Methane Adsorption-Desorption Hysteresis and Its Effect on Shale Gas Production

Jamiu Mufutau Ekundayo
0000-0001-5307-7974

This thesis is presented for the Degree of
Doctor of Philosophy
of
Curtin University

December 2020

Declarations

To the best of my knowledge and belief, this thesis contains no material previously published by any other person, except where due acknowledgment has been made.

This thesis contains no material which has been accepted for the award of any other degree or diploma in any university.

Signature: Ekundayo, J. M.

Date: 21 December 2020

Abstract

Gas desorption is one of the major gas transport mechanisms in shale gas reservoirs. However, its actual contribution to gas production is often masked by the indiscriminate use of adsorption-derived parameters for desorbed gas volumes during gas production calculations at reservoir conditions. Traditionally, it is believed that gas adsorption is fully reversible at the high-pressure, high-temperature conditions found in shale gas reservoirs. However, research has shown that desorption isotherms are often different from, and often show hysteresis with their adsorption counterparts. But, the cause of this hysteresis behavior at high temperature and high pressure remains unclear. More importantly, the implications of sorption hysteresis on production performances of shale gas reservoirs have not been previously studied.

In this study, adsorption and desorption isotherms of methane were studied at temperatures of 25°C, 40°C, 60°C, and 80°C and pressures up to 7MPa using the Particulate System's HPVA-II® 200 equipment first for a coal sample and then for shale samples from Ordovician Goldwyer Formation, Canning Basin, Western Australia. The coal sample was used to test the effect of equations of states (EOSs) on the measured isotherms and their subsequent applications. The use of coal eliminated the complexities of shale and isolated the effect of fluid densities resulting from the use of different EOSs. Six popular EOSs namely Peng-Robinson's (PR), Soave-Redlich-Wonk's (SRK) and their volume translated forms (PR-Peneloux and SRK-Peneloux), Soave's modified Benedict-Webb-Rubin's (SBWR), and Lee-Kesler's (LK) were used for data interpretation and the results were compared with those calculated by the equipment using Z-factors from the equipment's software implementation of McCarty and Arp's EOS for helium and Setzmann & Wagner's EOS for methane (a combination subsequently referred to as NIST-refprop®). The three-parameter Langmuir model was used to describe each of the adsorption isotherms and the results showed that all the equations of state tested gave varied deviations in the measured isotherms, calculated model parameters, observed type and degree of sorption hysteresis and original gas in-place because of the variations in the calculated Z-factors of both helium and methane relative to NIST-refprop. Consequently, the SWBR EOS was selected for studies involving the shale samples.

Early pore saturation, indicated by maximum excess adsorptions at pressures in the neighbourhood of the critical pressure of methane, was also observed for all the shale samples. Consequently, the measured sorption isotherms could not be represented directly by three-parameter Langmuir model. Therefore, a two-step modelling approach was adopted. First, each

excess adsorption isotherm was modelled using Dubinin–Radushkevich (D-R) model to obtain the adsorbed phase density used to convert both the adsorption and desorption amounts to their absolute equivalents. In the second step, and based on the intended application of the results, the conventional Langmuir model was used to describe the resultant absolute adsorption and desorption isotherms. Significant hysteresis was observed for all samples at all temperatures, albeit the relationship between the size of the hysteresis and temperature was inconsistent. Desorption isotherms resulted in lower model parameters than the corresponding adsorption isotherms. For both processes, Langmuir volumes positively correlated with TOC contents but show no significant correlations with total clay contents. A novel ratio of total clay to TOC (i.e. clay-to-organic-carbon, COC) applied as a single predictor showed good correlations with Langmuir volumes (R^2-values comparable to those of correlations with TOC). The size of the hysteresis, as well as the BET surface areas and pore volumes determined from low-pressure adsorption experiments, also showed significant correlations with TOC contents and COC.

Lastly, a compositional 3D multiple interacting nested continua (MINC) model was developed in CMG-GEM® to test the effect of the observed hysteresis at reservoir conditions on shale gas production. For each sample, a base scenario, corresponding to a "no-sorption" case was compared against two other cases; one with adsorption Langmuir parameters (adsorption case) and the other with desorption Langmuir parameters (desorption case). The simulation results showed that while gas production can be significantly under-predicted if gas sorption is not considered, the use of adsorption isotherms in lieu of desorption can lead to over-prediction of gas production performances.

Parts of this thesis have been published in the following journals and conference articles:

Publications

Ekundayo, J. M., Rezaee, R. & Fan, C. 2020. Experimental investigation and mathematical modelling of shale gas adsorption and desorption hysteresis. Journal of Natural Gas Science and Engineering, 103761.

Ekundayo, J. M., and R. Rezaee. 2019. "Numerical Simulation of Gas Production from Gas Shale Reservoirs – Influence of Gas Sorption Hysteresis." *Energies 12 (18)*

Ekundayo, J. M., and R. Rezaee. 2019. "Volumetric measurements of methane-coal adsorption and desorption isotherms—Effects of equations of state and implication for initial gas reserves." *Energies 12 (10)*

Ekundayo, J. M., and R. Rezaee. 2019. "Effect of Equation of States on High-Pressure Volumetric Measurements of Methane-Coal Sorption Isotherms-Part 1: Volumes of Free Space and Methane Adsorption Isotherms." *Energy and Fuels 33 (2)*: 1029-1036

Conference Papers

Ekundayo, J. M., Rezaee, R. and Fan, C. (2020)" Effects of Gas Sorption Hysteresis on Gas Production from Organic-Rich Gas Shale Reservoirs" SPE-202462-MS accepted for presentation at the SPE Asia Pacific Oil & Gas Conference and Exhibition to be held 20 -22 October 2020 in Perth, Australia

Table of Contents

Acknowledgment

First, I would like to give all thanks to Allaah for seeing me through every stage of my life till now. Nothing, I have ever achieved, would have been possible without His permission.

My sincere appreciations go to my PhD supervisor, Professor Reza Rezaee for the technical and moral supports I received from him throughout this PhD journey. His timely responses to my eleventh-hour requests, his open-door approach to supervision, his constructive feedbacks and invaluable suggestions have all been instrumental to the successful completion of this thesis.

I would also like to thank my co-supervisors, Dr. Sam Xie and Associate Professor Ali Saeedi and Dr. Chunyan Fan for their guidance and moral supports throughout the 3+ years of my PhD journey. The regular meetings with Dr. Chunyan Fan were helpful in my navigating through the most daunting stages of my HPVA experimental data analysis.

My studentship in this program has blessed me with the friendship and love of lots of people in no specific order: Dr. Lukman M. Johnson, Tolu Olu-Ojo, Mohammed Al-Mobarak, Dr. Naseer Al-Hinnai, Naseer Al-Maskari, Moatiz Mansi, Faaiz Al-Shajalee, Dr. Ahmad Sari, Mohammed Daway, Omar Al-Fatwali, Shoaib Memon, Zain-Ul-Adedin Arain, Muhammad Atif Iqbal, Miftah Hidayat, Cut-Aja Fauziah, Dr. Nadia Testamanti, Dr. Jie Zou, Yujie Yuan, Xiu Liu, Lingping Zeng, Gonzalo Ceron Lopez, Dr. Eghan Arjomand, Duraid Al-Bayati, Emad Al-khdheeawi, Moustafa Elzeftawy, Dr. Pooya Hadian, Partha Mandal, Ifechukwu Michaels, Jimmy Li, Faranak Parvinpour, Runhua Feng, Zhiqi Zhong, Nichole Sik, Ruby Lo, Nathan Tarom, Bob Webb. You all made my PhD experience rewarding and worthwhile. Many thanks to Dr. Jie Zou for guiding me through how to use the HPVA equipment for my adsorption and desorption experiments. Special thanks to Dr. Christopher Lagat and Associate Prof. Mofazzal

List of Figures

List of Tables

Chapter 1

Introduction

1.1 Background

Despite the increased interest in renewable sources of energy, natural gas resources continue to play a vital and leading role in global energy supply, accounting for over 24% of the primary energy supply in 2019 (BP, 2020). According to BP's 2020 energy outlook, natural gas consumption rose by 2% in 2019 while gas production increased by 3.4% over the same period (BP, 2020). Moreover, the International Energy Outlook 2016 (IEO2016) also projected that the global demand for natural gas will increase by more than 69% in the next 2 decades, from 120 trillion cubic feet (Tcf) in 2012 (EIA, 2016). With 90% of the current gas production in the United States of America (USA) contributed by tight and shale gas resources (Figure 1.1), it is evident from the USA's Annual Energy Outlook 2020 (AEO2020) that unconventional resources (or more specifically gas shales) will contribute a significant portion of the gas production over the next few decades.
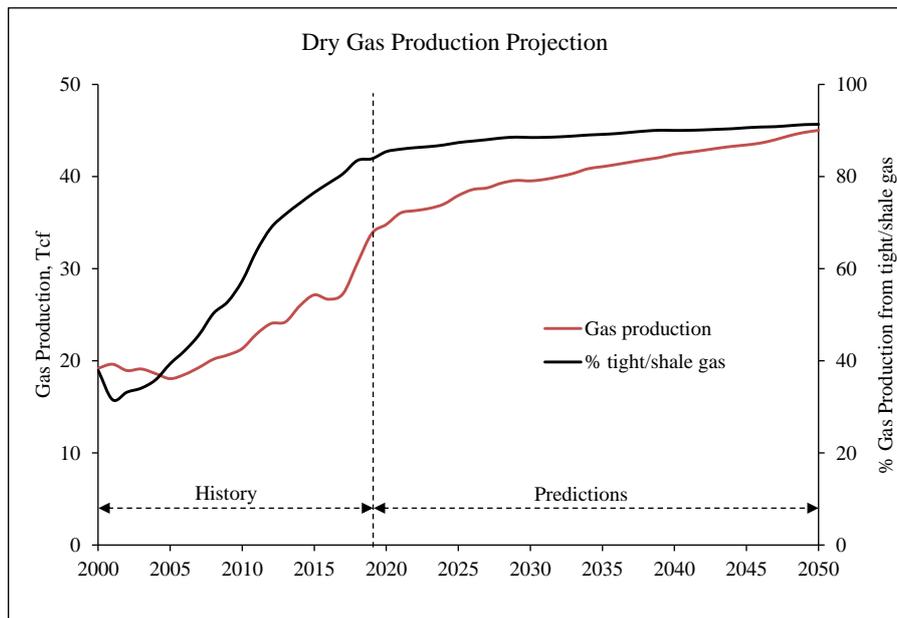
Figure 1.1: US gas production history and projections with contribution from shale gas (data from EIA (2016))

Shale gas resources are widely distributed across many countries with the USA at the forefront of the exploration and development of these low-quality reservoirs. Australia is also blessed with abundant shale gas resources, estimated at 437 Trillion cubic feet (Tcf) technically

recoverable volume, which could augment the country's liquefied natural gas (LNG) exports when fully harnessed (Cook et al., 2013). Most of the shale resources in Western Australia are concentrated in the Canning Basin in which the Ordovician Goldwyer Formation forms the most prospective (Bahar and Triche, 2013). Several studies have shown that the Goldwyer Formation is highly diverse in organic matter content, and mineralogy (Johnson et al., 2019, Ghori, 2013, Spaak et al., 2017, van Hattum et al., 2019, Yuan et al., 2019, Johnson et al., 2017, Johnson, 2019, Hashimoto et al., 2018, Ghori, 2018, Bahar and Triche, 2013, Alshakhs, 2017, Delle Piane et al., 2015). However, despite this knowledge, little is known of the relationship between the properties of the shale reservoirs and their gas contents. Thus, one of the purposes of this thesis is to establish such a relationship through a series of experimental studies and subsequently mathematical modelling of the experimental results.

1.2 Shales and their Characteristics

Shales are composed of complex pore structures made up of organic matter and inorganic nano-scale pores of different sizes broadly classified as micropores (pores up to 2nm), mesopores (pores in the range 2nm – 50nm) and macropores (pores > 50nm) (Thommes et al., 2015, Sing et al., 1985). Adsorbed gas in shale rocks reside mostly in the micropores and mesopores while the macropores, and natural fractures, mostly contain free-gas and in situ water saturation (Ross and Bustin, 2007, Ross and Bustin, 2008, Bustin, 2005, Chalmers and Bustin, 2007). Thus, a combination of different experimental techniques is required to fully describe the spectrum of pores and the structural properties of shale rocks (Guo et al., 2019, Chen et al., 2017, Bahadur et al., 2014). Low-pressure adsorption and desorption of Nitrogen (LPN$_2$) at 77K is the most popular technique among researchers because it can conveniently cover a wide range of pore sizes (up to about 300nm) (Klobes et al., 2006, Sing and Williams, 2004, Garrido et al., 1987, Hansen and O'Leary, 1993). Micropores not accessible to nitrogen and are best characterised using low-pressure carbon dioxide (LPCO$_2$) adsorption at 273K (Sing and Williams, 2004, Garrido et al., 1987, Ross and Bustin, 2009). Given its smaller molecular size, CO$_2$ can access ultra-low micropores and as such, LPCO$_2$ adsorption is commonly used for characterising ultra-micropores (down to about 0.35nm) (Thommes et al., 2012). The results of the LPN$_2$ tests, often modelled using the Brunauer, Emmett, and Teller (BET) isotherm (Brunauer et al., 1938), can be combined with density functional theory (DFT) kernels (Ravikovitch et al., 2001, Do and Do, 2003, Lastoskie et al., 1993), to obtain the distribution of pore sizes. Analytical models such as the Barrett-Joyner-Halenda (BJH) model can also be used to derive the mesopore volumes and specific surface areas (Anovitz and Cole, 2015, Clarkson et al., 2012, Clarkson et

al., 2013, Kuila et al., 2014, Cui et al., 2007). LPCO2 tests are often modelled using Dubinin-Radushkevich (DR) which can be combined with t-plots to obtain the micropore volumes and specific surface areas (Kuila et al., 2014, Ross and Bustin, 2009, Gregg et al., 1967).

Although LPN2 tests can give the distribution of macropores up to about 120nm, mercury intrusion is capable of characterising pores up to 1mm and as such, is the preferred approach for characterising macropores (Klock, 1968). Mercury intrusion technique relies on the application of an external pressure, P_c to deliver mercury into pore throats (Lowell and Shields, 1981) of average radius r. The Young-Laplace equation (Equation 1.1) gives the relationship between P_c, r, and the contact angle (θ) between the mercury and the solid (Washburn, 1921).

$$P_c = -\frac{2\gamma \cos \theta}{r} \qquad\qquad 1.1$$

The parameter γ in equation 1.1 is the surface tension between the non-wetting phase (mercury) and wetting phase (air). Given the inverse relationship depicted by equation 1.1 between P_c and r, pressures greater than *400MPa* may be required to penetrate small pore throats, down to about 3nm lower pore throat limit (Cao et al., 2016). This obviously shows the mercury-intrusion technique is not capable of defining the wide spectrum of pore throat sizes inherent in shale rocks. Besides, the high pressure required to force mercury into the smaller pore throats may result in induced fractures within the rock sample (Klaver et al., 2015). Thus, the characterizations of micropores and mesopores are routinely performed using the low-pressure gas adsorption techniques previously described.

The techniques discussed above are all invasive and as such, can only provide inFormation on the accessible pores (Bahadur et al., 2014). Non-invasive methods such as the nuclear magnetic resonance (NMR), small-angle and ultra-small-angle neutron scattering (SANS and USANS) have also be used by various researchers to characterize the pore structures of shale rocks (Bahadur et al., 2014, Testamanti, 2018, Clarkson et al., 2013, Yang et al., 2017, Sun et al., 2017, Zhang et al., 2015a, Mastalerz et al., 2012, Bernard et al., 2012). They can provide useful information on the distribution of pore size distributions and are also useful for inferring the structural properties of the pore systems in shale rocks. Information on pore morphology can be qualitatively inferred from the techniques so far discussed. Microscopic imaging techniques, such as the scanning electron microscopy (SEM) and its various adaptations (for example, field emission scanning electron microscopy (FE-SEM), focused ion beam scanning electron microscopy (FIB-SEM), and transmission electron microscopy (TEM)) are preferred in

obtaining information on the morphology of the pore system in shales (Milliken and Curtis, 2016, Loucks et al., 2009, Xiong et al., 2020, Bahadur et al., 2014). Besides, these techniques can provide visual information on the pore geometry, pore size, pore types, and pore connectivity (Chen et al., 2019b, Guo et al., 2019). However, they are best useful as qualitative indications of pore properties like pore sizes and their distributions (Chen et al., 2019b, Guo et al., 2019).

In terms of composition, shales are composed of organic matter and several inorganic constituents such as clay minerals, quartz, feldspar, pyrites, carbonates, plagioclase, and their cohorts. The abundance and maturity of the organic matter content of a shale Formation can be obtained from its geochemical properties often measured using RockEval pyrolysis. The clay and other mineral contents of shale are routinely determined using x-ray diffraction (XRD) analysis. In addition to controlling its gas adsorption capacity, the composition of a shale affects its mechanical (strength) and chemical stability (Li et al., 2019) and consequently, its brittleness and fracability (Ma et al., 2019). Thus, a detailed understanding of the mineralogy of shale is essential to both reserve estimations and development planning of the shale reserves. It not surprising therefore that the relationships between adsorption capacities (as well as gas production performances) of shale reservoirs and shale properties such as total organic carbon (TOC) contents and clay contents have been extensively studied (Zou and Rezaee, 2019, Gasparik et al., 2014a, Zou and Rezaee, 2020, Wang et al., 2017c, Liu et al., 2017a, Ma and Guo, 2019, Chen et al., 2019a).

1.3 Shale Gas Adsorption and Desorption

Significant portions of the gas in unconventional resources like shale are predominantly stored as adsorbed gas in the internal surface areas of the rock matrix (Curtis, 2002, Leahy-Dios et al., 2011) making adsorption the primary storage mechanism in unconventional reservoirs. The relation of the amount of adsorbed gas to pressure at a constant temperature is referred to as adsorption isotherm and has been the primary means of assessing the gas adsorption capacity of shale reservoirs (Seidle, 2011b). The reversed process of adsorption is desorption in which the adsorbed gas is released as pore pressure is reduced. The relation is mostly measured experimentally using different techniques such as volumetric, manometric, gravimetric, and some combinations of thereof (Keller and Staudt, 2005) most of which rely on some equation of state to obtain gas compressibility factors for data interpretation (Gasparik et al., 2014b).

As the pressure is lowered to produce gas, adsorbed gas molecules in the pores and surface of the adsorbent begin to desorb. Where the adsorption process is characterized by capillary condensation, the amount of desorbed gas at a given pressure is often different from the amount initially adsorbed at the same pressure. This phenomenon is known as sorption hysteresis and it is a common observation under low-temperature, low-pressure conditions (Rajniak and Yang, 1993). Adsorption and desorption of methane in coals and shales are usually conducted at high-temperature and high-pressure conditions, similar to reservoir conditions at which capillary condensation is theoretically impossible (Dantas et al., 2019). Thus, methane sorption hysteresis in coals and shales remains an elusive subject. Attempts have been made to attribute this anomaly to measurement uncertainties (Ozdemir, 2017, Bell and Rakop, 1986). However, this has been debunked by other researchers who have also offered several incongruous theories to explain this phenomenon.

In attempts to investigate high-pressure sorption hysteresis for methane on coal samples from Blue Creek and Cameo-D seams, Bell and Rakop (1986) reported significant hysteresis between measured adsorption and desorption isotherms. The authors were more focused on establishing the effects of simulated in-situ moisture contents on measured gas contents in comparison with actual field data and as such, the observed hysteresis was not linked to any physical parameter. Instead, the authors suggested that the sample preparation procedure, moisture contents, and temperature could significantly affect the results of sorption experiments (Bell and Rakop, 1986). In a similar study using pure CH_4, pure CO_2 and a natural gas, Pariti (1992) reported no hysteresis for any of the gases despite the visible differences between reported adsorption and desorption isotherms. Busch et al. (2003) reported different of degrees sorption hysteresis for both CO_2 and CH_4 on Argonne Premium coal samples of different ranks. The authors observed that the hysteresis decreased with coal rank for CO_2 but no relationship could be established for CH_4 hysteresis with coal rank (Busch et al., 2003). In their inter-laboratory comparison study for CO_2 sorption on similar coal samples, Goodman et al. (2004) also observed rank-dependent sorption hysteresis as reported by three of the participating laboratories (Goodman et al., 2004). The authors attributed the observed hysteresis to residual moisture contents, coal swelling and/or CO_2 trapping (Goodman et al., 2004). Ozdemir (2004) also explored adsorption and desorption isotherms of CO_2 on Argonne Premium coal samples of different ranks and found that significant hysteresis occurred at supercritical conditions for all ranks (Ozdemir, 2004). The authors also observed that the initial desorption steps appeared to be characterized by the readsorption of CO_2 (Ozdemir, 2004).

Weishauptová et al. (2004) reported low-pressure reversible sorption isotherms for methane on activated charcoal at 25 °C but significant hysteresis for methane on coal samples at the same experimental conditions (Weishauptová et al., 2004). The authors believed the observed hysteresis in coal was caused by methane absorption accompanying the adsorption process due to the increased contact time with methane (Weishauptová et al., 2004). Harpalani et al. (2006) also reported significant sorption hysteresis for CO_2 on coal samples from San Juan and Illinois basins but small to negligible hysteresis with methane. Harpalani et al. (2006) also reported significant CH_4 sorption hysteresis with coal samples from Illinois basins and zero CH_4 sorption hysteresis with a coal sample from San Juan under the same experimental conditions. However, CO_2 was reported to show significant sorption hysteresis for all samples (Harpalani et al., 2006). While the authors noted that the observed hysteresis could have been caused by many different reasons, they recommended further investigations of any claims of structural changes to the solid, caused by the sorption processes (Harpalani et al., 2006). Jessen et al. (2008) reported significant sorption hysteresis for CO_2, CH_4 and N_2 with coal samples from Powder River Basin. The authors claimed that surface heterogeneity, and not experimental errors, was the cause of the observed hysteresis (Jessen et al., 2008). Ju et al. (2009) reported CH_4 sorption hysteresis for both primary and tectonically deformed coal samples. The authors observed that the observed hysteresis is largest for the strongly deformed coal samples and smallest for the primary coals. The trend with deformation was attributed to structural changes to the micropores in the coal samples (Ju et al., 2009). Bae et al. (2009) reported that high-pressure sorption hysteresis could be related to reduced surface areas resulting from pore mouth blockage by volatile hydrocarbons. The authors believed that heat-treatment at high temperature, above a certain threshold potential known as the activation barrier (Bae et al., 2009), will result in the evolution of the volatile hydrocarbons and consequent opening of the pore mouths leading to increased surface areas and reduced hysteresis (Bae et al., 2009). Pan et al. (2010) also reported small hysteresis for both CO_2 and CH_4 on a coal sample from the Sydney Basin at different moisture contents. Battistutta et al. (2010) reported significant CO_2 sorption hysteresis and no hysteresis for N_2 & CH_4 on coal samples from South Wales Coalfield. The authors assumed insufficient equilibration time, presence of residual water content in the coal samples, and irreversible bonding between the molecules of CO_2 and coal were responsible for the observed hysteresis (Battistutta et al., 2010). The authors however failed to explain why these factors did not affect the sorption of N_2 and CH_4 on the same coal samples. Dutta et al. (2011) reported significant CO_2 sorption hysteresis on a set of coals from India and zero to discernible hysteresis for CH_4 on the same samples. The authors believed

molecular interaction of CO_2 with coal, CO_2 absorption by coal and CO_2 dissolution were the causes of the observed CO_2 sorption hysteresis (Dutta et al., 2011). The authors also assumed that the few cases of discernible CH_4 sorption hysteresis could be attributed to incomplete drying of the coal samples leading to measurement errors (Dutta et al., 2011). However, it was no clear why these errors did not exist in case of CO_2 considering that the same samples were used for both gases. Pillalamarry et al. (2011) reported no hysteresis for CH_4 on two coal samples even though their results for sample 1 showed that desorption isotherm fell below the adsorption curve from pressures above 4 MPa. Zhou et al. (2013) reported no significant sorption hysteresis for pure N_2, CO_2 and CH_4 on a coal sample from Qinshui Basin but significant hysteresis for binary/ternary mixtures of the gases. Wang et al. (2014a) also reported CO_2 sorption hysteresis on coal. The authors found that the path followed by the desorption isotherm varied with the maximum pressure in adsorption cycle (Wang et al., 2014a). A similar observation was previously made by Jessen et al. (2008) for N_2, CO_2 and CH_4 on coal although the authors could not explain this observation. This observation of desorption path dependence on maximum adsorption pressure further reaffirms the failure of assuming reversible sorption isotherms for coals and shales under high-pressure, high-temperature conditions. Not only is it imperative to apply desorption isotherms for gas production calculations involving coal seams and shale reservoirs, but desorption scanning curves (resulting from the dependence on maximum adsorption pressure) may also be required to adequately match gas production history and ensure accurate forecasts. Zhang et al. (2014) and Feng et al. (2016) found a relationship between coal's particle sizes and sorption hysteresis for both CO_2 and CH_4, the hysteresis being larger for large particle sizes. To model their observed CO_2 and CH_4 sorption hysteresis four different coal samples, Zhang and Liu (2016) introduced a partitioning parameter to theoretically isolate adsorption sites unavailable to desorption. The authors believed the selectiveness of adsorption sites (related to Langmuir pressure) during desorption and/or gas-solid molecular interaction at the solid surface were the cause of observed hysteresis (Zhang and Liu, 2016). Liu et al. (2017b) believed sorption hysteresis is the consequence of irreversible gas absorption due to coal swelling during adsorption.

It is generally believed that, where hysteresis exists, desorption isotherms should lie above their adsorption counterparts. This type of hysteresis is referred to as "positive hysteresis" (Kim et al., 2011) and was the case with all the examples cited above. Less commonly, cases of "negative hysteresis" and cross-overs (desorption isotherm intercepting adsorption isotherm) have also be reported (He et al., 2010, Keller and Staudt, 2005, Kim et al., 2011, Rodrigues et

al., 2018). However, it was hitherto believed that such observations could only be caused by pressure non-equilibration, desorption of pre-adsorbed gas in the adsorbent (Keller and Staudt, 2005), or irreversible structural changes to the solid as a result of gas adsorption (He et al., 2010, Kim et al., 2011).

From the above literature survey, it is obvious that there is no consensus on what causes sorption hysteresis at high-pressure. Hence, the need for further research on the subject.

1.4 Research Objectives

Methane-shale adsorption isotherm has been widely studied both experimentally and mathematically for years due to the importance of the sorption mechanisms in shale gas reserves estimation and development. The sensitivity of measured isotherms to the gas compressibility factors used during experimental data interpretation has been reported (Gensterblum et al., 2010, Gasparik et al., 2014b, Goodman et al., 2004). However, it was not clear how much effect this would have on the model parameters associated with the isotherms as well as the reserves estimated from those parameters.

Besides, while there are numerous adsorption studies of methane on shale, none of those studies paid adequate attention to gas desorption despite the well-established need to incorporate this (desorption) in the flow equations for shale gas production. The need to perform desorption experiments is often ignored because the Langmuir isotherm, which is often assumed to be suitable for shale-gas adsorption, is believed to be fully reversible based on its underlying monolayer theory. Hence, adsorption curves are traditionally used to account for desorbed gas volume in shale-gas production equations. Also, while few reported cases of modelling high-pressure methane desorption in shales and coals with the Langmuir isotherm (modified or not) have been reported (Zhang and Liu, 2016, Bell and Rakop, 1986, Wei et al., 2017a), there is no record of an empirical model to estimate the Langmuir (or any similar model) parameters for desorption.

Based on the above-mentioned knowledge gaps, this research seeks to:

1. Investigate the effect of equation of state on measured isotherms, their derived model parameters, associated reserves estimate as well as the size and type of sorption hysteresis. To achieve this objective, seven different equations of state were applied to calculate the gas compressibility factors of helium and methane required to compute isotherms from measured HPVA data.

2. Investigate hysteresis between the adsorption and desorption isotherms of supercritical methane on shales and relate the observed hysteresis to temperature and shale properties. To achieve this objective, series of adsorption and desorption isotherms were measured for a number of shale samples at four different temperatures and up to 7MPa. The samples exhibited early pore saturation, resulting in early peaks in excess adsorption (at about 5MPa). Thus, the measured isotherms were converted to absolute ad/desorption isotherms using adsorbed phase densities calculated from Dubinin-Radushkevich (DR) model and then fitted to the Langmuir model.

3. Develop analytical models for predicting Langmuir parameters, for both adsorption and desorption as functions of temperature and shale properties.

4. Investigate the effect of sorption hysteresis on gas production from gas shale reservoirs. This was achieved through numerical simulation studies utilizing a single-phase, compositional, MINC model developed with Computer Modelling Group's GEM$^{\circledR}$ (ref).

1.5 Thesis Layout

Chapter 1 provides a quick insight into the need for shale gas exploration and production. It presents an overview of the characteristics of shale reservoirs that make them unconventional gas reservoirs. It introduces gas adsorption as a key process in shale gas reserves estimation and gas desorption has a key shale gas transport mechanism. This chapter also covers a review of the existing literatures on the causes of sorption hysteresis supercritical methane on coals (and shales) at high-pressure conditions. Lastly, the chapter presents the primary objectives of this research and x-rays the contents of each chapter contained in this thesis.

Chapter 2 describes the characteristics and geological background of the samples used in this study. Details of the experimental approaches used in characterising the samples and the relationships (or otherwise) between the mineralogy, geochemical and micro-structural properties of the Ordovician Goldwyer shales are discussed. Some parts of this chapter have been recently published (along with Chapter 4) in the Journal of Natural Gas Science and Engineering.

Chapter 3 describes the high-pressure volumetric analysis (HPVA) approach for measuring the adsorption and desorption isotherms of supercritical methane on coal. Its primary focus is to present the effect of equation of state on measured isotherms and their associated model parameters, the size and type of hysteresis between the resulting adsorption and desorption

isotherms (if any), as well as estimated gas reserves. The use of a coal sample was to eliminate complications that might be introduced by the complex microstructures of shale rocks and isolate the effects of fluid density on the final isotherms. This chapter is a combination of two already published articles.

Chapter 4 presents the results of HPVA measurements of methane sorption isotherms on shale samples. Mathematical modelling of the isotherms is also presented in this chapter. It also presented the approaches to quantify the size of the hysteresis between the measured adsorption and desorption isotherms. Lastly, analytical models of the relationships between the model parameters, temperature, and key shale properties are also presented. This chapter has also been recently published in the Journal of Natural Gas Science and Engineering.

Chapter 5 presents an investigation of the effect of observed sorption hysteresis on shale gas production. A composition three-dimensional single-well model, developed with CMG-GEM$^{\circledR}$ was used for this purpose. This chapter is expanded from a section of an article that was published in Energies.

The last chapter, **Chapter 6,** is a summary of the key findings and conclusions from this thesis. It also provides recommendations for further research on the subject.

Chapter 2

Sample Selection and Characterisation

2.1 Introduction

Until recently, interests in unconventional resources, such as shale gas resources, have soared primarily due to technological advances in hydraulic fracturing and multi-lateral drilling which have facilitated production from unconventional resources (Yu et al., 2014a, Feast et al., 2015). Shale is a complex micro-structure that requires the integration of different experimental methods for its full characterisation. Geochemical properties determined from thermal treatment and kerogen pyrolysis are used to infer the hydrocarbon generation potential and thermal maturity of the rock (Hunt 1996, Lafarge et al., 1998, Li et al., 2018, Peters and Cassa, 1994, Peters, 1986, Rabbani and Kamali, 2005). The mineral contents are often determined with x-ray diffraction (XRD) tests and analysis and can be used to infer the brittleness and fracability of the Formation (Ma et al., 2019). Pore structural properties such as pore-size distributions, surface areas, and pore volumes and their distributions can be determined from low-pressure adsorption nitrogen experiments at 77K (Sing, 2001, Sing et al., 1985, Thommes et al., 2015). Low pressure adsorption of carbon dioxide (CO_2) gas at 298K can be conducted, if necessary, to further characterise micropores inaccessible to nitrogen. A careful combination of these properties can provide useful insights into their distribution across the depth of the Formation, generating continuous profiles that can be correlated with wireline logs.

While the geochemical properties of the Goldwyer Formation in the Canning Basin are well documented, little has been reported about the relationship of these properties and the mineral composition as well as the pore characteristics of this Formation. Most published articles on this subject often concluded that total organic carbon (TOC) content is the controlling parameter for the pore structural properties of this shale Formation (Testamanti, 2018). Such conclusions are premised on the poor to weak correlations observed between total clay contents and pore structural properties (Testamanti, 2018, Labani, 2014). However, Yuan et al. (2019) recently reported that clay contents are the principal factors affecting the properties of mesopores of size range 2 -17 nm in Goldwyer Formation (Yuan et al., 2019). Since this size range accounts for a significant proportion of the pores in this Formation, relying on TOC contents alone for predicting the rock properties in this Formation may be grossly misleading.

This study presents a new perspective to the relationships between the geochemical properties, mineralogy, and pore structural properties of Goldwyer Formation using experimental data from eight samples selected across the three sub-divisions of the Formation. Acknowledging the lack of any appreciable mathematical relationship between the TOC contents and clay minerals, we employed a novel clay-to-organic carbon ratio (COC) as a single parameter to correlate with the micro-structural properties determined from low-pressure nitrogen adsorption/desorption experiments.

2.2 Geological Overview – Sample Description

Predominantly in Western Australia, the Canning Basin spans approximately 506,000 km^2 in total area (Hashimoto et al., 2018). Structurally compartmentalized by the NW-SE trending, Fitzroy Trough- onshore Gregory Sub-basin and the south-bound Willara Sub-basin–Kidson Sub-basin, depocenters, the onshore Canning basin accounts for about 85% of the total area. These depocenters have maximum sediment thicknesses of 15km and 5km (Hashimoto et al., 2018, Kennard et al., 1994, Parra-Garcia et al., 2014), and are separated by the Jurgurra, Mowla and Barbwire terraces, Broome platform, and the Crossland platform. While the Jones arch separates the Fitzroy trough and the Gregory sub-basin, the Munro arch separates the Willara sub-basin and the Kidson sub-basin as depicted by Figure 2.1. More elaborate discussions on the geology of the Canning basin are available in (Hashimoto et al., 2018, Ferguson, 2016, Kennard et al., 1994, Parra-Garcia et al., 2014) and the references therein. However, a brief discussion on the Broome platform is subsequently presented to provide some insights into the geological basis of the Goldwyer Formation from which the samples used in this study were acquired.
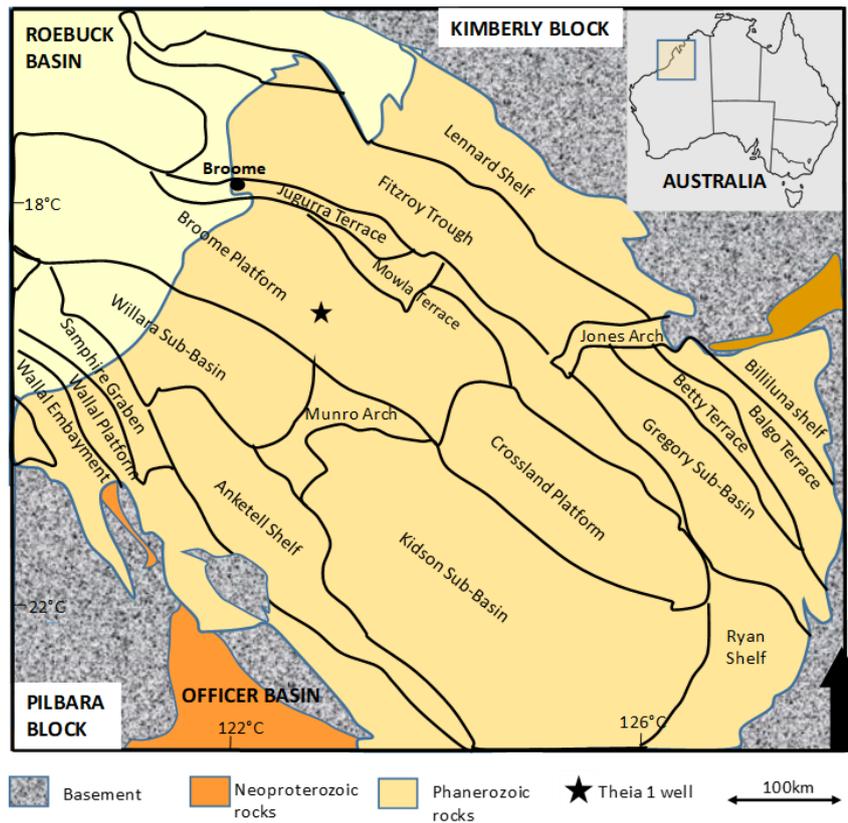
Figure 2.1: Map of Canning Basin Showing Broome Platform with Theia 1 well (modified from Johnson et al. (2019))

The Goldwyer Formation occurred within the Ordovician-Silurian sequence and is predominantly made up of oil and gas-prone kerogen types II & III (Bahar and Triche, 2013). The Formation is primarily composed of alternating proportions of calcareous mudstone and dolomitized limestone with sparse distributions of pyrite mostly in the south-east area of the basin (Alshakhs, 2017). Structurally, the Goldwyer Formation is sub-divided into upper (Goldwyer – I), middle (Goldwyer – II) and lower (Goldwyer – III) with evidence showing vertical and areal variations in geochemical properties and source rock potential across the Formation (Johnson, 2019). Along the eastern part of the Formation, the upper Goldwyer is reported to have excellent geochemical properties (Bahar and Triche, 2013, Cadman et al., 1993) and consequently, excellent hydrocarbon generating potential due to the abundance of *Gleocapsamorpha Prisca* (Spaak et al., 2017). Theia-1 well (Figure 2.2) recently drilled on the Broome Platform has cleared our initial understanding of the source rock potential of the lower Goldwyer Formation in this platform. Samples taken from the Theia 1 well showed evidences of good source rock potential in the lower Goldwyer Formation contrary to the previously held views that the Formation is poorly developed in the north of the Broome Platform and towards the Willara sub-basin (Hashimoto et al., 2018, Kennard et al., 1994, Spaak et al., 2017).

For this study, eight shale samples were selected from the Theia 1 well to cover the different sub-divisions (units) of the Goldwyer Formation as shown in Figure 2.2. Core descriptions revealed that the shallowest sample, GTh-1 is predominantly claystone with traces of limestone while the rest of the samples contains varying proportions of (calcareous) mudstone and (fossiliferous) limestone. The middle Goldwyer appears to be richer in limestone than the rest of the Formation and the proportion of mudstones was found to be higher in the lower part of the Formation.
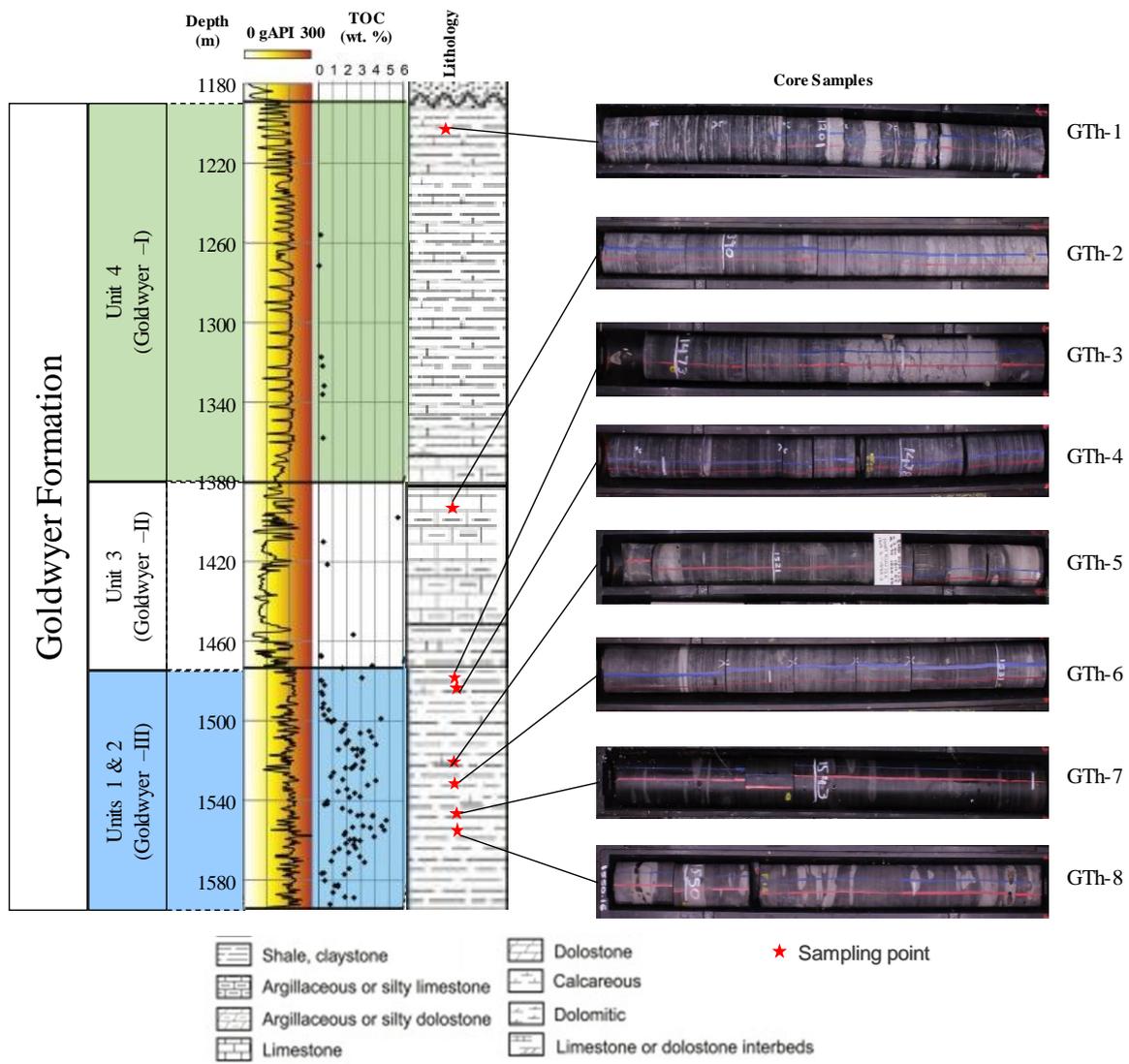
Figure 2.2: Gamma-ray, TOC content and lithological distributions in Theia 1 well drilled into Broome Platform with core images of our study samples (modified from Spaak et al. (2017))

2.3 Sample Characterization

Following the core descriptions, geochemical, mineralogical, and pore size characterisations of the samples were conducted respectively using RockEval-6®, X-ray diffraction, and low-pressure nitrogen sorption experiments. The details of each experiment are discussed subsequently.

2.3.1 Geochemical Analysis

Aliquots of the pulverised samples were placed into the sample crucibles sample holders and subjected to pyrolysis using the RockEval-6® (Vinci Technologies, France) available at the Unconventional Gas Resources (UGR) research laboratory, Curtin University. The key steps used in the RockEval-6® pyrolysis are summarized as shown in Figure 2.3 below:

1. Sample preparation and loading
- Place 60 - 80 mg of pulverised sample into the crucible

2. Calibration with IFP standard sample - 16000
- Initial analysis and subsequently after every six samples

3. Isothermal Heating to 300°C
- To expel free hydrocarbons from the sample - S_1 peak

4. Thermal Cracking of Kerogen from 300 - 650°C at 25°C/min
- To release additional hydrocarbons - S_2 peak at a temperature, T_{max}
- To release carbondioxide, CO_2 at about 390°C- S_3 peak

Figure 2.3: Steps in RockEval-6® pyrolysis of rock samples

2.3.2 Mineralogy

The mineral contents of the samples were determined using the Bruker D8 X-ray diffraction (XRD) unit available at Curtin University's John de Laeter Centre. Homogenised aliquots of the pulverised samples were treated with methanol and then placed in an oven to dry under a vacuum at a temperature of 40°C for an extended period prior to the XRD analysis. Rietveld refinement method implementation in TOPAS software was used to analysis the resulting XRD patterns (Hadian and Rezaee, 2020).

2.3.3 Low-Pressure Nitrogen Adsorption and Desorption Tests

Following the geochemical and mineralogical characterisations, five of the samples were subjected to low-pressure nitrogen adsorption and desorption experiments to quantify their

pore-size distributions and related pore-structure characterisation. The choice of these five samples was dictated by sample availability. The nitrogen isotherms were measured at 77.3K and relative pressure (P/P$_o$) range from about 0.01 to 1 for all five shale samples using Micromeritics® Tristar II 3020 apparatus. Prior to the tests, each sample was pulverized and sieved to particle sizes 44−74 μm (325-200 mesh). This range was selected to cover a wide range of pore sizes typically found in shales and more so, to provide adequate surface areas favourable to gas adsorption (Zou and Rezaee, 2016a, Yan-Yan et al., 2016). An aliquot of each pulverized sample was then degassed at a temperature of 110°C for at least eight hours followed by the adsorption and desorption measurements. The isotherms and their associated parameters (such as pore-size distributions, surface areas and pore volumes) were automatically generated by the equipment's inbuilt software system using the Brunauer-Emmett-Teller (BET) model (Brunauer et al., 1938) for isotherm fitting and density functional theory (DFT) (Ustinov and Do, 2004, Ustinov and Do, 2005, Lastoskie et al., 1997, Lastoskie et al., 1993) for pore size distribution (PSD).

2.4 Results and Discussion

2.4.1   Geochemical Properties

Table 2.1 shows the results of the RockEval® pyrolysis. The samples have TOC contents in the range of 0.28 – 4.16 wt. % covering a wide spectrum of source rock qualities from poor to excellent based on the classification by Peters and Cassa (1994). The first peak, S_1, detected by the flame ionizing detector (FID) in the equipment (Lafarge et al., 1998, Peters, 1986) is in the range of 0.04 – 2.85 mg/g. This parameter represents the amount of hydrocarbon expelled at 300°C prior to thermal cracking (Peters, 1986, Lafarge et al., 1998). The second peak, S_2 has values in the range 0.85 – 7.55 mg/g, suggesting that the source rocks range from poor to good based on the same classification scheme by Peters and Cassa (1994). These values denote the amounts of hydrocarbon produced from the thermal cracking of the kerogen and heavy hydrocarbons present in the rock samples. Similarly, the third peak, S_3, representing the amount of carbon dioxide produced through thermal cracking of kerogen at about 390°C, is in the range 0.28 – 0.73 mg/g. T_{max}, the temperature at which S_2 was recorded ranged from 430 – 458°C indicating a varied level of thermal maturity. Hydrogen index (HI) ranges from 107mg/g TOC to 393mg/g TOC indicating kerogen types II, II/III and III. The observation of kerogen type II is supported by the evidence of graptolite (Figure 2.4) in the upper Goldwyer Formation (Spaak et al., 2017). The observation of kerogen types II/III and III could be attributed to organic matter maturation since land plants did not exist in the Ordovician-Silurian age (Wellman et

al., 2013). Using pyrolysis-gas chromatography data from samples taken across the Goldwyer Formation, Johnson et al. (2020) has also recently attributed their observation of kerogen type II/III in the lower Goldwyer Formation to maturity effect. Oxygen index (OI) is significantly higher for the shallowest sample compared to the remaining samples with values ranging 13mg/g TOC in the deepest sample to 175mg/g TOC in the shallowest sample. Lastly, the production index (PI) ranges from 0.035 to 0.375 indicating varied stages of thermal maturity. Although sample GTh-1 has a high HI value, this does not necessarily imply high potential to generate hydrocarbon (Peters and Cassa, 1994, Peters, 1986) but may be attributed to its low TOC content. Similarly, the high OI value for this sample may be related to oxidation (Nunez-Betelu and Baceta, 1994), but is more likely invalid because organic lean samples (TOC < 0.5 wt.%) generally produce anomalous values (Espitalie et al., 1977).

Table 2.1: Geochemical properties of study samples

Sample ID	Depth m	TOC wt%	S_1 mg/g	S_2 mg/g	S_3 mg/g	T_{max}, °C	HI mg/gTOC	OI mg/gTOC	PI -
GTh-1	1201	0.28	0.04	1.10	0.49	442	393	175	0.035
GTh-2	1390	1.26	0.63	2.43	0.28	454	193	22	0.206
GTh-3	1473	3.20	2.12	7.55	0.51	454	236	16	0.219
GTh-4	1478	2.82	1.57	4.66	0.43	456	165	15	0.252
GTh-5	1521	2.76	1.63	3.50	0.63	430	127	23	0.318
GTh-6	1531	0.75	0.51	0.85	0.41	458	113	55	0.375
GTh-7	1543	3.86	1.86	4.12	0.73	435	107	19	0.311
GTh-8	1550	4.16	2.85	6.96	0.53	430	167	13	0.291
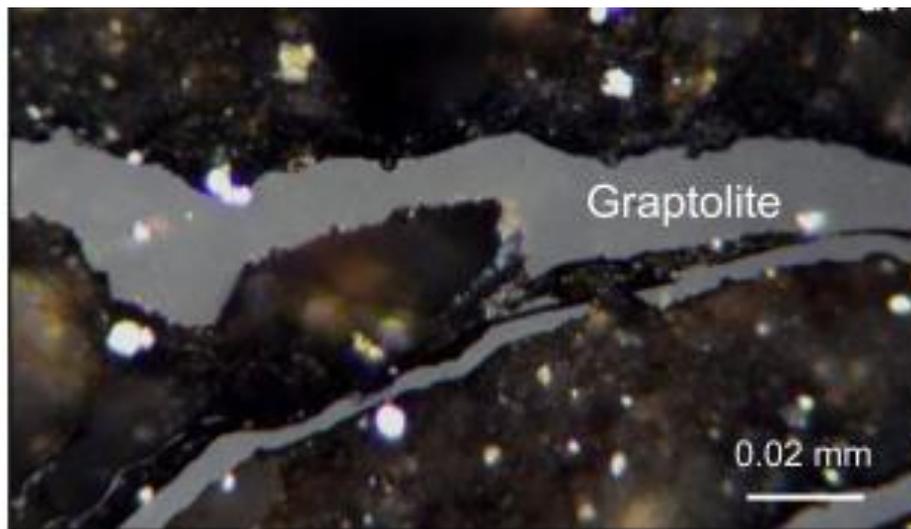
Figure 2.4: A photomicrograph showing evidence of graptolite in Goldwyer I (adopted from (Spaak et al., 2017))

2.4.2 Mineral Compositions

The XRD analysis of the samples revealed a vertical complex variation in the mineralogy of the samples. As shown in Table 2.2, six of the samples are composed primarily of clay minerals (ranging from 67.5% - 83.5%), of which illite/mica form most of the clay contents, indicating a high degree of plasticity which may not be favourable for hydraulic fracking. The remaining two samples, GTh-5 and GTh-8 have lower clay contents, are slightly richer in quartz and more in carbonates, and are therefore less plastic and more suitable for hydraulic fracking than the other samples. Combined with the quartz contents, the presence of potash-feldspar (K-feldspar) in all the samples indicates some, albeit varied, degree of brittleness (Ma et al., 2019).

Table 2.2. Mineralogical Composition of study samples.

Sample ID	Depth, m	Quartz, %	K-feldspar, %	Plagioclase, %	Total Clay*, %	Carbonate**, %	Pyrite, %
GTh-1	1201	15.68	2.23	1.96	76.58	2.11	1.44
GTh-2	1390	12.42	1.24	1.84	83.50	0.25	0.77
GTh-3	1473	17.39	1.78	3.54	74.28	0.42	2.59
GTh-4	1478	20.11	2.63	4.21	67.52	3.93	1.60
GTh-5	1521	27.11	1.49	3.02	37.10	29.11	2.17
GTh-6	1531	12.93	1.91	1.20	68.44	12.71	1.75
GTh-7	1543	9.14	2.74	2.06	72.47	12.11	2.42
GTh-8	1550	21.61	11.13	4.32	46.33	14.21	1.47

* Total clay = Kaolinite + illite/mica + chlorite; Carbonate** = calcite + dolomite

2.4.3 Low-Pressure Nitrogen Sorption Isotherms and Pore Structural Properties

The results of the low-pressure nitrogen adsorption and desorption tests are shown in Figure 2.5. As shown in the Figure, all the samples have non-zero initial nitrogen adsorption uptakes which may be an indication of micropore filling or some localised monolayer coverage (Sing, 2001). The samples (especially GTh-3 & GTh-4) exhibit significant overlap between the onset of the multilayer adsorption and the completion of monolayer coverage, which appears to be at relative pressure less than 0.1 (as can be seen in GTh-1, GTh-2 and GTh-6). The multilayer coverages appear to be associated with mesopore filling and capillary condensation indicated by the sharp increase in the nitrogen adsorption up to about 0.9 relative pressure. The further increase in the nitrogen adsorption for relative pressure > 0.9 is an indication of macropore filling (Xiong et al., 2015). The desorption isotherms for all the samples exhibit significant hysteresis with the adsorption counterparts due to the mesopores emptying along paths different from those followed during mesopore filling (Sing, 2001). The shapes of the hysteresis loops suggest they are all of type H3 (based on IUPAC classification) characterised

by adsorption isotherms of type II and lower closure of the hysteresis loop, at relative pressure of about 0.4 – 0.5, suggesting slit-like nanopores (Thommes et al., 2015, Sing et al., 1985).
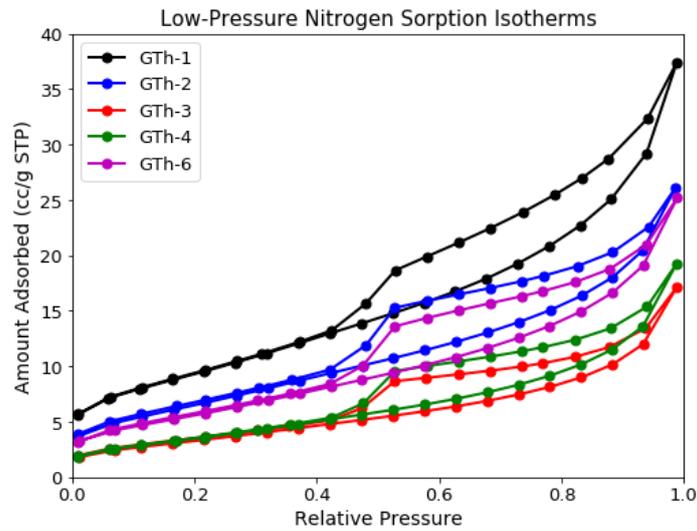
Figure 2.5: Low-pressure nitrogen adsorption and desorption isotherms showing hysteresis

As shown in Figure 2.6, the samples have similar ranges of pores which are roughly bi-modally distributed with dominant pore sizes of approximately 4nm and 25nm. Besides, the Figure shows small peaks in the PSDs below the 2nm micropore boundary and the presence of macropores (> 50nm). This implies that mesopores (2nm - 50nm) account for the majority of the pores in all the samples. The small volume of micropores observed here may be due to the limited accessibility of these small pores by nitrogen molecules as a result of pore blockage caused by illite precipitation (Pevear, 1999, Delle Piane et al., 2015) and other diagenetic reactions (Delle Piane et al., 2015).
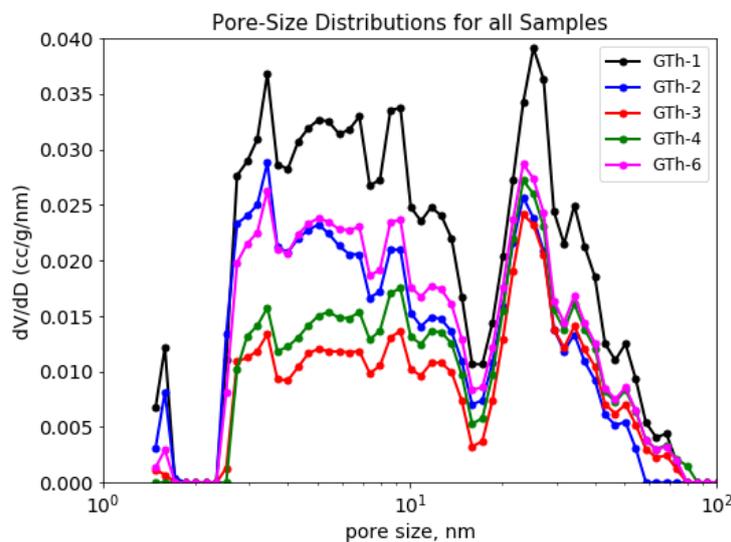
Figure 2.6: Pore-size distributions based on low-pressure nitrogen adsorption

2.4.4 Relationship between Geochemical Properties and Mineral Compositions

The ternary plot in Figure 2.7 shows a binary classification in the distribution of carbonates with depth. For depths up to 1478m (that is samples GTh-1 through GTh-4), the carbonates are relatively low compared to the amount of the brittle minerals (quartz and K-feldspar) indicating that these samples are more brittle and, except for the high clay contents, should be good candidates for hydraulic fracking. Conversely, the remaining samples (GTh-5 through GTh-8) have carbonate contents comparable to the amount of their brittle minerals indicating that the expected brittleness might be neutralised by the high ductile strength of the carbonates. Consequently, the suitability of the samples for hydraulic fracking would depend largely on their clay contents.

Figure 2.8 shows that the illite/mica dominates the clay minerals for all the samples with kaolinite and chlorite only existing in limited amounts. Among other geological and depositional considerations, the abundance of the illite/mica in these shales can explain the low values of the TOC contents observed in some of the samples. Illite can precipitate and block off small organic pores (Pevear, 1999). This is supported by the negative trend observed in Figure 2.9 between TOC content and illite/mica content.
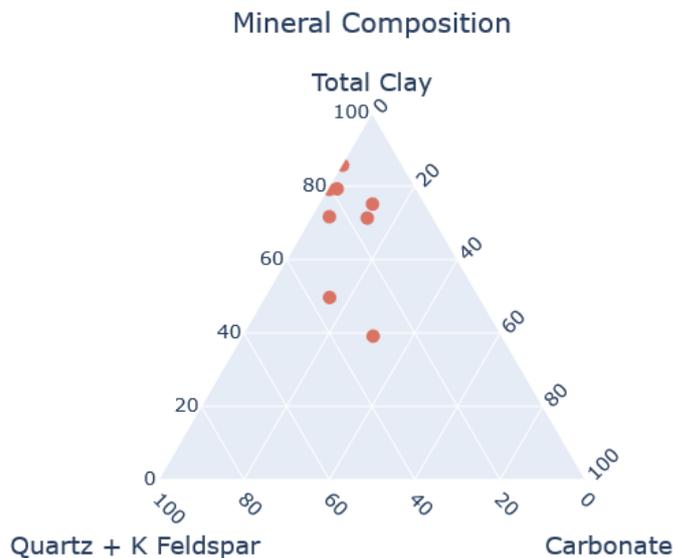
Figure 2.7: Ternary plot of samples' mineral compositions
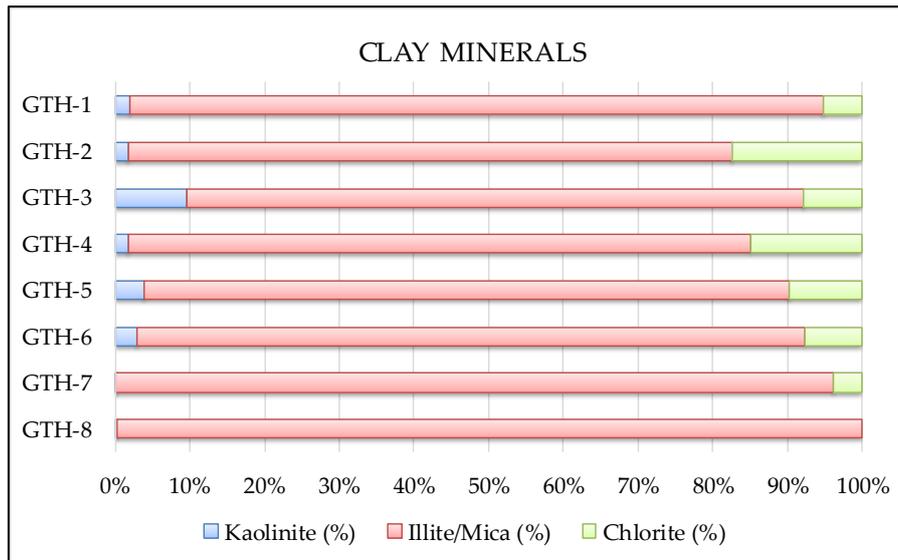
Figure 2.8: Composition of total clay minerals in study samples
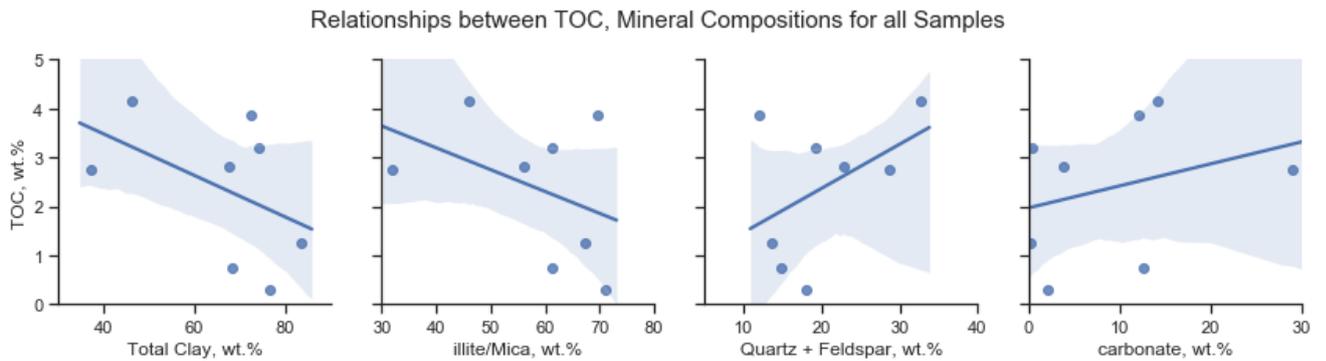
Figure 2.9: Relationships between TOC Contents and Mineral Compositions with 95% Confidence Intervals

Figure 2.9 clearly shows that no correlational relationships can be established between TOC content and any of the inorganic components of the shale samples. This attests to the vertical heterogeneity in reservoir qualities and might be due to the presence of thin laminates intermittently found at different depths in this Formation. Lastly, the vertical or stratigraphic trends of the source rock characteristics are shown in Figure 2.10. This Figure shows that the middle and lower section of the Goldwyer Formation exhibits better source rock characteristics than the upper section. While the need for more samples from the upper and middle sections of the Formation is acknowledged, the findings in this study clearly indicate the lower Goldwyer Formation may contain better source rock qualities than previously believed.
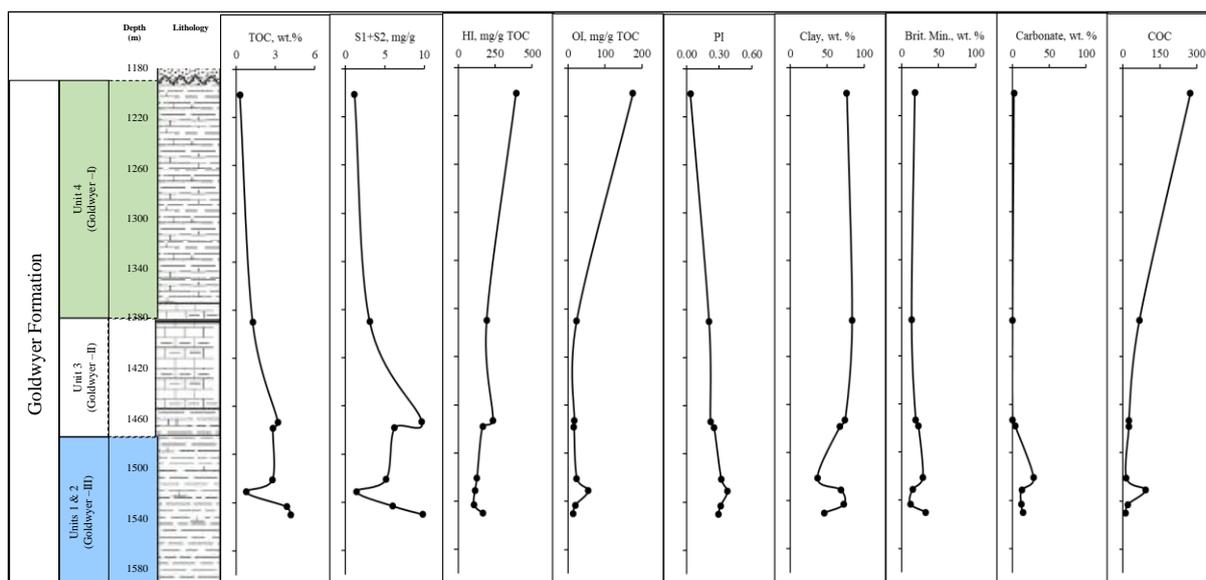
Figure 2.10: Stratigraphic trends of key geochemical properties and mineral contents
(Brit. Min. = Brittleness Minerals = Quartz + K-feldspar)

2.4.5 Relationship between Pore Structural Properties, Geochemical Properties and Mineral Compositions

The nitrogen uptakes (and consequently, the derived PSDs) appear to be negatively influenced by TOC contents. A similar finding has been reported by Guo et al. (2019) in clay-rich Longmaxi shale samples from the Sichuan Basin in China. While this is contrary to most published LPN2-GA results, it is in part due to the effect of the pore blockage by illite in the Goldwyer shales (as previously discussed). Nitrogen adsorption is believed to be controlled by the abundance of micropores and mesopores which are believed to be related to organic matters (Guo et al., 2019), hence the positive correlations found in the literature between nitrogen uptakes and TOC content. However, Goldwyer shales are clay-dominated and it has been reported that a larger portion of the mesopores are controlled by clay minerals (Yuan et al., 2019). Also, (most) clay minerals are polar and have strong affinity for polar molecules (Thompson and Goyne, 2012). Although nitrogen does not have dipole moments, it has an effective quadrupole moment (Buckingham et al., 1968) which explains why the columbic law is often included in the force-fields for molecular simulation of nitrogen (Coasne et al., 2010). It is therefore possible that the contributions of the clay minerals to nitrogen adsorption in these samples superseded that of organic matters leading to the observed deviation from the commonly observed trends between nitrogen uptakes and TOC contents. Moreover, the samples have lower quantities of

quartz and feldspar and are therefore prone to higher mechanical compaction which might reduce the pore spaces available to nitrogen (Guo et al., 2019).

The above discussion suggests that the low-pressure nitrogen sorption processes are controlled by a combined effect of both the organic matter and mineral composition of the shale samples. To capture this interplay, we employed the ratio of clay-content to TOC content (subsequently referred to "clay to organic carbon, COC" defined by Equation 2.2) which was first introduced by Liu et al. (2008) and hitherto referred to as RCO.

$$COC = \frac{Total\ Clay\ Content}{TOC\ Content} \qquad\qquad 2.2$$

Figure 2.11 shows a plot of COC as a function of TOC content for the eight samples used in this study and another plot for seventy-seven data points from the literature. The published data (shown in Table A1, appendix A) included in this plot have TOC contents ranging from 0.12 wt.% to 7.74 wt.% and clay contents from 14.2 wt.% to 72 wt.%, covering the ranges of properties of the samples studied in this work. It is clear from this Figure that a strong correlation exists between COC and TOC contents even when there is no significant relationship between TOC and clay contents as in the case in this study. Therefore, COC would be a better parameter to correlate with properties like surface area, pore volume, and gas contents when one or both TOC and clay contents fail to yield a reliable correlation.
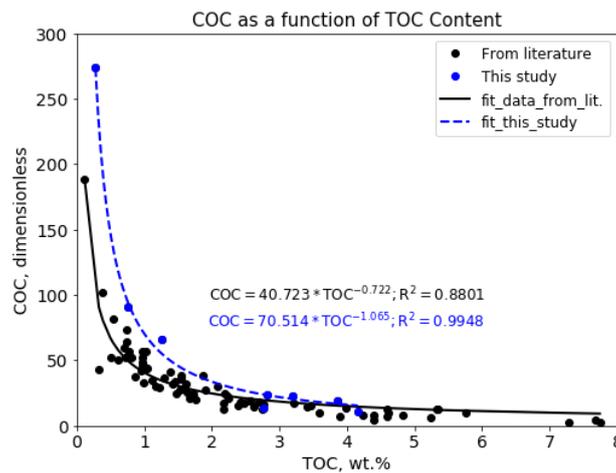
Figure 2.11: Relationship between COC and TOC Content

As shown in Figure 2.12, BET-Surface areas and total pore volumes show negative correlations with the TOC contents, no appreciable correlation with clay contents was observed. However, COC shows positive correlations with both surface area and pore volume, with accuracies

comparable to (or better than) those of the correlations with the TOC contents. This observation agrees with our postulation about the use of COC as a single predictor of surface area and total pore-volume when either TOC or clay content fails to give a satisfactory correlation with these properties.
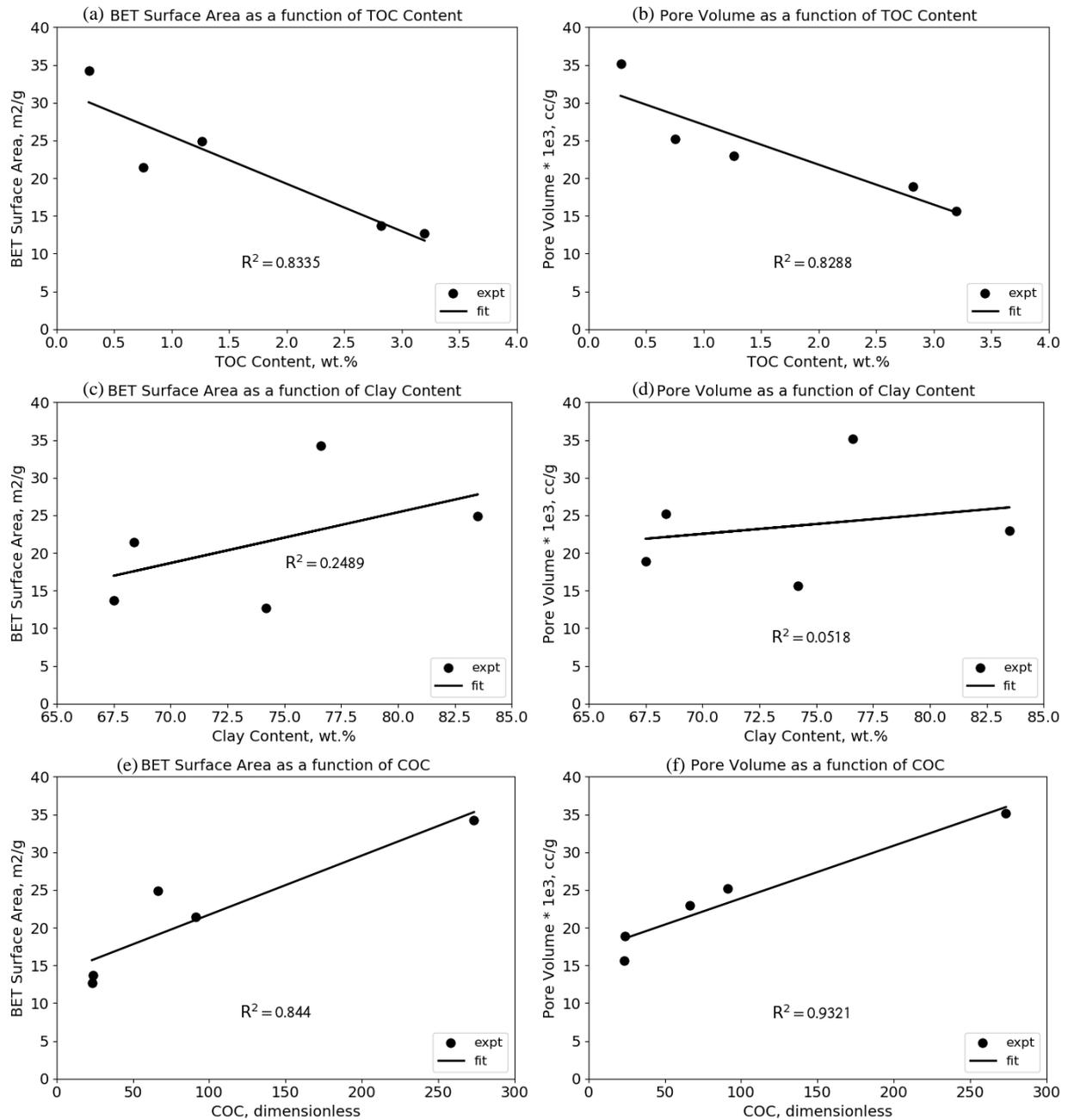
Figure 2.12: Relationships between pore structural properties and TOC contents (a & b), clay contents (c & d), and COC (e & f).

2.5 Conclusions

Characterization of shale samples from the Goldwyer Formation is presented based on the results of the geochemical analysis, XRD analysis and low-pressure nitrogen adsorption experiments conducted on eight samples selected across the three sections of the Formation. The rock properties are found to vary stratigraphically from the upper to the lower sections of the Formation. The samples are composed of varying amounts of inorganic components, such as quartz, feldspar, pyrites, and carbonates, and relatively high clay contents, predominantly illite/mica with small amounts of kaolinite and chlorites. TOC contents in these samples appeared to be negatively, albeit weakly, correlated with the clay and illite contents but no appreciable correlation with other inorganic components was observed. Contrary to most published shale rocks around the world, these Ordovician Goldwyer shale samples studied here exhibited pore characteristics that are highly negatively correlated with TOC contents and show very weak to no correlations with clay contents. Lastly, the parameter (COC) used a single predictor to correlate with structural properties (surface areas and total pore volumes) showed strong positive correlations with accuracies comparable to those of correlations with TOC content.

Chapter 3

High-Pressure Volumetric Measurements of Methane Sorption Isotherms – Effect of Equation of State

3.1 Introduction

Adsorbed gas represents a significant proportion of the total gas in place in coal seams and gas shale (Curtis, 2002) due to their characteristic pore structures and mineral make-ups (Leahy-Dios et al., 2011, Didier et al., 2014). Hence, investigations, mostly experimental, of adsorption capacities of coal samples to methane have been widely explored (Bell and Rakop, 1986, Wei et al., 2017b, Wei et al., 2013, Zhang and Liu, 2016). Menon (1968) discussed different approaches for laboratory measurements of high-pressure gas-solid sorption isotherms. These include the glass-piezometric method used for methane-coal sorption studies up to 50 MPa, Mitchel's modified glass-piezometric method for gas-solid sorption and general PVT studies up to 300 MPa, modified gas-chromatographic method for both pure and multicomponent gas-solid sorption studies up to about 14 MPa and the modified gravimetric method used for methane-silica gel up also up to 14 MPa (Menon, 1968). More recently, Keller and Staudt (2005) also discussed in details, several experimental approaches for measuring gas-solid sorption isotherms. These include the volumetric method, the manometric method, the gravimetric method, the rotational oscillometric method, the impedance spectroscopic or dielectric method, and some combinations thereof (Keller and Staudt, 2005).

Based primarily on its simplicity (Keller and Staudt, 2005), the volumetric method seems to have gained a wider acceptance among researchers. Zhang and Liu (2016) used the volumetric method to measure isotherms for different coal samples using subcritical CO_2 gas & supercritical methane with a focus on sorption hysteresis (Zhang and Liu, 2016). Busch et al. (2005) also used the volumetric approach for CO_2 and CH_4 adsorption isotherms on coal up to 23 MPa and 45 °C (Busch et al., 2005). Gasparik et al. (2012) measured shale gas adsorption up to 25 MPa using the volumetric method at 65 °C. Simply put, the volumetric method operates primarily on gas expansion and equilibration processes resulting in a pressure profile that is converted to amounts using the ideal gas equation corrected for non-ideality by real gas compressibility (Z-) factors calculated with a chosen equation of states (EOS) (Goodman et al., 2004). Volumetric balance at each equilibrium pressure step allows for the calculation of adsorbed gas volume. Despite its wide use, there is no known standard for reporting measured data (Goodman et al., 2004). This lack of reporting standard for high-pressure volumetrically

measured gas/solid sorption isotherms has made it nearly impossible to compare or reproduce, with any degree of certainty, reported data (Gasparik et al., 2014b, Gensterblum et al., 2010, Goodman et al., 2004). One obvious issue identified from published reports is the varied (and sometimes inconsistent) use of EOSs. For example, Tang et al. (2015) measured the adsorption of methane on coal by volumetric approach up to 9 MPa and calculated the Z-factors of methane using Redlich-Kwong EOS (Tang et al., 2015). Zhang et al. (2015b) applied a 32-parameter modified Benedict-Webb-Rubin (MBWR) EOS for their data interpretation in a similar study with coal. In a more recent study with shale, Yang et al. (2018a) used McCarty and Arp EOS to calculate the Z-factors of helium for void space calculations and Setzmann and Wagner EOS for Z-factors of methane (Yang et al., 2018a).

While various explanations have been attempted to explain some of the commonly observed anomalies in high-pressure sorption isotherms (for example, observations of hysteresis loops in high-pressure supercritical methane isotherms (Bell and Rakop, 1986, Wei et al., 2017b, Wei et al., 2013, Zhang and Liu, 2016, Rajniak and Yang, 1993), observations of reducing amounts adsorbed at medium to high pressure especially in coals and shale rocks (Lutynski et al., 2011, Zhang et al., 2015b), little has been reported on equation of state as a potential (or primary) reason for some (or all) of these observations. To demonstrate the effect of Z-factor on CO_2 excess adsorption, Goodman et al. (2004) compared the ideal isotherm (one obtained with Z = 1) with those calculated using Z-factor from two other sources (Span & Wagner's and Gas Encyclopaedia) and found that CO_2 excess adsorption is much lower for the ideal case. Lutynski et al. (2011) investigated the effect of equations of state on the adsorption of supercritical CO_2 by comparing the performances of PR-EOS and SRK-EOS with Span and Wagner's EOS (SW-EOS). The authors found that both PR-EOS and SRK-EOS gave unrealistically higher results above the critical pressure (7.39 MPa) following lower results at subcritical pressures and attributed these discrepancies to errors in density calculations by these EOS relative to SW-EOS (Lutynski et al., 2011). Al-Fatlawi et al. (2017) have also reinstated the need for accurate predictions of Z-factors for gas reserves estimations, which is one of the direct applications of gas adsorption.

Hysteresis in high-pressure sorption isotherms of supercritical methane on coals and shales has become a common observation and yet, it remains difficult to explain. Some researchers believe it is caused primarily by measurement uncertainties (Ozdemir, 2017, Bell and Rakop, 1986, Dutta et al., 2011) while others have argues that it could be too significant to be attributed to measurement errors alone (Bell and Rakop, 1986). Parameters such as equilibrium time

(Battistutta et al., 2010, Keller and Staudt, 2005), (residual) moisture contents of coal (Goodman et al., 2004, Battistutta et al., 2010), coal ranks (Busch et al., 2003, Goodman et al., 2004), particle sizes of coal (Feng et al., 2016, Zhang et al., 2014), irreversible structural changes to the adsorbent due to gas adsorption (Zhang and Liu, 2016, Liu et al., 2017b), irreversible absorption associated with gas adsorption (Dutta et al., 2011, Weishauptová et al., 2015), surface heterogeneity (Jessen et al., 2008), gas trapping (Goodman et al., 2004), irreversible chemical bonding of gas molecules with molecules of the adsorbent (Battistutta et al., 2010, Dutta et al., 2011, Zhang and Liu, 2016) and selectiveness of adsorption sites during desorption (Zhang and Liu, 2016) have been offered as explanations for observed high-pressure CO_2 and CH_4 sorption hysteresis.

It is generally believed that, where hysteresis exists, desorption isotherms should lie above their adsorption counterparts. This type of hysteresis is referred to as "positive hysteresis" (Kim et al., 2011) and was the case with all the examples cited above. Less commonly, cases of "negative hysteresis" and cross-overs (desorption isotherm intercepting adsorption isotherm) have also been reported (He et al., 2010, Keller and Staudt, 2005, Kim et al., 2011, Rodrigues et al., 2018). However, it was hitherto believed that such observations could only be caused by pressure non-equilibration, desorption of pre-adsorbed gas in the adsorbent (Keller and Staudt, 2005), or irreversible structural changes to the solid as a result of gas adsorption (He et al., 2010, Kim et al., 2011).

From the above discussion, it is obvious that there is no single universal explanation for CO_2 or CH_4 sorption hysteresis at high-pressure. A similar conclusion was made by Wang et al. (2014b) in their review paper on sorption hysteresis of CO_2 and CH_4 on coals. It is noteworthy, however, that majority of the articles reviewed were based on the volumetric/manometric method. This invariably means that the authors used some equations of state to obtain the fluid data required for experimental data analysis. Interestingly, none of the authors considered that the choice of EOSs (and hence, calculated Z-factors) could be the cause of the observed hysteresis.

This chapter presents a comparison of the performances of different equations of state relative to a combination (subsequently referred to as NIST-refprop) of McCarty & Arp EOS (for helium) (McCarty and Arp, 1990) and Setzmann & Wagner's EOS (Setzmann and Wagner, 1991) (for methane) in high-pressure volumetric measurements of methane adsorption on a coal sample. It focuses on establishing that the choice of EOS can significantly affect the

volume of free space, the calculated isotherms and their associated model parameters, the size and type of hysteresis between the resulting adsorption and desorption isotherms (if any), as well as estimated gas reserves. The coal sample used here is a medium-ranked, volatile bituminous coal, selected to eliminate complications that may be introduced by the complex microstructures of shale rocks and isolate the effects of fluid density on the final isotherms.

3.2 Equations of State

The thermodynamic state of a system is often defined in terms of the relationship between its pressure (P), temperature (T), and molar volume (v_m) such that:

$$f(P, T, v_m) = 0 \qquad\qquad 3.1$$

This relationship is referred to as the equation of state (EOS) (Kikic, 2005). By solving Equation 3.1 for v_m for a given system over a range of pressure and temperature conditions, other physical properties such as the compressibility factor, enthalpy, entropy, fugacity, etc. as well as the phase equilibrium of the system can be calculated (Jia et al., 2016). Equations of state are empirically classified as cubic and non-cubic based on the degree of the polynomic function (Kikic, 2005) represented by Equation 3.1. In this paper, only the cubic EOS of Peng-Robison's (PR) and the Soave-Redlich-Wonk (SRK) and their volume translated forms (Pedersen and Christensen, 2007, Péneloux et al., 1982) are discussed. Also, Soave's modified Benedict-Webb-Rubin's (SBWR) (Soave, 1999) and Lee-Kesler's (Lee and Kesler, 1975) equations of state are the only non-cubic equations of states discussed in this paper. The details of these equations of state are included in *appendix B*.

3.3 Materials and Methods

3.3.1 Sample

The coal sample used in this study is ranked medium volatile bituminous with a mean vitrinite reflectance of 1.43%. The results of the sample's petrographic and proximate analyses are summarized in Table 3.1. The sample was pulverized and sieved to particle sizes 45−75 μm (325-200 mesh) and then subjected to low-pressure nitrogen adsorption to determine its pore-size distributions (PSDs).

Table 3.1: Properties of coal sample

Components	Composition (%)
A. Petrographic Analysis	
Vitrinite	75.0
Fusinite	3.3
Semi-fusinite	13.0
Macrinite	0.3
Inertodetrinite	4.0
Mineral matter	4.5
Mean maximum reflectance	1.43
B. Proximate Analysis	
Ash content	9.6
Moisture content	1.2
Volatile matter	21.2
Fixed carbon	68.0

3.3.2 Measurement of Methane Sorption Isotherms

Methane adsorption and desorption isotherms were measured at 25°C and 40°C using Particulate System's HPVA-II® 200 unit described in (Zhang et al., 2015b, Zou and Rezaee, 2016b, Zou et al., 2017, Ekundayo and Rezaee, 2019a). The fully automated HPVA can measure up to 500 $^{\circ}$C temperature and 20 MPa pressure (Micromeritics, 2013) and it uses NIST's refprop® to calculate the Z-factors used in generating the isotherms. It also logs the pressure and temperature data at specified intervals thereby allowing the user to perform their own calculations. In this work, the data logged by the equipment was used to calculate adsorption and desorption isotherms with Z-factors obtained from each of the equations of states identified in section 3.2. Some schematics and descriptions of the HPVA-II 200® unit, its data interpretation approach and typical experimental procedures have been discussed by Zhang et al. (2015b); Zou and Rezaee (2016b), Zou et al. (2017). As much as possible, we have also used similar notations as these authors to make a comparison of our analysis and theirs easy for readers.

Figure 3.1 shows the schematic of a typical pressure-time profile for a complete adsorption-desorption experiment using the HPVA-II 200. The pre-adsorption steps are usually performed to obtain the volume of the free-space needed for subsequent calculations and to stabilize the sample cell at the experimental temperature. For any two consecutive adsorption steps $i - 1$ & i (as illustrated in *Figure C1* in *Appendix C*), the differential and cumulative amounts adsorbed (at any step r), per unit mass of the adsorbent, can be calculated using *Equations 3.2 and 3.3* below (details of derivation are available in *Appendix C*).

$$\Delta \tilde{V}^{ads,i} = \frac{V_{STP}}{RM_s} \left[\left(\frac{P_{mA}^i V_{man}}{T_{mA}^i Z_{mA}^i} - \frac{P_{mB}^i V_{man}}{T_{mB}^i Z_{mB}^i} \right) - \left(\frac{P_{sc}^i V_{sc}}{T_{sc}^i Z_{sc}^i} + \frac{P_{sc}^i V_{us}}{T_{us}^i Z_{us}^i} + \frac{P_{sc}^i V_{ls}}{T_{ls}^i Z_{ls}^i} \right) \right.$$
$$\left. + \left(\frac{P_{sc}^{i-1} V_{sc}}{T_{sc}^{i-1} Z_{sc}^{i-1}} + \frac{P_{sc}^{i-1} V_{us}}{T_{us}^{i-1} Z_{us}^{i-1}} + \frac{P_{sc}^{i-1} V_{ls}}{T_{ls}^{i-1} Z_{ls}^{i-1}} \right) \right] \qquad 3.2$$

$$\tilde{V}_r^{ads} = \sum_{i=1}^{r} (\Delta \tilde{V}^i) \qquad\qquad 3.3$$

P_{mA}, T_{mA} & Z_{mA} in *Equation 3.2* are respectively the initial pressure, temperature and Z-factor of the reference cell (of volume, V_{man}) before dosing gas into the sample cell, P_{mB}, T_{mB} & Z_{mB} represent the conditions of the reference cell after dosing. P_{sc}, T_{sc} & Z_{sc} are the equilibrium pressure, temperature, and corresponding Z-factor in the sample cell (of volume V_{sc}), T_{us} & Z_{us} are the temperature and Z-factor in the upper stem (of volume, V_{us}) of the sample holder while T_{ls} & Z_{ls} are the temperature and Z-factor in the lower stem (of volume V_{ls}) of the sample holder. V_{STP}, R and M_s are respectively the molar volume of gas at standard conditions, gas constant ($\approx 8.3145 \, Jmol^{-1}K^{-1}$) and mass of the adsorbent.

The equipment uses a helium expansion method to measure the volume of free space which includes the volumes of the lower and upper parts of the stem (that is, V_{ls} & V_{us} respectively) connecting the sample cell to the reference cell. The details of this measurement technique have been discussed by Zhang et al. (2015b), Zou and Rezaee (2016b), Zou et al. (2017) and are also discussed in *Appendix C*. The volume free space at ambient condition (V_{Amfs}) is given as follows:

$$V_{Amfs} = V_{sc} + V_{ls} + V_{us} \qquad\qquad 3.4$$

Where:

$$V_{Amfs} = \frac{T_{sc}^{He} Z_{sc}^{He}}{P_{sc}^{He}} \left(\frac{P_{mA}^{He} V_{man}}{T_{mA}^{He} Z_{mA}^{He}} - \frac{P_{mB}^{He} V_{man}}{T_{mB}^{He} Z_{mB}^{He}} - \frac{P_{sc}^{He} V_{us}}{T_{us}^{He} Z_{us}^{He}} + \frac{P_{sc}^{He} V_{us}}{T_{sc}^{He} Z_{sc}^{He}} \right) \qquad 3.5$$

The parameters in *Equation 3.5* are defined similar to those in *Equation 3.2*.

These equations were used to calculate the amounts adsorbed per unit mass which were plotted against corresponding equilibrium pressures to obtain the adsorption isotherms. One important assumption made in using *Equations 3.2 & 3.3* is that $P_{sc}^0 = 0$ since the system is expected to be fully evacuated prior to the first adsorption step.
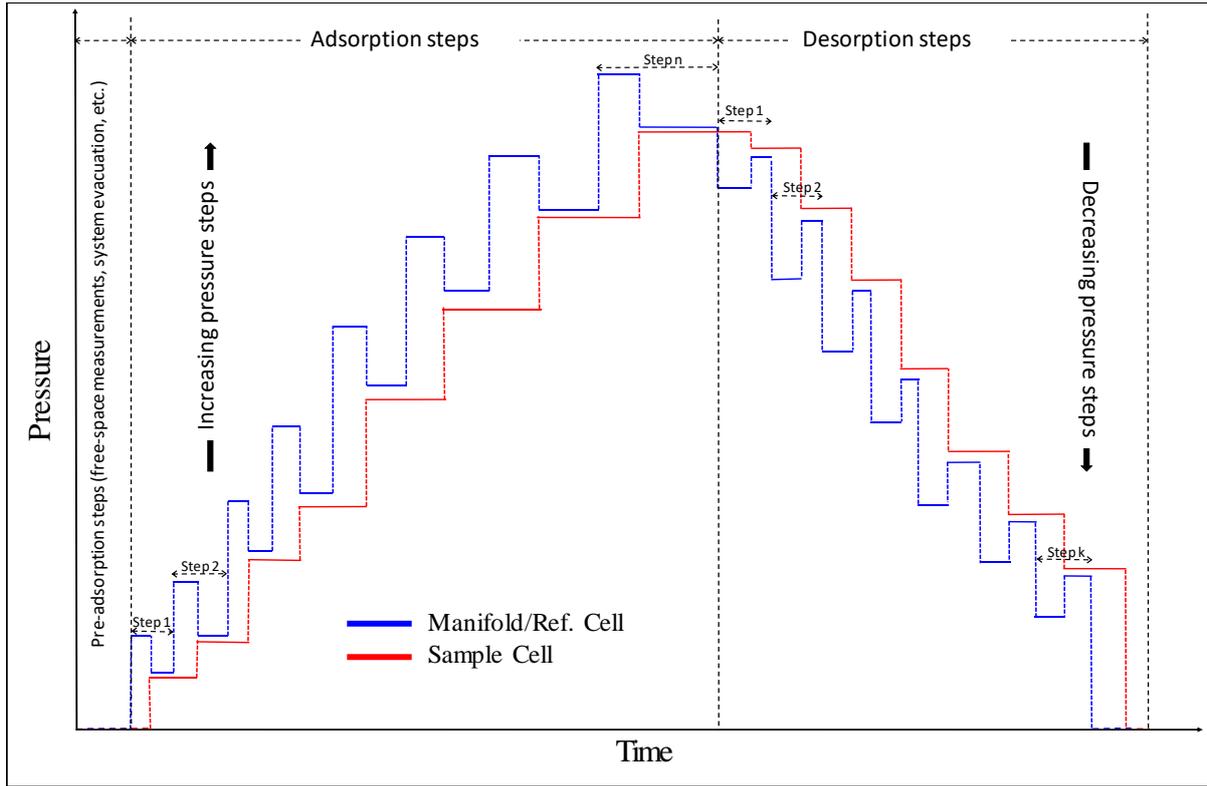
Figure 3.1: Typical pressure-time plot for a HPVA adsorption-desorption experiment

If the amounts adsorbed at any two consecutive adsorption steps $i-1$ and i are $\tilde{V}_{i-1}^{ads}$ and $\tilde{V}_{i}^{ads}$ respectively, then the differential amount adsorbed at step i (as shown in Equation 3.2) can be written as:

$$\Delta \tilde{V}_{i}^{ads} = \tilde{V}_{i}^{ads} - \tilde{V}_{i-1}^{ads} \qquad\qquad 3.6$$

Thus, the target amount during the desorption from step i to $i-1$ is $\Delta \tilde{V}_{i}^{ads}$. In practice, however, the desorption step terminates at a new pressure point j (typically, $P_{i-1} < P_j < P_i$) desorbing an amount $\Delta \tilde{V}_{j}^{des}$. Therefore, the amount adsorbed at the pressure point P_j is given as:

$$\tilde{V}_{j}^{ads} = \tilde{V}_{i}^{ads} + \Delta \tilde{V}_{j}^{des} \qquad\qquad 3.7$$

A plot of $\tilde{V}_{j}^{ads}$ against P_j on the same axes as the adsorption isotherm gives the desorption isotherm. In a rare case where $P_j = P_{i-1}$, $\left|\Delta \tilde{V}_{j}^{des}\right| = \Delta \tilde{V}_{i}^{ads}$. For this ideal case, the isotherms do not only overlay, they are also equal. However, in reality, $P_j \neq P_{i-1}$ and $\left|\Delta \tilde{V}_{j}^{des}\right|$ may be less or greater than $\Delta \tilde{V}_{i}^{ads}$ resulting in one of three scenarios:

1. *Negligible (or Zero) Hysteresis* in which the isotherms overlay even though $\left|\Delta \tilde{V}_{j}^{des}\right| \neq \Delta \tilde{V}_{i}^{ads}$.

32

2. *Positive Hysteresis* in which $\left|\Delta \tilde{V}_j^{des}\right| < \Delta \tilde{V}_i^{ads}$ and as such, desorption isotherm lies above the adsorption curve

3. *Negative Hysteresis* in which $\left|\Delta \tilde{V}_j^{des}\right| > \Delta \tilde{V}_i^{ads}$ and as such, desorption isotherm lies below the adsorption curve

3.4 Isotherm Parameterisation and Application

3.4.1 Isotherm Modeling

The measured excess adsorbed amounts are usually converted to absolute amounts, which are needed for practical applications (Gasparik et al., 2012). In this study, the measured isotherms were parameterized using the three-parameter Langmuir model (Gasparik et al., 2012, Zhang and Liu, 2016, Zhang et al., 2015b, Gasparik et al., 2014b) which includes a factor to convert the excess amount adsorbed to the absolute amount. If the excess amount at any equilibrium pressure, P is V_{exc}, then the model is given as:

$$V_{exc} = \frac{V_L P}{P + P_L}\left(1 - \frac{\rho_{bulk}}{\rho_{ads}}\right) \tag{3.8}$$

Where:

V_L, P_L = Langmuir volume and pressure (respectively)

ρ_{ads} = Adsorbed gas phase density

$$\rho_{bulk} = \frac{PM}{ZRT} = \text{ Density of the bulk gas phase} \tag{3.9}$$

M = Molecular weight of methane

The model parameters ($V_L, P_L, and\ \rho_{ads}$) were determined by non-linear curve fitting using the trust region reflective algorithm implementation in Scientific Python (SciPy) to allow for the parameters to be bounded to non-negative values. Each of the parameters is thus bounded to $(0, +\infty)$. The quality of the match with experimental isotherms has been assessed using the coefficient of determination, R^2 defined as:

$$R^2 = 1 - \left(\sum_{i=1}^{i=n}\left(V_{expt}^i - V_{fit}^i\right)^2 \middle/ \sum_{i=1}^{i=n}\left(V_{expt}^i - \bar{V}_{expt}\right)^2\right) \tag{3.10}$$

Where V_{expt}^i is the experimental amount adsorbed at step i ($i = 1, 2, 3, ..., n$); V_{fit}^i is the corresponding amount adsorbed calculated with *Equation 3.8* and $\bar{V}_{expt}$ is the mean experimental amount adsorbed given as:

$$\bar{V}_{expt} = \sum_{i=1}^{i=n} \left(V_{expt}^i \right) \Big/ n \qquad\qquad 3.11$$

3.4.2 Gas in-Place Calculation

The total volume of gas originally in-place, in a coal-seam, is the sum of the free gas and adsorbed gas and can be calculated using *Equation 3.12* (Seidle, 2011a):

$$Gi = Ah \left[\frac{43560 \emptyset_i (1 - S_{wi})}{B_{gi}} + 1359 \rho_{rock} \frac{V_L^{res} P_i}{P_i + P_L^{res}} \right] \qquad\qquad 3.12$$

In this equation, A (acre) is the area of the coal seam, h (ft) is the thickness, $\emptyset_i, S_{wi}$ represent the respective initial porosity and water saturation in the cleat system, ρ_{rock} (g/cc) is the density of the coal seam, P_i (MPa) is initial reservoir pressure, B_{gi} (rcf/scf) represents the initial gas Formation volume factor (FVF) calculated from *Equation 3.13*, V_L^{res} (scf/ton) is the Langmuir volume for the adsorption isotherm at reservoir temperature, T_{res} (°C) & P_L^{res} (MPa) is the corresponding Langmuir pressure. Table 3.2 shows the parameters used in calculating the OGIP for each EOS.

$$B_{gi} = \frac{0.000195 \, Z_i (1.8 T_{res} + 492)}{P_i} \qquad\qquad 3.13$$

Z_i = Z-factor of methane at initial coal seam pressure and temperature

It is obvious from *Equation 3.13* that the gas FVF is directly related to Z- factor and as such is also EOS-dependent. To isolate the effect of the gas FVF on the calculated volume of gas in-place, two different cases were investigated as follows:

Case 1: Gas FVF equals the value calculated for each EOS.

Case 2: Gas FVF equals constant for all EOS. The constant value was set as the value obtained for the reference EOS.

Table 3.2: Parameters used for initial gas reserves estimates

Parameters	
Reservoir Temperature, $^{\circ}$C	40
Initial Res. Pressure, MPa	10.34
Rock density, g/cc	1.34*
Initial porosity, fraction	0.1*
Initial water saturation, fraction	0.8*

* data from Rodrigues et al. (2018)

3.5 Results and Discussion

3.5.1 Low-Pressure Nitrogen Sorption Isotherms and Pore-Size Distribution

Figure 3.2 shows the low-pressure nitrogen sorption isotherms (Figure 3.1a) and the corresponding pore-size distribution, PSD (Figure 3.1b) for the sample. The nitrogen adsorption isotherm shows no monolayer coverage but exhibits a significant multilayer coverage (Thommes et al., 2015), up to relative pressure of about 0.8, followed by a sharp increase in the amount adsorbed (an indication of capillary condensation (Jun-yi et al., 2014) thereafter. Negligible hysteresis of type H3 (IUPAC classification, (Thommes et al., 2015)) characterized by a type II adsorption isotherm and a lower closure of the hysteresis loop indicate that the sample is composed of non-rigid aggregates of slit-like particles and the possible presence of a network of macropores (Thommes et al., 2015). The PSD shows that the sample is composed of approximately bi-modal distributed pores with mesopores accounting for more than 90% of the distribution and dominant pores sizes of approximately 4nm and 25nm. The PSD also shows negligible micropores thereby confirming the absence of monolayer coverage observed in the nitrogen adsorption isotherm.
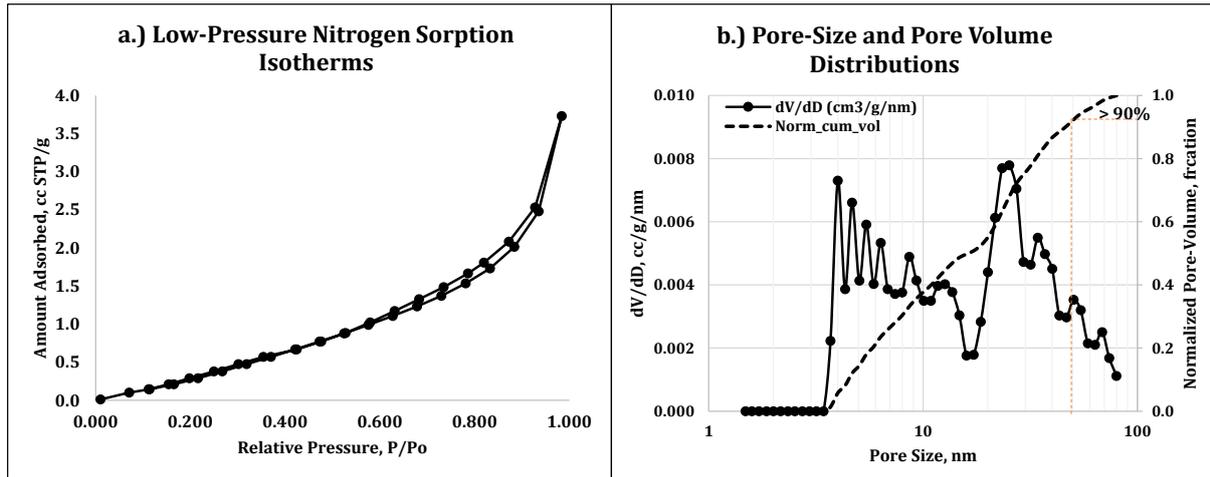
Figure 3.2: Pore-Size Distribution from Low-Pressure Nitrogen Adsorption Data

3.5.2 Methane-Coal Adsorption Isotherms

Figure 3.3a shows the variation in the ambient volume of free-space calculated by different EOSs relative to the value obtained from NIST-refprop. These deviations are directly related to the differences in the Z-factor of helium gas calculated by the different EOSs. As shown in Figure 3.3b, PR-EOS, SBWR-EOS and LK-EOS gave higher helium Z-factors than NIST-refprop, and thus their corresponding ambient volumes of free space are less proportionately. On the other hand, PR-Peneloux-EOS, SRK-EOS, and SRK-Peneloux-EOS gave lower Z-factors of helium compared to NIST-refprop and consequently, their resultants ambient volumes of free space are proportionately larger. All EOSs (except Lee-Kesler) deviated to less than 0.1% compared to the reference EOS. In fact, the deviations are within -0.025% to +0.009% for the cubic EOSs and 0.09% for SBWR-EOS. The greater deviation ($<0.25\%$) observed with Lee-Kesler EOS may be due to its use of linear interpolation to calculate the Z-factor of a fluid from those (Z-factors) of a simple fluid and a reference fluid. The inverse relationship observed between the Z-factor and ambient volume of free space, for each EOS, follows from the gas law ($n = PV/ZRT$). For the same, pressure, volume, and temperature, the amount of gas (n) in a system is inversely related to the Z-factor of the gas which (as shown in Figure 3.3b) is dependent on the choice of EOS.
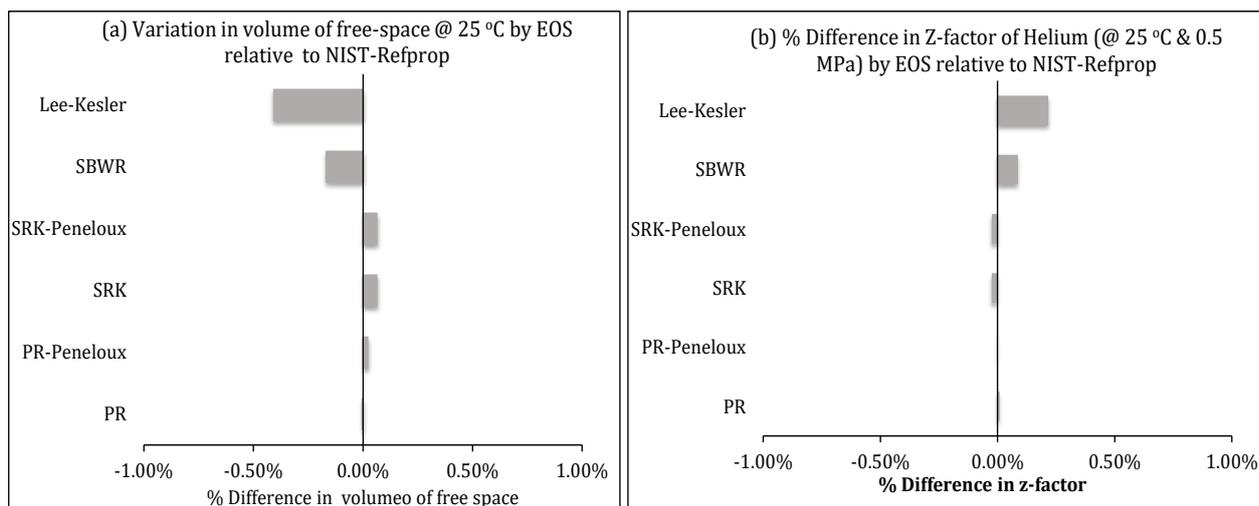
Figure 3.3: **(a)** Variation in the volume of free space by different equations of state (actual free space volumes are in *Figure C1* of *Appendix C*) **(b)** Variation in Z-factor of helium gas by EOS (Reference Z-factor = 1.0023)

It should be noted that the deviations in the volume of free space from NIST-refprop's are not to be considered errors but rather they serve to warn that any reported volume of free space may not be taken as absolute but is highly sensitive to Z-factor (and by implication, EOS). This has implications for the calculated isotherms especially at higher pressures where the amounts of gas adsorbed have been reported to be highly sensitive to the volume of free space (Rouquerol et al., 2016, Do and Do, 2007). A similar observation is made here as shown in Figure 3.4 in which a change of ±0.25% in the ambient volume of free space resulted in ∓10% change in the amount adsorbed at the last equilibrium pressure tested in this paper. While this may be argued to be within the range of uncertainty for this type of measurements, we envisage that the effect may be more pronounced in a shale due to its lower organic matter content (compared to coal). It is illustrated in this paper (see Figure 3.5) that this behaviour is not necessarily connected with pressure equilibrium or any leakage in the system, as is generally believed (Keller and Staudt, 2005), but is predominantly controlled by the EOS used in calculating the Z-factor.
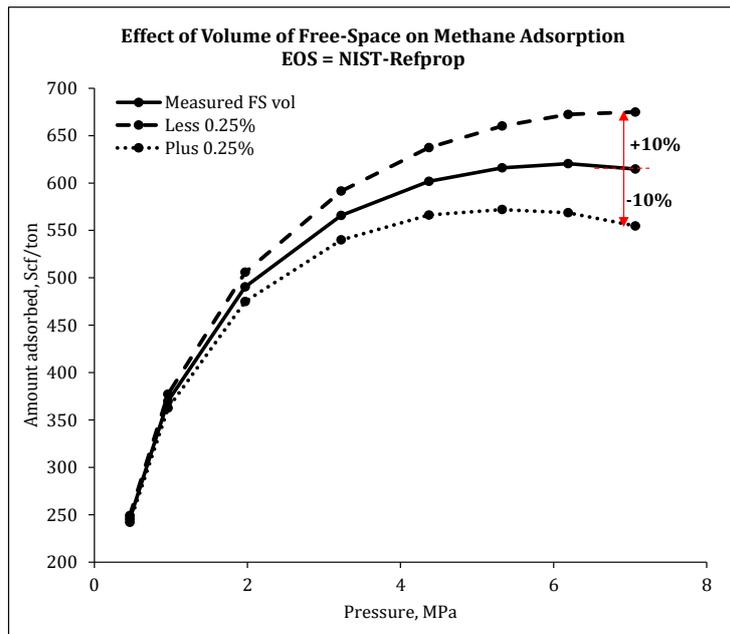
Figure 3.4: Effect of Volume of free space on methane-coal adsorption isotherm at 25 °C
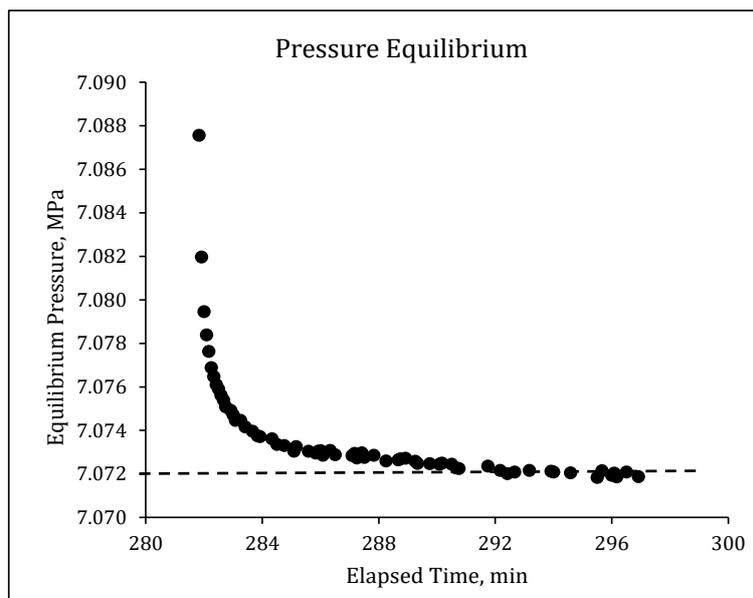
Figure 3.5: Example of pressure equilibration for methane adsorption at 7 MPa & 25 °C

To minimize the error in calculated isotherms due to variation in the volume of free space, Z-factor of methane was calculated with the same EOS used in calculating the Z-factor of helium. The variations in the Z-factors of methane at 25 °C calculated by different EOSs at different equilibrium pressures are shown in Figure 3.6. For each pressure value, SBWR-EOS, followed by LK-EOS, gave the closest Z-factor of methane relative to NIST-refprop's. The deviation from the reference value increases with pressure for each EOS hence, the deviation in the resultant isotherm (shown in Figure 3.7) also increases proportionately with pressure.

Considering the inverse relationship between the Z-factor of gas and the amount of the gas in a system, it is not surprising that PR, PR-Peneloux and SBWR EOSs gave higher methane adsorption isotherms than the reference EOS since their Z-factors are lower (Figure 3.6). For these EOSs, the higher methane adsorption isotherms (compared to the reference EOS) are the results of the combined effects of volume of free space (actually, Z-factor of helium) and Z-factor of methane. PR-EOS and PR-Peneloux EOS gave almost the same volumes of free space as the reference EOS but their significant negative deviations in Z-factor of methane resulted in great amounts adsorbed at each pressure. Similarly, SBWR-EOS which gave a lower volume of free space relative to the reference EOS should ordinarily give much higher amounts of methane adsorbed at each pressure compared to PR-EOS and PR-Peneloux EOSs but for its methane Z-factors which are significantly lower (Figure 3.6) compared to these EOSs. On the other hand, SRK-EOS and its volume-shifted form resulted in lower methane adsorption isotherms compared to the reference EOS. This is expected considering that both the volume of free space and Z-factor of methane from these EOSs are higher compared to the reference EOS. Lastly, the LK-EOS gave higher methane adsorption isotherm compared to the reference EOS despite its higher methane Z-factors. This is because the effect of the Z-factor is counteracted by the lower volume of free space (compared to the reference EOS).

The above observations of combined effects of Z-factors of helium (and methane are also true at 40 ºC (Figure 3.7). The difference, in this case, is the reducing effect of temperature on adsorption isotherms. At higher temperature, lower amounts of methane are adsorbed at each pressure because of the reducing effect of temperature on gas density.
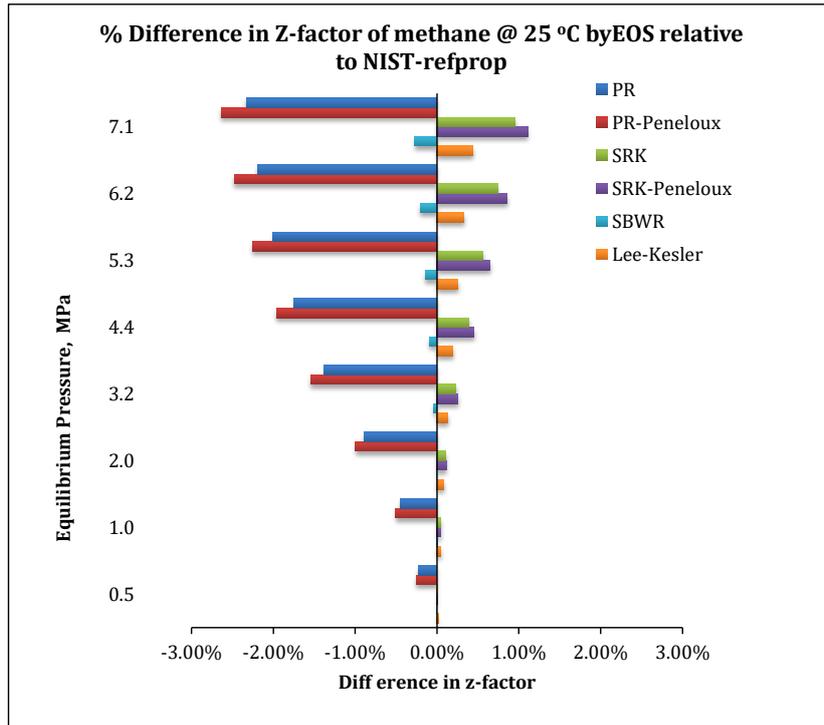
Figure 3.6: Variation in Z-factor of methane at 25°C by different equations of state
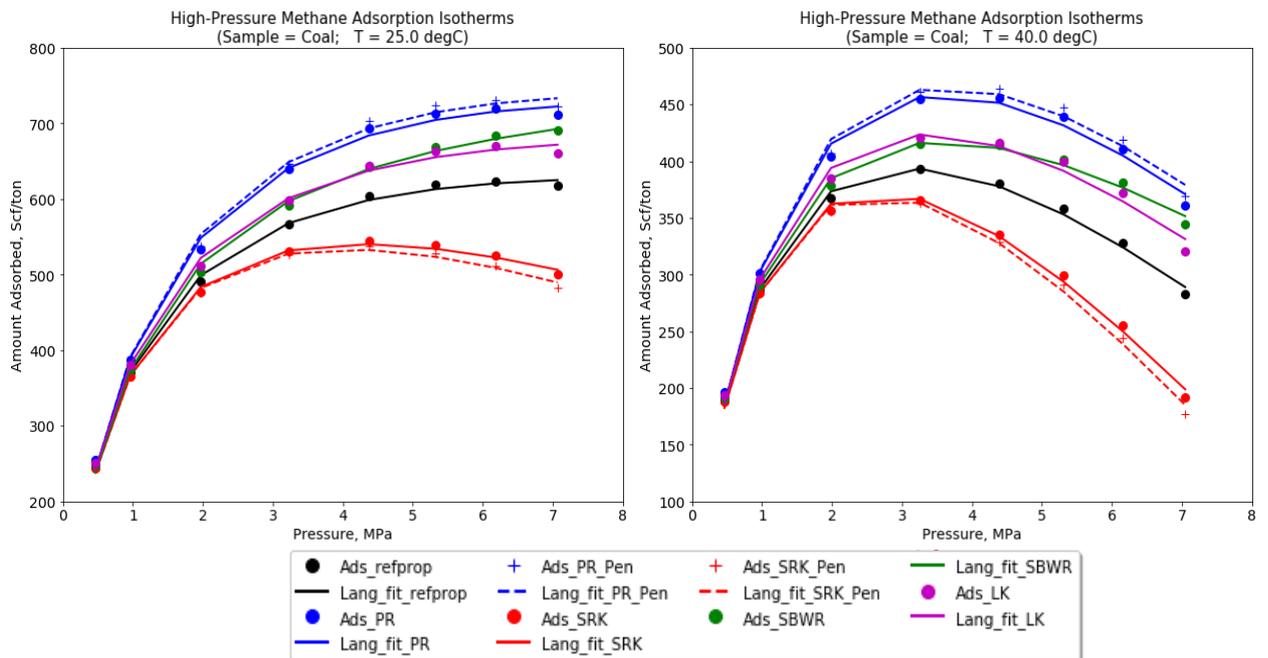
Figure 3.7: Effects of equation of state on methane adsorption capacity of coal

3.5.3 Methane-Coal Desorption Isotherms & Sorption Hysteresis

It is clear from the preceding section that adsorption isotherms from the same experimental data vary significantly for different EOSs. Similar observations are made with desorption isotherms and hysteresis between the adsorption and desorption isotherms. Figure 3.8 shows the adsorption and desorption isotherms for different EOSs. Negligible hysteresis can be seen between the adsorption and desorption isotherms for NIST-refprop® at both temperatures. For the measurements at 25°C, the desorption isotherm is slightly lower than the adsorption isotherm for most test pressures (Figure 3.8a). Although the reason for this behavior is not clear, it is unlikely due to any significant irreversible structural changes to the coal sample, as postulated by He et al. (2010), given the near negligible difference between the isotherms. Also, pressure equilibrium was achieved (as shown in Figure 3.9) for each desorption step, therefore, pressure non-equilibration was also ruled out as a reason for this anomaly. Thus, it is assumed that this observation may be related to measurement uncertainties especially fluctuations in experimental temperature.
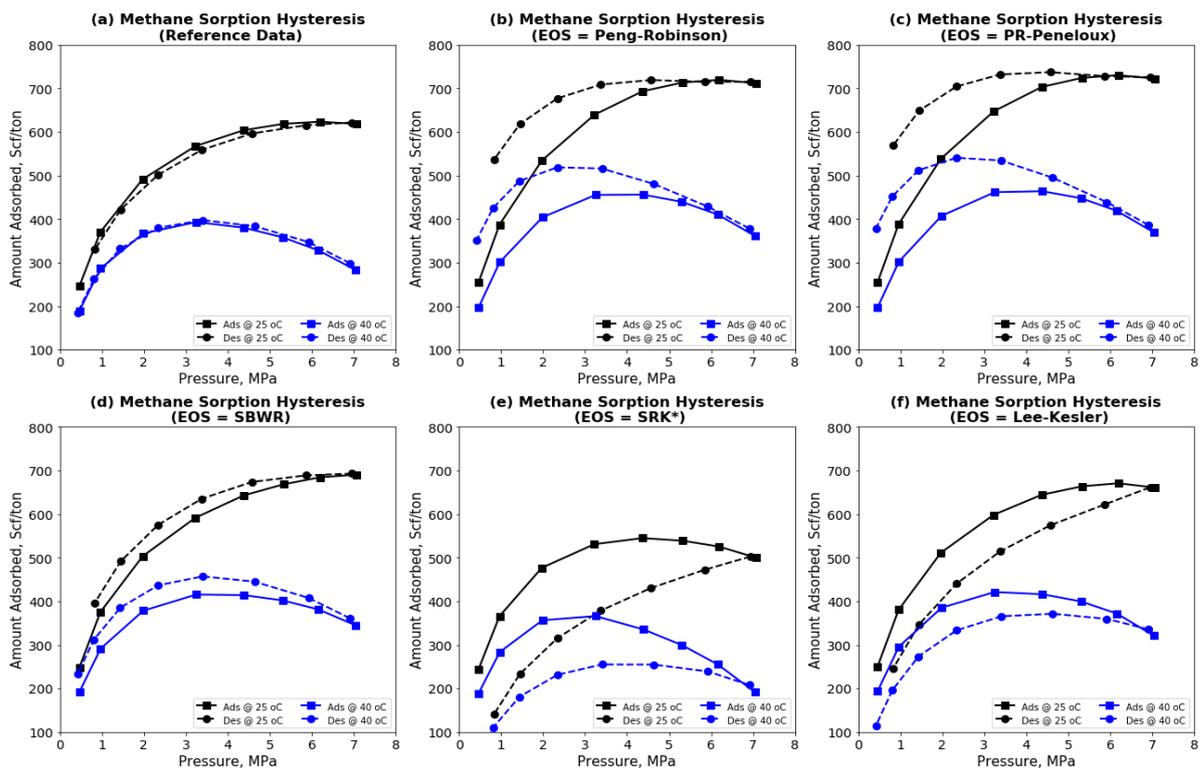
Figure 3.8: Methane-coal sorption hysteresis by equation of state (* SRK-Peneloux is similar)

Compared to refprop, each of the comparison EOS gave significant differences between the adsorption and desorption isotherms (Figure 3.8b-f) leading to two types of observed sorption

hysteresis. On one hand, EOSs (that is PR-Peneloux, PR-EOS & SBWR-EOS) that gave lower values of Z-factor for methane resulted in positive hysteresis and the more negatively deviated the Z-factors are, the bigger the observed hysteresis loop. As shown in the example plot in Figure 3.10a, these EOSs gave lower differential amounts of desorbed gas than the corresponding differential amounts adsorbed. Conversely, EOSs (that is SRK-Peneloux, SRK-EOS & LK-EOS) that gave positive relative deviations for Z-factors of methane (Ekundayo and Rezaee, 2019a) produced negative hysteresis loops and the more positively deviated the Z-factors are, the larger the loop. As shown in the example plot in Figure 3.10b, each of these EOSs gave differential amounts of gas desorbed greater, for most of the pressure steps, than the corresponding differential amounts adsorbed.
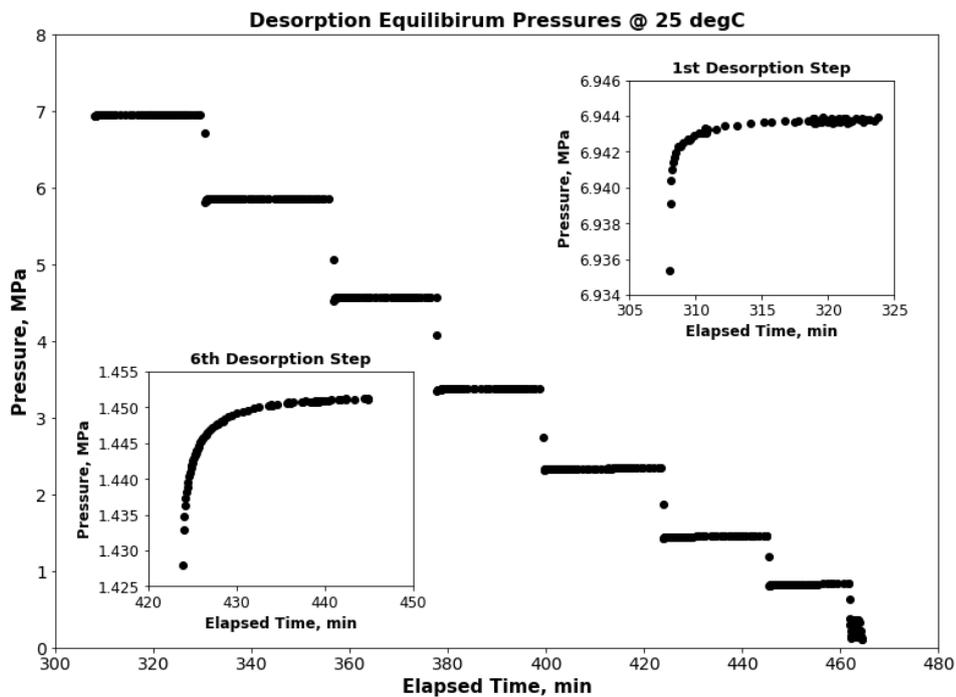
Figure 3.9: Equilibrium pressures for all desorption steps at 25°C
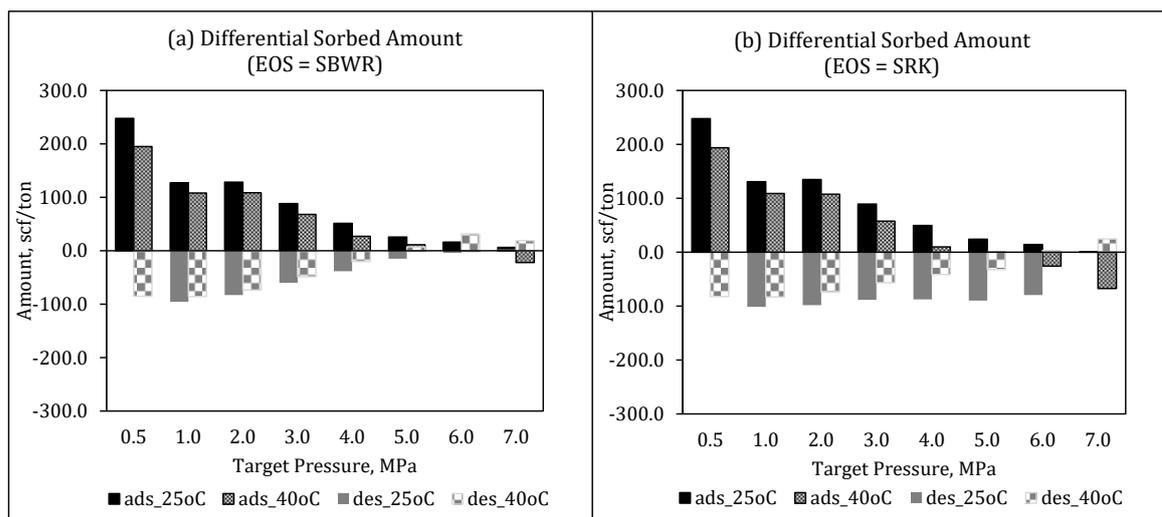
Figure 3.10: Comparing differential ad/desorbed amounts Vs. EOS

3.5.4 Langmuir Parameters – Adsorption Isotherms

Table 3.3 shows the model parameters obtained by fitting the three-parameter Langmuir model to each of the adsorption isotherms. The results showed that the model achieved over 99% match with each of the isotherms as indicated by the R^2 values. For each EOS, it was also observed that Langmuir volume and adsorbed phase density are lower, while Langmuir pressure is higher, at 40°C than the corresponding values at 25°C due to the reducing effect of temperature on gas adsorption (Gasparik et al., 2012, Tang et al., 2015, Yang et al., 2018a, Zhang et al., 2015b, Zou et al., 2017). The lower adsorbed phase density at 40°C is an indication of the temperature-dependence of this parameter which is often assumed to constant and temperature-independent (Zhang and Liu, 2016, Harpalani et al., 2006, Zhang et al., 2015b, Gasparik et al., 2012). As shown in Figure 3.11, SBWR-EOS gave the closest values of Langmuir volume and pressure compared to NIST-refprop at both temperatures. Conversely, PR-EOS and PR-Peneloux gave the largest deviations for these parameters relative to the reference values. These observations agree with the deviations of Z-factors of methane obtained from these EOSs. Lastly, the adsorbed phase density obtained from SBWR-EOS at 25°C is large and as such, the ratio of the bulk gas density at each pressure to adsorbed phase density is negligibly small so that excess adsorption approximates absolute adsorption for this EOS at this temperature.

Table 3.3: Langmuir Parameters for Different Equations of State

(Adsorption Isotherms only)

Equation of State	Langmuir Parameters	25.0 ºC	40.0 ºC
NIST-refprop	VL, Scf/ton	772.9	705.8
	PL, MPa	1.02	1.26
	ρ_{ads}, Kg/m^3	689.9	92.1
	R^2	0.9985	0.9953
PR	VL, Scf/ton	943.3	860.9
	PL, MPa	1.34	1.63
	ρ_{ads}, Kg/m^3	590.9	103.7
	R^2	0.9969	0.9918
PR-Peneloux	VL, Scf/ton	964.6	880.1
	PL, MPa	1.38	1.68
	ρ_{ads}, Kg/m^3	578.8	104.6
	R^2	0.9966	0.9915
SRK	VL, Scf/ton	806.6	740.0
	PL, MPa	1.08	1.34
	ρ_{ads}, Kg/m^3	183.8	69.4
	R^2	0.9978	0.9946
SRK-Peneloux	VL, Scf/ton	815.0	748.2
	PL, MPa	1.10	1.35
	ρ_{ads}, Kg/m^3	165.4	66.9
	R^2	0.9977	0.9947
SBWR	VL, Scf/ton	800.0	699.7
	PL, MPa	1.09	1.23
	ρ_{ads}, Kg/m^3	1.30E+09	116.6
	R^2	0.9983	0.9957
Lee-Kesler	VL, Scf/ton	836.8	768.4
	PL, MPa	1.13	1.39
	ρ_{ads}, Kg/m^3	742.9	98.2
	R^2	0.9973	0.9911
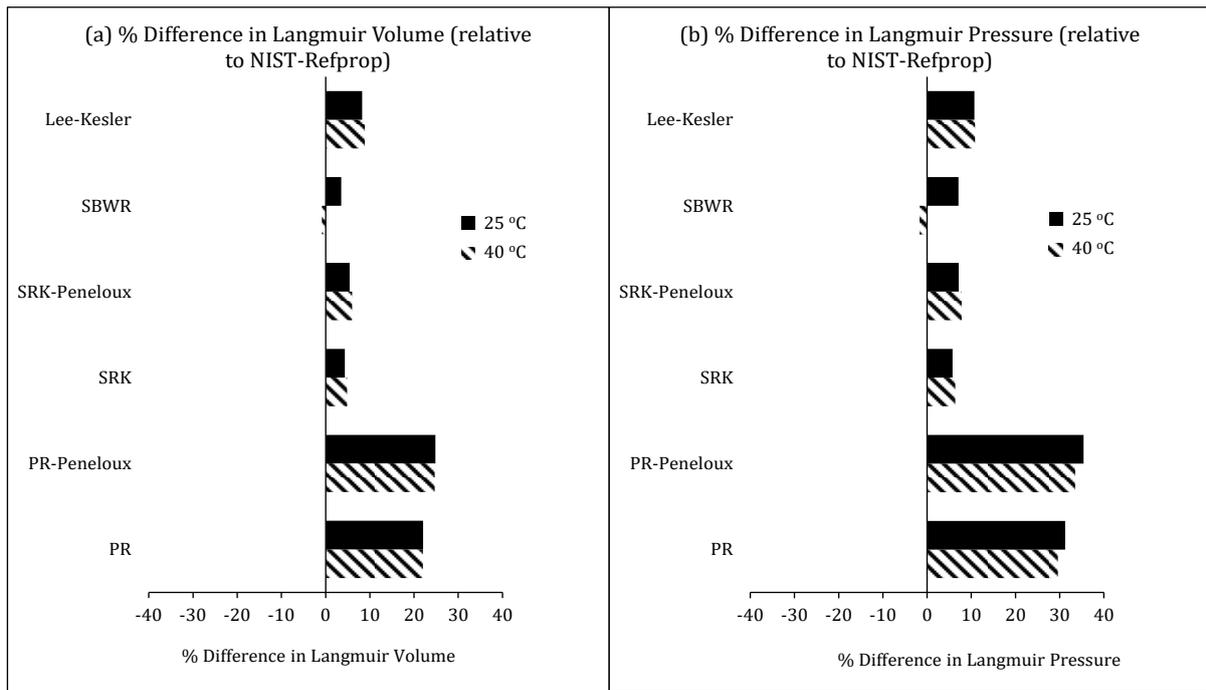
Figure 3.11: Percentage difference in Langmuir parameters by EOS with respect to NIST-Refprop®

3.5.5 Original Gas in-Place (OGIP)

Figure 3.12 shows the calculated initial Z-factor, initial gas FVF, OGIP, and relative differences in the calculated OGIP for each EOS. Similar to previous observations on variations in Z-factors of methane, PR-Peneloux, PR, and SBWR EOSs gave lower values of Z-factor of methane compared to the Setzmann & Wagner's (shown as refprop in Figure 3.12) while SRK-Peneloux, SRK and Lee-Kesler EOSs gave higher values. The corresponding values of initial gas FVF are shown in Figure 3.12b *(grey bars)*. Given the direct relationship between Z-factor and gas FVF (as shown in equation 3.13), the calculated initial gas FVF followed the same trend as the Z-factors. The black bars in Figure 3.12b represent the constant value of gas FVF for case 2. This constant value is the reference gas FVF obtained from Setzmann & Wagner's EOS. As shown in Figure 3.12c, the calculated OGIPs for cases 1 & 2 show a minimal difference. This implies that gas FVF (by implication Z-factor) has a negligible effect on OGIP for this coal. Therefore, it can be concluded that the observed variation in calculated OGIPs (shown in Figure 3.12d) is primarily caused by the variations in Langmuir parameters obtained with the different EOSs. Thus, SBWR-EOS gave the lowest deviation in OGIP relative to refprop while PR-Peneloux EOS gave the largest deviation. As shown in Figure 3.13, the deviations in OGIP correlate directly with deviations of Langmuir volume (or pressure) relative to the refprop. The proportion of OGIP that is adsorbed is shown in Figure 3.14. It is not

unsurprising that the adsorbed gas accounted for over 90% of gas in-place (for each EOS) given the initial porosity and initial water saturation in the cleats (Table 3.2). This is also supported by the sample's pore-size distribution which contains less than 10% of macropores that could hold free gas.
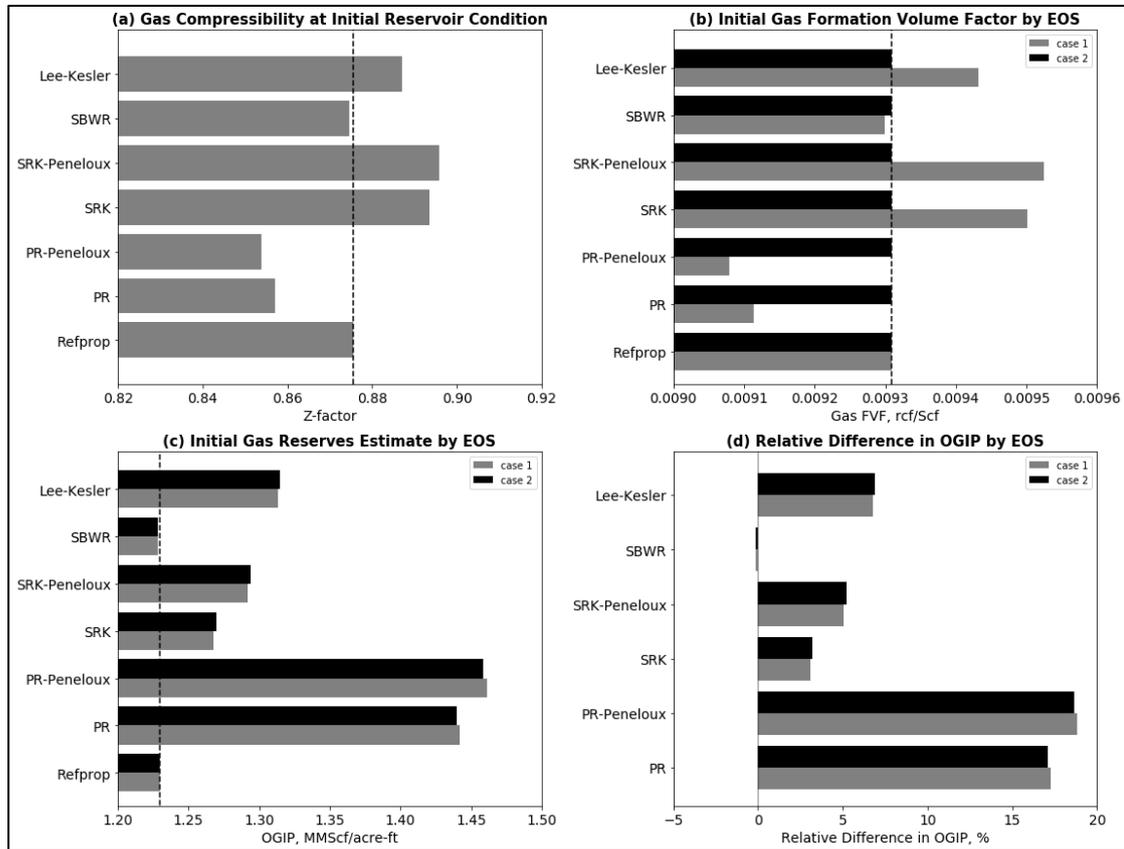
Figure 3.12: Effects of Equation of state on OGIP (a) EOS Vs Z-factor at initial reservoir conditions (b) EOS Vs Initial FVF (c) EOS Vs OGIP (d) Relative difference in calculated OGIPs
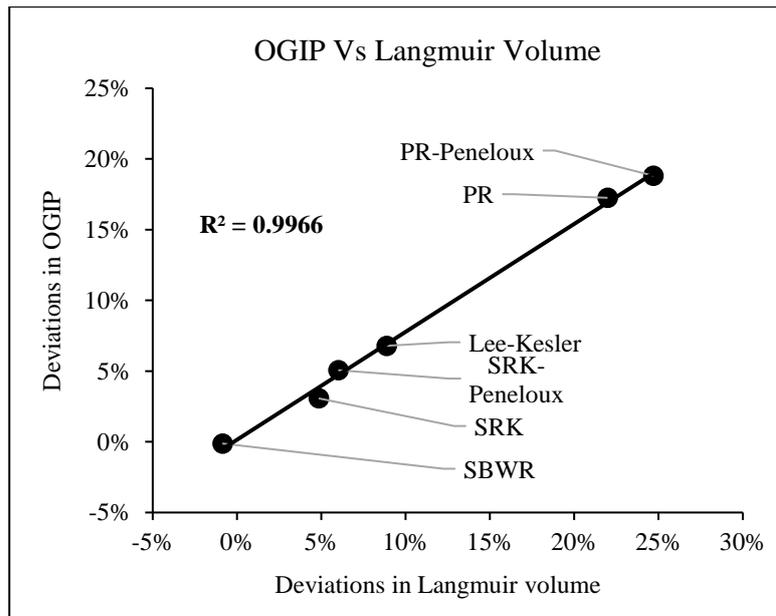
Figure 3.13: Relationship between calculated Gas Reserves and Langmuir Volume
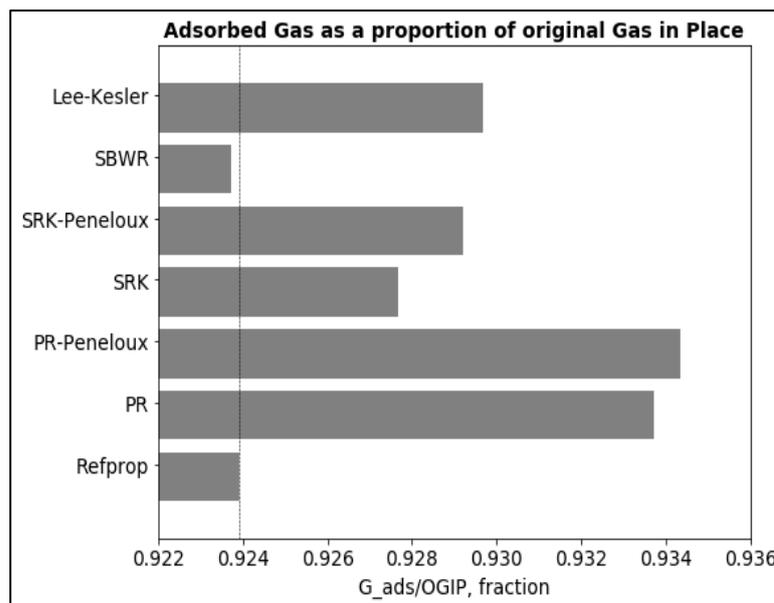
Figure 3.14: Adsorbed gas as a ratio of the original gas in-place

3.6 Conclusions

This chapter presents the effects of equations of state on the results of high-pressure volumetric measurements of methane adsorption and desorption isotherms on a coal sample. The results showed that all the equations of state tested gave varied deviations in the measured isotherms, calculated Langmuir parameters, observed type and degree of sorption hysteresis, and original gas in-place because of the variations in the calculated Z-factors of both helium and methane relative to NIST-refprop. It can be concluded that:

1. Gas compressibility factors have significant effects on high-pressure adsorption and desorption isotherms of methane on coal.

2. Langmuir parameters also varied significantly with the choice of EOS with the SBWR-EOS having the closest values Langmuir volumes and pressures to NIST-refprop at both test temperatures.

3. For each EOS, Langmuir volume and adsorbed phase density are lower for 40°C than the corresponding values at 25°C because of the negative effect of temperature on adsorption.

4. High-pressure methane-coal adsorption-desorption hysteresis is not a unique phenomenon; its existence, degree, and type depend on the applied EOS.

5. For both test temperatures, negligible hysteresis was observed for the reference EOS while a relationship was observed between the deviations of methane Z-factor for each EOS (relative to Setzmann & Wagner's) and the type of sorption hysteresis observed. Negatively deviating EOSs produced positive sorption hysteresis while positively deviating ones gave negative sorption hysteresis for the same dataset.

6. Calculated OGIP is predominantly in adsorbed phase and as such, varies with Langmuir volume.

In summary, it has been demonstrated that, significant uncertainties may be incurred in estimated gas contents and gas reserves of unconventional gas reservoirs due to the choice of EOS for computing the gas compressibility factors needed for experimental data analysis.

Chapter 4

Experimental Investigation and Mathematical Modelling of Shale Gas Adsorption and Desorption Hysteresis

4.1 Introduction

High-pressure adsorption of supercritical methane is often used to determine the gas contents of shale reservoirs at in situ conditions. This is because gas adsorption in the internal surface areas of the rock matrix is the primary storage mechanism in such reservoirs (King, 1993, Curtis, 2002, Bell and Rakop, 1986). The amount of gas adsorbed by a rock is affected by controllable factors such as pressure, temperature, and moisture contents (Bell and Rakop, 1986) as well as the rock's organic and inorganic matter compositions. The relationship between the amount of gas adsorbed, at a constant temperature, and pressure is known as adsorption isotherm and can be measured experimentally using various techniques such as volumetric, spectroscopic, and gravimetric among others. The measured adsorption is referred to as the excess adsorption which implies that the difference in the amount of gas in the adsorbent at a given pressure and temperature and the amount that would otherwise be present as bulk phase if all the adsorbent's pore volume were accessible under the same conditions (Myers and Monson, 2014). A typical workflow in determining the gas contents of shale resources involves the conversion of excess to absolute adsorption followed by a mathematical modelling of the resultant absolute adsorption isotherm, typically using the Langmuir model (Langmuir, 1918). Detailed discussions of the different types of adsorptions and how to convert from one to the other have been extensively discussed in the literature (Myers and Monson, 2002, Brandani et al., 2016, Myers and Monson, 2014). However, it is important to reiterate that the density of the adsorbed phase (ρ_{ads}) controls the shape and size of the resultant absolute adsorption and consequently, the model parameters associated with the isotherm. Currently, there is no practical mechanism to measure ρ_{ads}. Thus, different approaches have been devised to estimate this parameter, including modifications to original adsorption models to handle supercritical conditions. Despite these efforts, ρ_{ads} remains an elusive parameter to estimate accurately.

The workflow described above is an indirect method used extensively for estimating gas contents in shale reservoirs and coal-seams. Several samples might be collected at different depths in a well to capture vertical trends in gas contents and possibly across several wells to

reduce the uncertainties in the estimated gas contents for the shale play. However, considering the associated cost, more often, adsorption experiments are conducted with few samples, fitted to a choice model (usually Langmuir) and the model parameters correlated with experimental parameters like temperature and shale properties such as TOC and clay contents (Liu et al., 2017a, Zou and Rezaee, 2019). Since TOC and clay contents can be tied to wireline logs (Fertl and Chilingar, 1988), these empirical models can be used to study the vertical and areal variations in gas contents. Several empirical models have been reported in the literature for predicting gas contents in different shale Formations across the world. For example, using data from different shale Formations, Zou and Rezaee (2019) developed prediction models for temperature-dependent Langmuir volume and pressure as functions of TOC and total clay contents.

Just as gas adsorption is akin to reserves estimation in shale reservoirs, gas desorption is also paramount to gas transport (and hence, production) in such reservoirs (Wang et al., 2017b, Ekundayo and Rezaee, 2019b). The importance of gas adsorption and desorption processes in modelling flows in shale gas reservoirs has also been re-emphasized by two recent independent review articles (Taghavinejad et al., 2020, Yang and Liu, 2020). However, despite the significant records of gas adsorption studies in shale reservoirs, studies involving desorption of methane from shales at high-pressure and high-temperature conditions remain very scanty. It is generally believed that high-pressure methane adsorption in shale reservoirs is a physical and reversible process (Ozdemir, 2017, Bell and Rakop, 1986, Dutta et al., 2011). Hence, the existence of sorption hysteresis under high-temperature, high-pressure conditions is often doped as an experimental error (Ekundayo and Rezaee, 2019c, Zhang et al., 2015b, Bell and Rakop, 1986, Zhang and Liu, 2016, Battistutta et al., 2010, Weishauptová et al., 2015, Dutta et al., 2011, Jessen et al., 2008, Liu et al., 2017b, Feng et al., 2016, Busch et al., 2003, Ozdemir, 2017, Wang et al., 2017a). However, findings from studies involving methane-coal systems have refuted this argument, suggesting other factors unconnected with the experimental parameters, might be responsible for this phenomenon (Ekundayo and Rezaee, 2019c, Ekundayo et al., 2020, Wang et al., 2014b). Excellent summaries of the key factors researchers have identified as the primary causes of sorption hysteresis in supercritical methane-coal systems at high pressures are available in (Ekundayo and Rezaee, 2019c, Ekundayo et al., 2020, Wang et al., 2014b).

In addition to the lack of enough studies on high-pressure methane desorption in shale Formations, there is no record of an empirical model to estimate the Langmuir parameters for

desorption. Also, the reported cases of high-pressure desorption of methane in shales and coals were either not modelled mathematically, or described using the Langmuir model with or without modifications. For example, while Zhang and Liu (2016) modelled desorption isotherms of methane in coals using a multiplied the Langmuir model by a factor referred to as the hysteretic factor to define the fraction of the gas-adsorbed sites available for desorption, Wei et al. (2017a) added a constant referred to as the "residual adsorption capacity" to Langmuir model to achieve the same objective for methane in shale. This same approach was adopted by He et al. (2019) However, it is noteworthy that neither of these proposed modifications to the Langmuir model (for desorption) has a scientific and theoretical backing, and thus, could be subjective.

To avoid the subjectivity associated with these modifications, this study applies the Langmuir model without modifications (similar to (Bell and Rakop, 1986)). Besides the elimination of subjectivity, the use of the unmodified Langmuir model allows for an unbiased comparison of the model parameters for desorption isotherms with the corresponding values from adsorption isotherms. Furthermore, this study develops the first ever mathematical models to predict the Langmuir parameters for desorption of methane in shales as functions of both temperature and rock properties. Moreover, while the predictive models developed for both adsorption and desorption in this study are based on Goldwyer shales, the approach used here can be replicated in other shale Formations especially those with clay (illite/mica) contents.

4.2 Sample and Methods

4.2.1   Sample

The properties of the samples used in this chapter have been discussed in detail in the Chapter 2 of this thesis.

4.2.2   Measurement and Modelling of Methane Sorption Isotherms & Hysteresis

Methane adsorption and desorption isotherms were measured at 25°C, 40°C, 60°C and 80°C for each sample using a high-pressure volumetric analyser (HPVA-II 200). The equipment uses the volumetric technique to measure the sorption isotherms of a gas on powdered rock samples and helium expansion for void volume measurements. Details of the measurement procedures and volumetric calculations have been extensively discussed in the literature (Ekundayo and Rezaee, 2019a, Ekundayo and Rezaee, 2019c, Zhang et al., 2015b, Zou et al., 2017). Prior to helium calibration, an aliquot of each sample was degassed in a furnace under vacuum at 110°C

for at least 16 hours to ensure all moisture contents and light hydrocarbons are completely removed. The measured excess isotherms (V_{exc}) were converted to absolute isotherms (V_{abs}) using equation 4.1 below:

$$V_{abs} = V_{exc}\bigg/\left(1 - \frac{\rho_{bulk}}{\rho_{ads}}\right)$$

<div align="right">4.1</div>

The bulk gas density (ρ_{bulk}) was obtained from Soave's modified Benedict-Webb-Rubin's equation of state (SBWR-EOS) (Soave, 1999). The resultant absolute isotherms were then represented by the traditional 2-parameter Langmuir model (Langmuir, 1918) as shown in equation 4.2.

$$V_{abs} = \frac{V_L P}{P + P_L}$$

<div align="right">4.2</div>

For each sample, the Langmuir volume, V_L and Langmuir pressure, P_L were determined for both adsorption and desorption isotherms. Equations 4.1 and 4.2 are often combined to a three-parameter Langmuir model for easy calculation of both the Langmuir parameters and adsorbed phase density (ρ_{ads}). However, it has been reported that this approach can be inappropriate within the pressure ranges tested in this study (Ekundayo and Rezaee, 2019b, Zhang et al., 2016) or in a case where the excess adsorption reaches an early maximum (Gasparik et al., 2012). Moreover, the method of linearly fitting plot of excess adsorption – bulk density post-saturation has also been shown to be subjective especially where the post-saturation data points are too few to justify the mathematical fit (Ekundayo and Rezaee, 2019b). On these bases, the modified Dubinin-Radushkevich (DR) (equation 4.3) (Sakurovs et al., 2007, Yang et al., 2018b, Rexer et al., 2013) was employed in this study to fit the measured adsorption data and obtain the value of the adsorbed phase density for each sample at each temperature. The calculated adsorbed phase density was then used in equation 1 to convert both the adsorption and desorption isotherms to absolute isotherms which were then fitted to equation 4.2. This hybrid DR-Langmuir fitting approach combined the superiority of the DR-model in calculating the adsorbed phase density (Rexer et al., 2013) for the range of pressures used in this study with the simplicity of Langmuir model.

$$V_{exc} = V_o * exp\left\{-D * \left(ln\left(\frac{\rho_{ads}}{\rho_{bulk}}\right)\right)^2\right\}\left(1 - \frac{\rho_{bulk}}{\rho_{ads}}\right)$$

<div align="right">4.3</div>

V_o in equation 4.3 is the maximum absolute adsorption while D is a parameter related to pore structure through the characteristic energy of adsorption (E) (Hutson and Yang, 1997) as shown in equation 4.4 below.

$$D = \left(\frac{RT}{E_o\beta}\right)^2 = \left(\frac{RT}{E}\right)^2 \qquad\qquad 4.4$$

Where E_o is the characteristic energy of adsorption for a reference vapour (typically benzene) and β is known as similarity constant (Hutson and Yang, 1997) which indicates the affinity of the adsorbent for the adsorbate (Tang et al., 2017). The characteristic energy of adsorption can be used to discriminate between physical adsorption (physisorption) and chemical adsorption (chemisorption).

Following the calculations of the Langmuir parameters, the size of the observed hysteresis between the adsorption and desorption isotherms was quantified using both the areal hysteresis index (*AHI*) (Zhang and Liu, 2016, Zhu and Selim, 2000) and improved hysteresis index (*IHI*) (Wang et al., 2014b) for each sample at each temperature. Figure 4.1 is an illustration of a typical sorption hysteresis of supercritical methane on shale rocks.
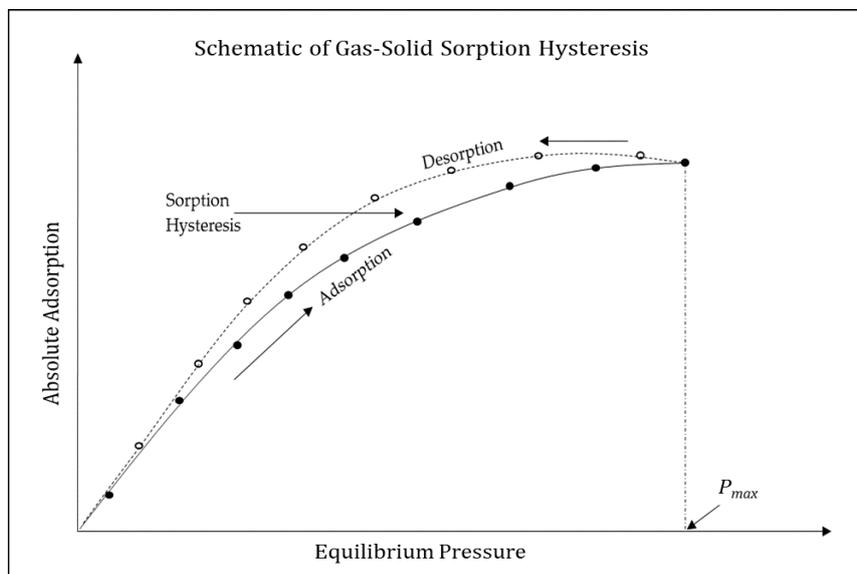
Figure 4.1: Illustration of hysteresis between gas-solid adsorption and desorption isotherms

The area covered by the hysteresis loop (A^{hys}) is given as the difference between the areas bounded by desorption isotherm (A^{des}) and adsorption isotherm (A^{ads}) and can be expressed mathematically as:

$$A^{hys} = A^{des} - A^{ads} = \int_0^{P_{max}} \left(\frac{V_L^{des} P}{P_L^{des} + P} - \frac{V_L^{ads} P}{P_L^{ads} + P} \right) dP \qquad 4.5$$

The difference between *AHI* and *IHI* lies in the definition of the base area to which the hysteresis area is compared. *AHI* is the ratio of the hysteresis area to the area bounded to the pressure axis by the adsorption curve.

$$AHI = \frac{A^{hys}}{A^{ads}} = \frac{V_L^{des} \left(P_{max} - P_L^{des} \times \ln \left(\frac{P_L^{des} + P_{max}}{P_L^{des}} \right) \right)}{V_L^{ads} \left(P_{max} - P_L^{ads} \times \ln \left(\frac{P_L^{ads} + P_{max}}{P_L^{ads}} \right) \right)} - 1 \qquad 4.6$$

IHI on the other hand, is the ratio of the hysteresis area to the area bounded to the adsorbed volume axis by the adsorption isotherm. The latter area is equivalent to the fully irreversible hysteresis area (A^{irr}).

$$IHI = \frac{A^{hys}}{A^{irr}} = \frac{A^{hys}}{V_{max} * P_{max} - A^{ads}} \qquad 4.7$$

4.3 Results and Discussion

4.3.1   High-Pressure Methane Sorption Isotherms

Figure 4.2 shows the measured methane adsorption isotherms for all the eight samples described in the preceding sections. For each sample, the excess adsorption followed the expected decreasing trend with temperature. The amount adsorbed increased rapidly with pressure until about 5MPa, which is in the neighbourhood of the critical pressure of methane, beyond which the rate of increase was significantly lower and for some samples, adsorbed amounts decreased beyond this pressure point. This behaviour is a typical characteristic of excess adsorption of supercritical fluids on solids (Do and Do, 2005).

At the point of inflection, the rates of change of the adsorbed and bulk phase densities with pressure are the same. This phase equilibrium (between the adsorbed and free fluids) occurred, for most of our samples, at the pressure in the neighbourhood of the critical pressure of methane (4.6MPa). Although lower than most of the values published for pressures at maximum excess adsorption of methane on shale, similar values exist in literature for a few samples. For example, the "*Geverik*" shale sample in Gasparik et al. (2012) showed significant maximum excess adsorption at about 6MPa while samples *X2-4* and *X3-1* in Zhou et al. (2018) showed maximum excess adsorptions between 5MPa – 10MPa. While no explanation was offered for

these observations in the latter, the *Geverik*'s case was attributed to the high proportion of organic microporosity due to the sample's over-maturity (Gasparik et al., 2012). On the contrary, our samples are predominantly mid to late matured marine shales and are characterised by larger proportions of mesopores in the inorganic components. Thus, thermal maturity alone cannot explain the early pore saturation observed in this study. It is expected that the high clay (illite) contents in these samples will counteract the high methane adsorbing capacity of their organic matters by reducing the surface areas available to methane adsorption in the organic pores and consequently, leading to earlier pore saturation than expected.
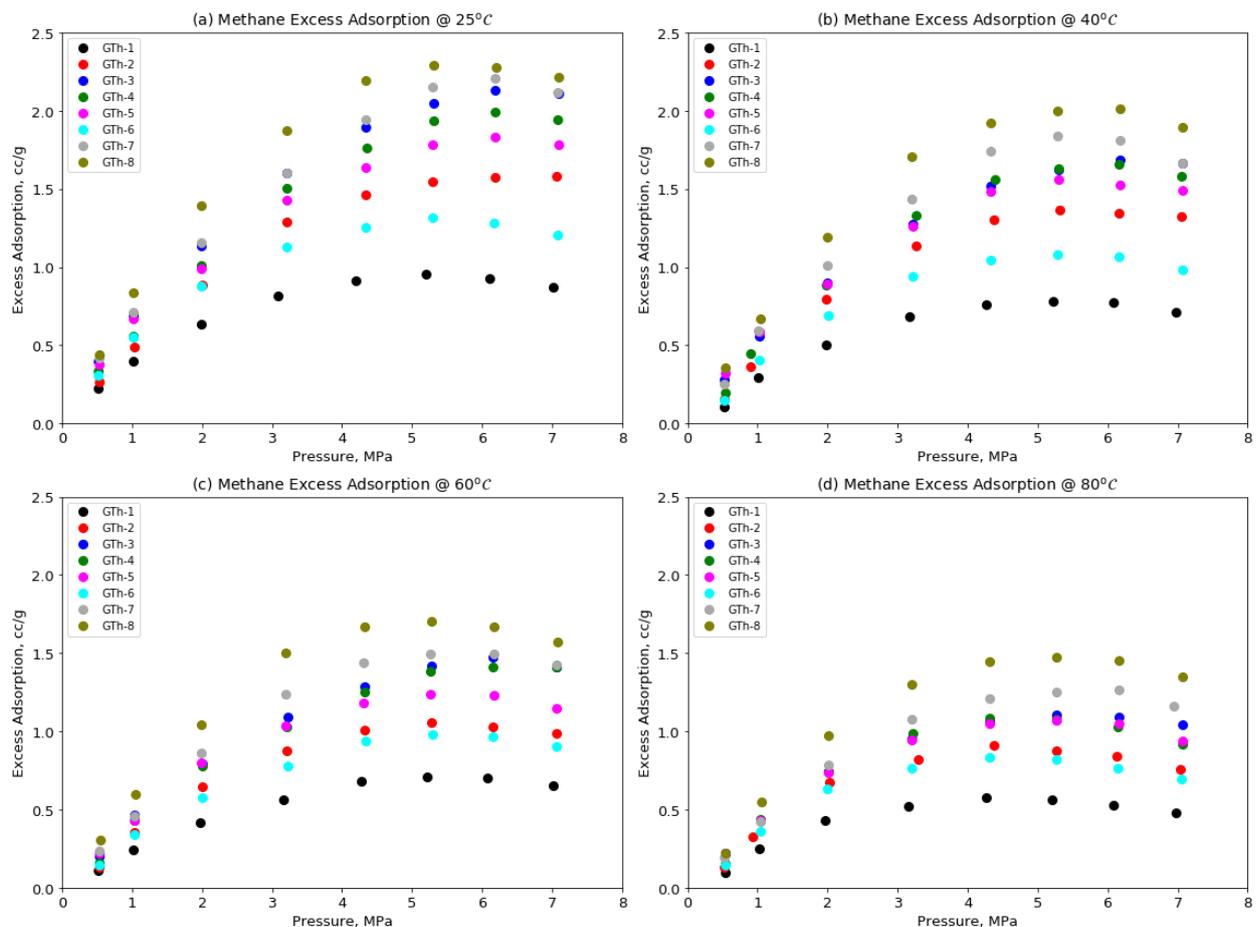
Figure 4.2: Excess adsorption of methane on shale samples at different temperatures

It follows from the above discussion that the methane sorption processes in our samples are controlled by a combined effect of their organic and inorganic contents. To capture this interplay, the parameter COC, discussed in Chapter 2 of this thesis, was used to better account for the effect of clay contents on adsorption and desorption model parameters. Table 4.1 summarises the relationship between the maximum excess adsorption and each of TOC content, total clay content, and the clay-to-organic-carbon (COC) ratio. These results show that

maximum excess adsorption has a strong positive linear correlation with TOC content but a weak negative linear correlation with total clay contents. The opposing correlations of maximum excess adsorption with TOC and total clay contents support our explanation for the observed low excess adsorptions and early pore saturation. At each temperature, maximum excess adsorption shows positive correlations with COC with values of the coefficient of determination (R^2 values) greater than 70%; lower than those of correlations with TOC because of the influence of clay contents. The decreasing slope and (vertical) intercept for each rock property is a reflection of the negative effect of temperature of adsorption.

Table 4.1: Relationships between maximum excess adsorption and rock properties

T, ºC	Maximum V_{exc} vs TOC Content		Maximum V_{exc} vs Total Clay		Maximum V_{exc} vs COC	
	Equation	R^2	*Equation*	R^2	*Equation*	R^2
25	$0.3173 \times$ TOC + 1.0304	0.9517	2.4921 - 0.0108 $\times$ Clay	0.1300	2.0913 - 0.0047 $\times$ COC	0.7745
40	$0.2731 \times$ TOC + 0.8463	0.9482	2.1997 - 0.0107 $\times$ Clay	0.1733	1.7592 - 0.0040 $\times$ COC	0.7692
60	$0.2191 \times$ TOC + 0.7347	0.9443	1.8074 - 0.0084 $\times$ Clay	0.1646	1.4597 - 0.0031 $\times$ COC	0.7124
80	$0.1800 \times$ TOC + 0.6107	0.9126	1.6061 - 0.0087 $\times$ Clay	0.2499	1.2084 - 0.0026 $\times$ COC	0.7077

4.3.2 Desorption Isotherms and Sorption Hysteresis

In addition to the adsorption isotherms, desorption isotherms were measured at each temperature for each of the samples to enable us to examine the existence and size of sorption hysteresis and its relationships with rock properties. As shown in Figure 4.3, significant hysteresis was observed between the adsorption and desorption isotherms for all the samples at all test temperatures. We have previously reported that the observed hysteresis was primarily due to the choice of equation of state (EOS) used to calculate the gas compressibility factors for experimental data analysis (Ekundayo and Rezaee, 2019b, Ekundayo and Rezaee, 2019c).

4.3.3 Isotherm Modelling – Model Parameters & Relationships with Rock Properties

As previously stated, the three-parameter Langmuir model was found to be inappropriate for isotherms exhibiting early excess adsorption maxima. Thus, the DR-model was used to parameterise the excess adsorption isotherms in this study. The value of ρ_{ads} obtained by fitting the modified DR-model to each adsorption isotherm was used to convert both excess adsorption and (the corresponding) desorption isotherms to absolute sorption isotherms. The results of the modified DR-model fit to the adsorption isotherms are summarised in Table 4.2. The maximum absolute adsorption (V_o) decreases with temperature in line with the expected negative effect of temperature on adsorption. However, contrary to the traditional practice of neglecting the temperature-dependence of the parameter D in the DR-model, the results here show that the

values of D show positive, albeit weak to strong, correlations with temperature. This is also obvious from equation 4.4, which expresses the parameter D as a function of temperature. The characteristic energy of adsorption, E (not shown in the Table) calculated from these results (using equation 4.4) ranged from 5.7 – 7.2 kJ/mol indicating the adsorption type is physisorption (Amrhar et al., 2015). Adsorbed phase densities show mild to strong negative correlations with temperature for all samples except GTh-1 and GTh-6. Lastly, while no appreciable correlation with TOC content, total clay content or COC could be established for parameter D, the characteristic energy (E) of adsorption and adsorbed phase density, the maximum absolute adsorption (V_o) showed strong positive correlations with TOC content and COC but relatively no correlation with total clay content as summarised in Table 4.3.
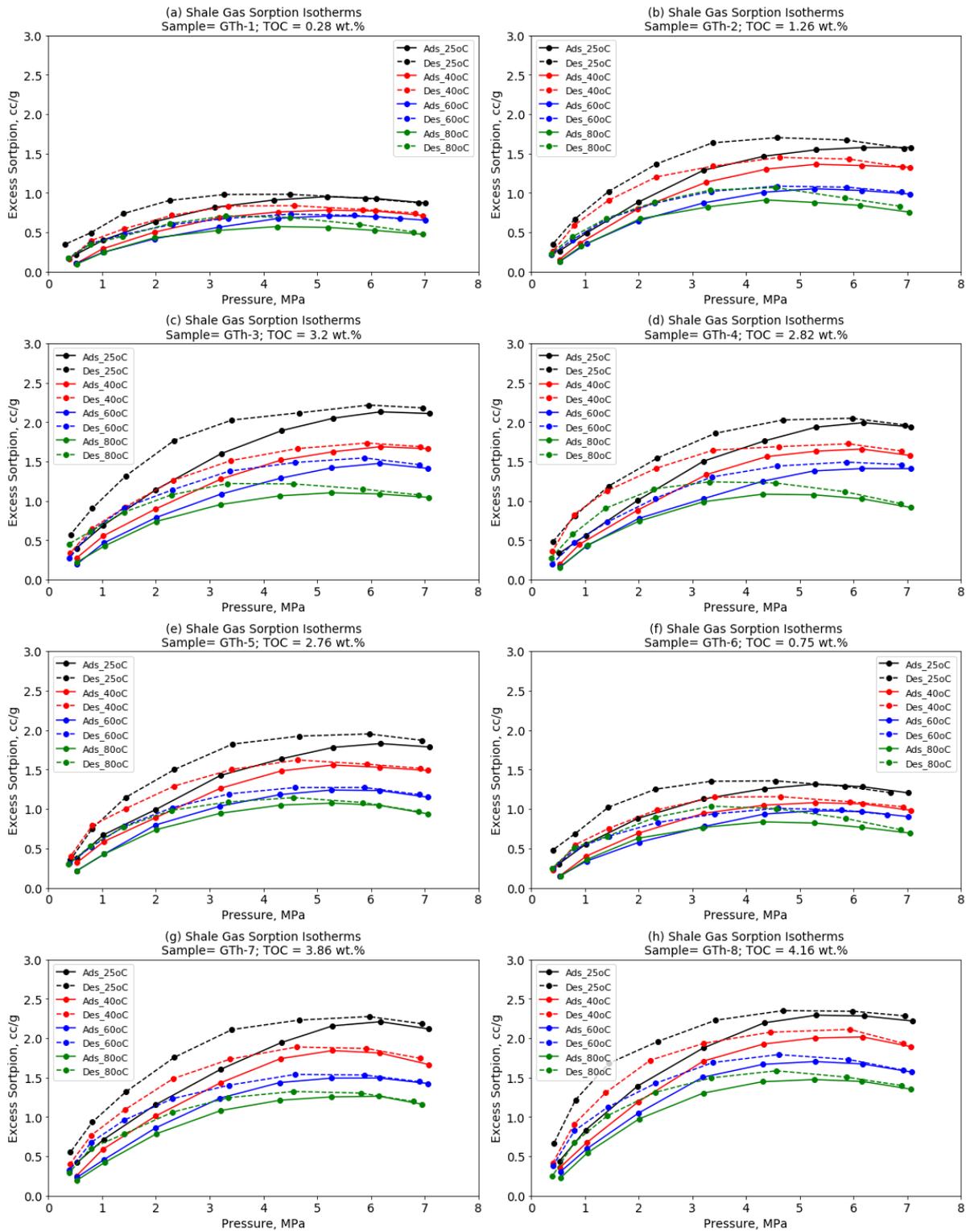
Figure 4.3: Shale gas adsorption and desorption isotherms and their associated hysteresis

Table 4.2: DR's model parameters at different temperatures

Sample ID	Temp. = 25°C			Temp. = 40°C			Temp. = 60°C			Temp. = 80°C		
	V_o, cc/g	D (-)	ρ_{ads}, Kg/m³	V_o, cc/g	D (-)	ρ_{ads}, Kg/m³	V_o, cc/g	D (-)	ρ_{ads}, Kg/m³	V_o, cc/g	D (-)	ρ_{ads}, Kg/m³
GTH-1	1.65	0.15	136.90	1.49	0.20	106.67	1.31	0.19	112.61	1.11	0.21	75.95
GTH-2	2.89	0.17	164.07	2.53	0.18	133.60	2.01	0.21	105.04	1.68	0.19	82.68
GTH-3	3.73	0.13	240.54	3.00	0.15	193.42	2.64	0.16	158.72	2.00	0.17	106.96
GTH-4	3.60	0.16	188.07	3.04	0.18	142.58	2.62	0.17	160.23	2.15	0.23	78.24
GTH-5	3.12	0.12	230.34	2.73	0.15	152.24	2.30	0.19	110.26	1.99	0.19	90.40
GTH-6	2.25	0.15	139.85	2.06	0.21	107.99	1.80	0.19	114.19	1.62	0.22	76.62
GTH-7	3.84	0.14	224.72	3.44	0.21	119.64	2.87	0.21	110.45	2.42	0.21	94.65
GTH-8	4.08	0.16	157.09	3.76	0.19	122.57	3.26	0.21	100.62	2.86	0.21	89.97

Table 4.3: Relationships between DR's maximum absolute adsorption (V_o) and sample properties

T, °C	V_o vs TOC Content		V_o vs Total Clay		V_o vs COC	
	Equation	R^2	Equation	R^2	Equation	R^2
25	$0.5615 \times TOC + 1.8054$	0.9245	$4.2708 - 0.0172 \times Clay$	0.1029	$3.6872 - 0.0084 \times COC$	0.7637
40	$0.4875 \times TOC + 1.5931$	0.9296	$3.9220 - 0.0178 \times Clay$	0.1471	$3.2146 - 0.0071 \times COC$	0.7278
60	$0.4213 \times TOC + 1.3461$	0.9453	$3.4199 - 0.0163 \times Clay$	0.1683	$2.7349 - 0.0059 \times COC$	0.6944
80	$0.3447 \times TOC + 1.1565$	0.8838	$3.0882 - 0.0169 \times Clay$	0.2534	$2.2939 - 0.0049 \times COC$	0.6546

To take advantage of the greater popularity and commercial software implementations of the traditional Langmuir model, the resultant absolute sorption isotherms were described with the two-parameter Langmuir model represented by Equation 4.2. Figure 4.4 shows the calculated absolute adsorption isotherms (markers) and the corresponding Langmuir model fits (solid lines). The absolute adsorption isotherms at each temperature followed the expected positive trend with TOC contents, with GTh-8 having the highest and GTh-1 having the lowest absolute adsorption at all temperatures. The values of the Langmuir volume and Langmuir pressure, for each sample and for each temperature, are summarised in Table 4.4. The results show that the Langmuir model adequately described the absolute adsorption and desorption isotherms with R^2 values exceeding 98%. Thus, it can be concluded that the Langmuir model, without any modification, can satisfactorily describe desorption isotherms. Due to the hysteresis, the desorption isotherms resulted in lower Langmuir volumes and pressures than the corresponding values obtained with the adsorption counterparts.
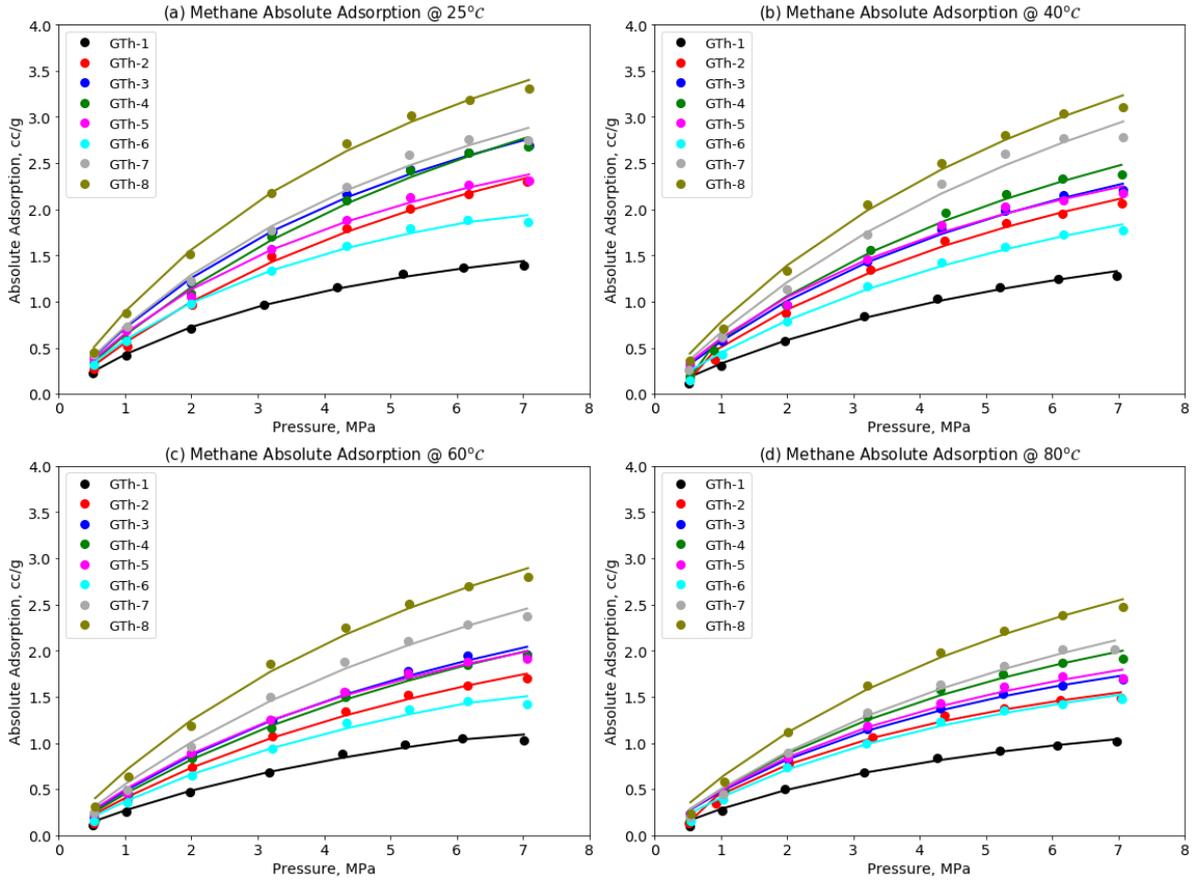
Figure 4.4: Absolute adsorption isotherms of methane on shale samples (markers represent absolute adsorption while lines represent corresponding model fitting)

Table 4.4: Langmuir model parameters for all samples at different temperatures

| Sample ID | Temperature = 25ºC | | | | | | Temperature = 40ºC | | | | | |
| | Adsorption | | | Desorption | | | Adsorption | | | Desorption | | |
	V_L, cc/g	P_L, MPa	R^2	V_L, cc/g	P_L, MPa	R^2	V_L, cc/g	P_L, MPa	R^2	V_L, cc/g	P_L, MPa	R^2
GTH-1	2.37	4.54	0.9967	1.71	1.58	0.9915	2.73	7.36	0.9931	1.92	3.02	0.9957
GTH-2	5.00	8.02	0.9969	3.34	2.86	0.9922	6.79	10.17	0.9954	4.19	3.47	0.9946
GTH-3	5.22	6.31	0.9977	3.74	2.37	0.9984	4.53	7.00	0.9971	3.41	3.45	0.9986
GTH-4	6.23	8.79	0.9952	3.96	3.04	0.9977	5.30	7.99	0.9932	3.38	2.58	0.9964
GTH-5	4.18	5.37	0.9958	3.47	2.72	0.9927	4.11	5.84	0.9938	3.01	2.46	0.9957
GTH-6	3.22	4.52	0.9959	2.37	1.66	0.9948	3.80	7.55	0.9930	2.68	3.15	0.9951
GTH-7	5.59	6.66	0.9931	3.96	2.53	0.9963	6.83	9.30	0.9887	4.59	3.94	0.9984
GTH-8	6.31	6.07	0.9970	4.41	2.24	0.9969	6.77	7.73	0.9942	4.72	3.27	0.9969
Sample ID	Temperature = 60ºC						Temp = 80ºC					
	Adsorption			Desorption			Adsorption			Desorption		
	V_L, cc/g	P_L, MPa	R^2	V_L, cc/g	P_L, MPa	R^2	V_L, cc/g	P_L, MPa	R^2	V_L, cc/g	P_L, MPa	R^2
GTH-1	2.36	7.73	0.9909	1.50	2.64	0.9969	1.88	5.63	0.9920	1.50	2.38	0.9814
GTH-2	3.90	8.65	0.9929	2.72	3.94	0.9991	2.63	4.89	0.9928	2.37	2.87	0.9881
GTH-3	4.39	8.11	0.9944	2.96	3.02	0.9960	3.09	5.55	0.9968	2.19	1.76	0.9920
GTH-4	4.61	9.24	0.9950	3.45	4.71	0.9961	4.01	7.10	0.9901	2.76	2.45	0.9929
GTH-5	3.94	6.93	0.9941	2.98	3.53	0.9987	3.24	5.69	0.9924	2.45	2.61	0.9974
GTH-6	3.28	7.95	0.9907	2.10	2.78	0.9969	2.78	5.79	0.9918	2.23	2.51	0.9805
GTH-7	5.68	9.26	0.9932	3.61	3.55	0.9983	4.60	8.21	0.9923	3.18	3.56	0.9963
GTH-8	6.02	7.65	0.9931	4.27	3.49	0.9971	5.25	7.46	0.9932	3.89	3.61	0.9953

4.3.4 Hysteresis Quantifiers and Relationship with Temperature and Rock Properties

The size of each hysteresis loop, quantified by the indices given by Equations 4.5-4.7, is significantly affected by temperature as shown in Figure 4.5. All three hysteresis quantifying parameters (indices) appear to decrease with temperature with notable deviations at 80°C.
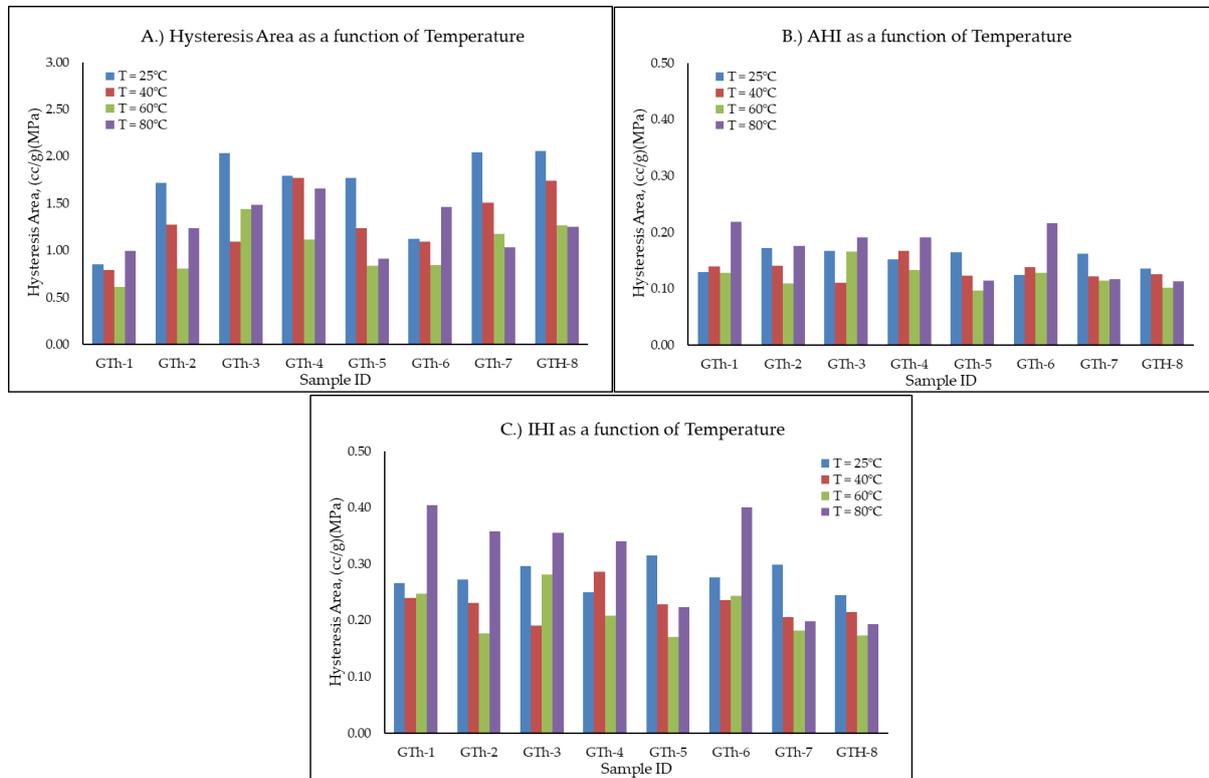
Figure 4.5: Effect of temperature on the size of the hysteresis loop measured by
(A) hysteresis area (B) areal hysteresis index (AHI) and (C) improved hysteresis index (IHI)

This observation is related to the thermodynamics of adsorption and desorption processes which is governed by the Gibb's free energy change (ΔG) given by equation 4.8 below:

$$\Delta G = -RT \ln K \qquad\qquad 4.8$$

Negative ΔG is required for adsorption to be spontaneous and the more negative the value of ΔG, the more favourable the adsorption is (Zhang et al., 2016). Typically, ΔG becomes less negative as temperature increases due to the inverse relationship between *ln K* (where K = adsorption equilibrium constant) and temperature, T (Zhang et al., 2016, Rani and Sud, 2015). Consequently, adsorption is less spontaneous and the degree of freedom (randomness) of methane molecules increases (Rani and Sud, 2015). Thus, desorption is more favoured at higher temperature. For most of the samples, the observed hysteresis at 80°C appeared to be characterized by methane readsorption (Ozdemir, 2004) causing unduly higher areas enclosed by the desorption isotherms. The higher values of the quantifying parameters are in part due to

this phenomenon. Also, the lower values of adsorbed phase density at this temperature resulted in larger values of Langmuir volumes for the desorption process and consequently, larger hysteresis areas and hysteresis indices. Moreover, the choice of equation of state alone may not be a sufficient reason for the extent of the hysteresis. Given their high clay contents, it is difficult to rule out structural changes to the shale samples, caused by the sorption processes (Goodman et al., 2004, Wang et al., 2017a, Yang et al., 2018b), as an explanation for the observed increasing hysteresis size with temperature (from 40°C to 80°C) for sample GTh-3. Adsorption has been reported to induce swelling in rock samples (Zhang and Liu, 2016, Liu et al., 2017b) and the swelling was said to be irreversible by the desorption-induced shrinkage (Cui et al., 2007). Thus, it can be hypothetically stated that the rate of adsorption-induced swelling in this sample increased with temperature. Thus, at higher temperatures, the sample swells more leading to reduced pore throats, increased inaccessibility of pores and consequently, increased gas trapping (Goodman et al., 2004, Wang et al., 2017a).
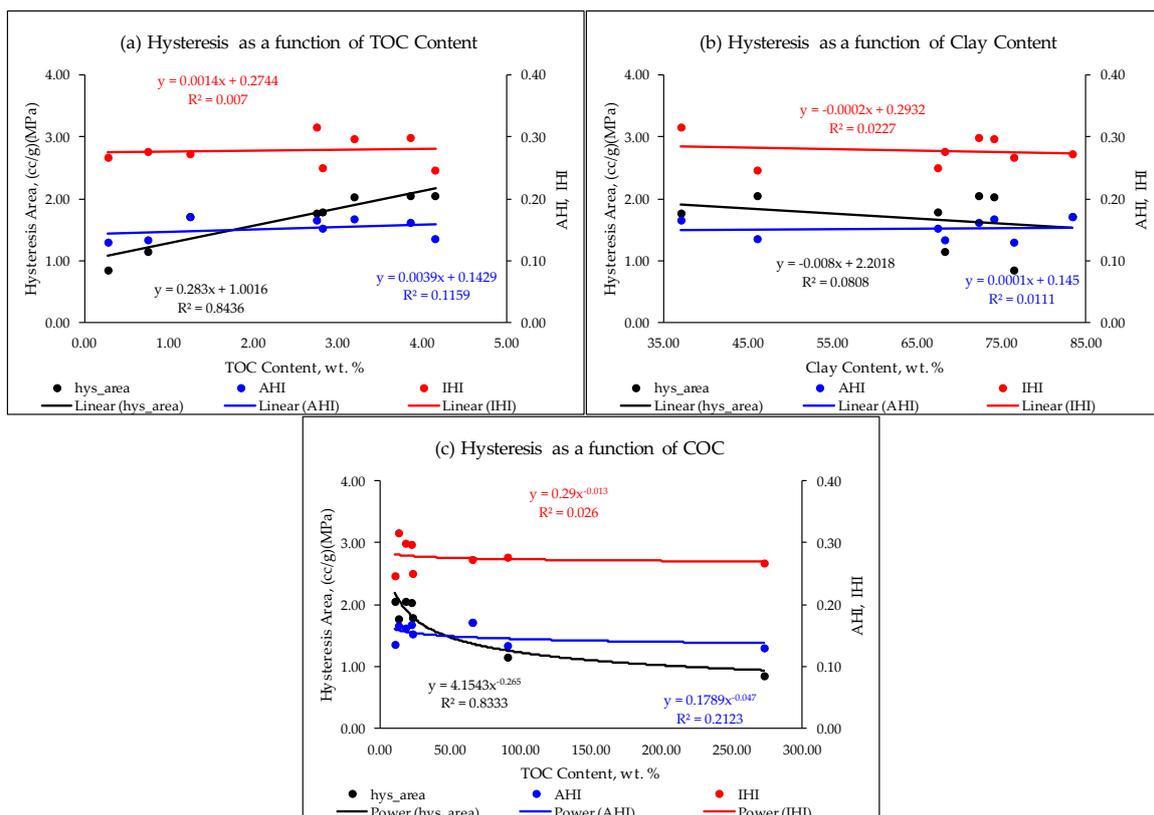
Figure 4.6: Relationship between sorption hysteresis at 25°C and rock properties

A comparison of the hysteresis quantifying parameters as functions of the rock properties is shown in Figure 4.6. It is obvious that both AHI and IHI showed weak to negligible correlations with each of the three rock properties examined. Considering that the amounts adsorbed are different at different temperatures, it is expected that while the size of the hysteretic area may

become smaller with increased temperature, the adsorption area also becomes smaller potentially leading to a higher ratio than expected. Thus, a comparison of the absolute values of areas enclosed by the hysteresis loop at different conditions offered better insights into the relationship between the size of sorption hysteresis and the controlling factors like temperature and rock properties.

4.3.5 Relationships between Langmuir Parameters and Shale Properties

As shown in Figure 4.7, Langmuir volumes for both adsorption and desorption processes showed strong positive correlations with TOC content, indicating that TOC content is the primary factor affecting adsorption and desorption in the Goldwyer Formation shales. A similar relationship between Langmuir volume and TOC content for methane adsorption has been reported in the literature for this Formation (Zou and Rezaee, 2019). The strong relationships between Langmuir volumes and TOC contents can be explained in terms of the stronger affinity of organic matters for methane as a non-polar adsorbate. It is believed that when a non-polar adsorbate (such as methane) binds with the hydrophobic organic matter of the adsorbent, the interfacial area between the non-polar adsorbate and the hydrophilic minerals (such as clay) is reduced (Thompson and Goyne, 2012). This observation is supported by the poor negative correlations found between Langmuir volumes and clay contents as shown in Figure 4.8. However, in order not to downplay the contributions of the clay minerals to methane adsorption and desorption in Goldwyer shales, COC was used as a predictor to capture the effect of clay contents on Langmuir volumes. As shown in Figure 4.9, Langmuir volumes for both adsorption and desorption show significant correlations with COC at all test temperatures. The lower values of the correlation coefficients, compared to of TOC content, are because of the poor correlations of Langmuir volumes with clay contents.

Langmuir pressures showed no appreciable correlation with either TOC, clay contents, or COC. However, positive (albeit weak to intermediate) linear correlations were observed between Langmuir pressures and Langmuir volumes at all temperatures as shown in Figure 4.10.
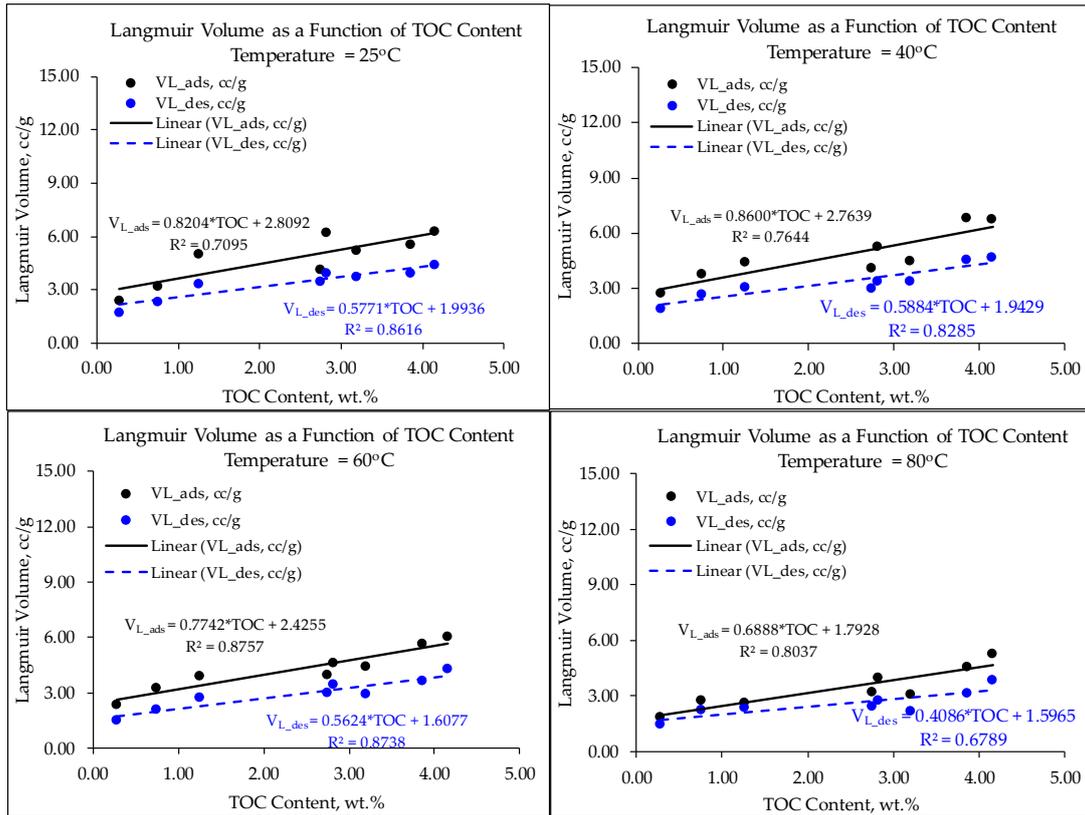
Figure 4.7: Relationship between Langmuir volumes and TOC contents
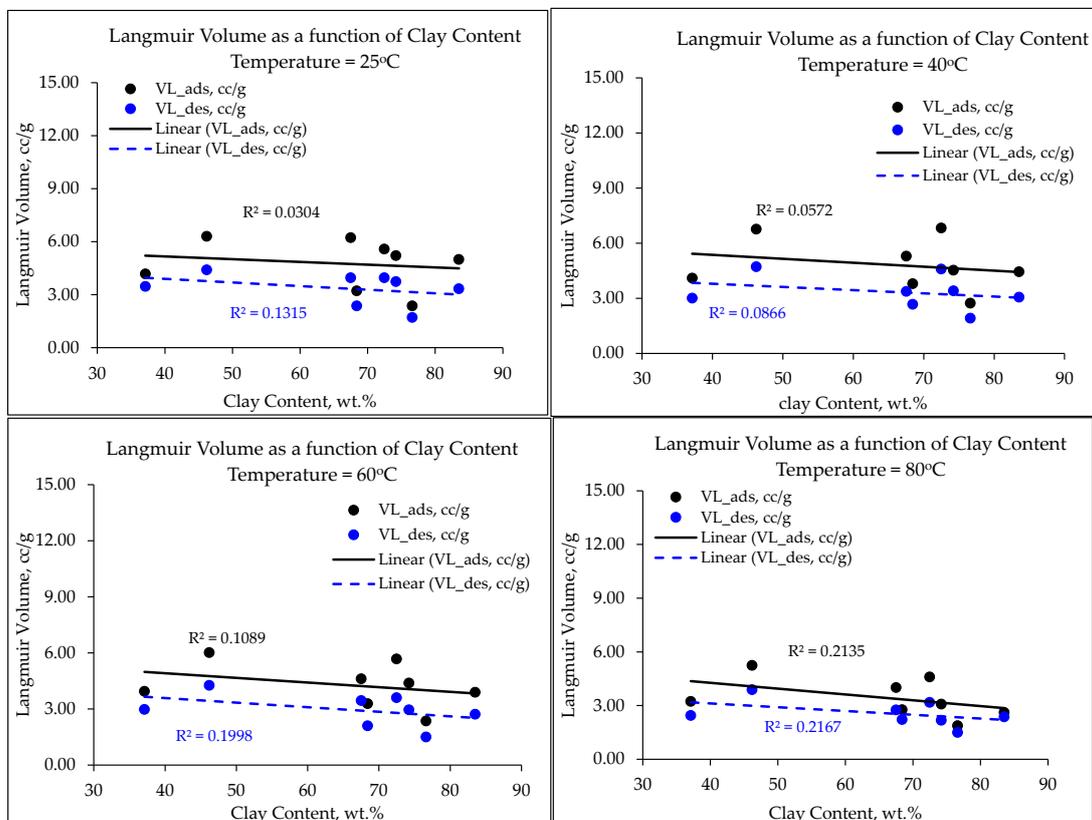
Figure 4.8: Relationship between Langmuir volumes and clay contents
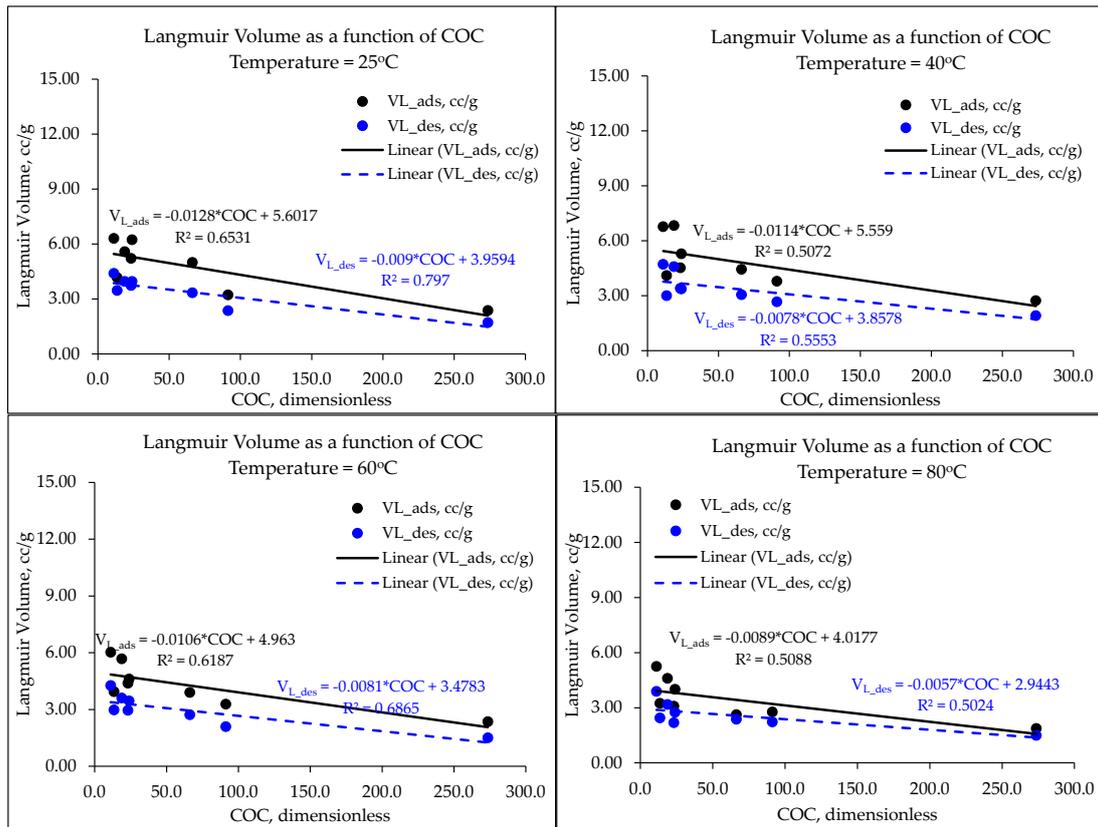
Figure 4.9: Relationship between Langmuir volumes and COC
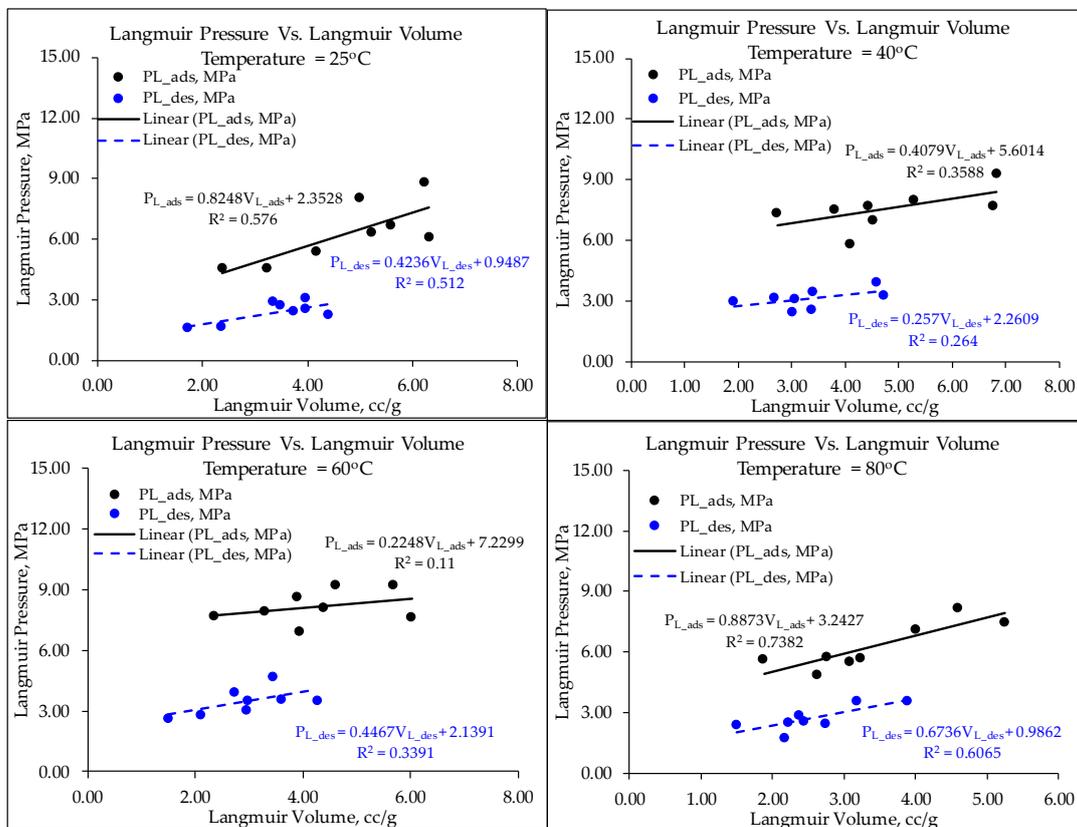
Figure 4.10: Relationship between Langmuir parameters at different temperatures

4.3.6 Prediction Models for Langmuir Parameters

Figure 4.7 shows that the Langmuir volumes for both adsorption and desorption isotherms follow linear relationships with TOC contents at all test temperatures. If the slope and vertical intercept of this linear relationship at a given temperature are *m* and *c* respectively, then the following generalised equation can be written for the relationship between Langmuir volume and TOC content:

$$V_L = m \times TOC + c \qquad\qquad 4.9$$

Another observation from the Figure is that both the slopes and vertical intercepts are functions of temperature. Thus, for temperature T in °C, the temperature-dependent nature of both *m* and *c* can be represented, for each the sorption process, by the following equations:

$$m_{ads}(T) = 0.9240 - 0.0027 \times T \qquad\qquad 4.10a$$

$$m_{des}(T) = 0.6861 - 0.0030 \times T \qquad\qquad 4.10b$$

$$c_{ads}(T) = 3.0199 - 0.0081 \times T \qquad\qquad 4.11a$$

$$c_{des}(T) = 2.2093 - 0.0083 \times T \qquad\qquad 4.11b$$

Combining equations 4.10 and 4.11 with equation 4.9, a single relationship was derived for the temperature-dependence of Langmuir volume as a function of TOC contents for each sorption process as shown in equation 4.12.

$$V_{L\_ads}(TOC, T) = 3.0199 + 0.9240 \times TOC - 0.0027 \times T \times (TOC + 3.00) \qquad 4.12a$$

$$V_{L\_des}(TOC, T) = 2.2093 + 0.6861 \times TOC - 0.0030 \times T \times (TOC + 2.79) \qquad 4.12b$$

Similar equations were also developed for the Langmuir volume as a function of COC as shown in equation 4.13.

$$V_{L\_ads}(COC, T) = 6.5456 + 0.0144 \times COC - 6.7 \times 10^{-5} \times T \times (COC - 438.4) \qquad 4.13a$$

$$V_{L\_des}(COC, T) = 4.5215 + 0.0104 \times COC - 5.2 \times 10^{-5} \times T \times (COC - 358.5) \qquad 4.13b$$

Figures 4.11 and 4.12 compare the actual and calculated Langmuir volumes for adsorption and desorption isotherms respectively using both the TOC-based and the COC-based models. The results showed that both models can adequately reproduce the actual Langmuir volumes with acceptable errors.
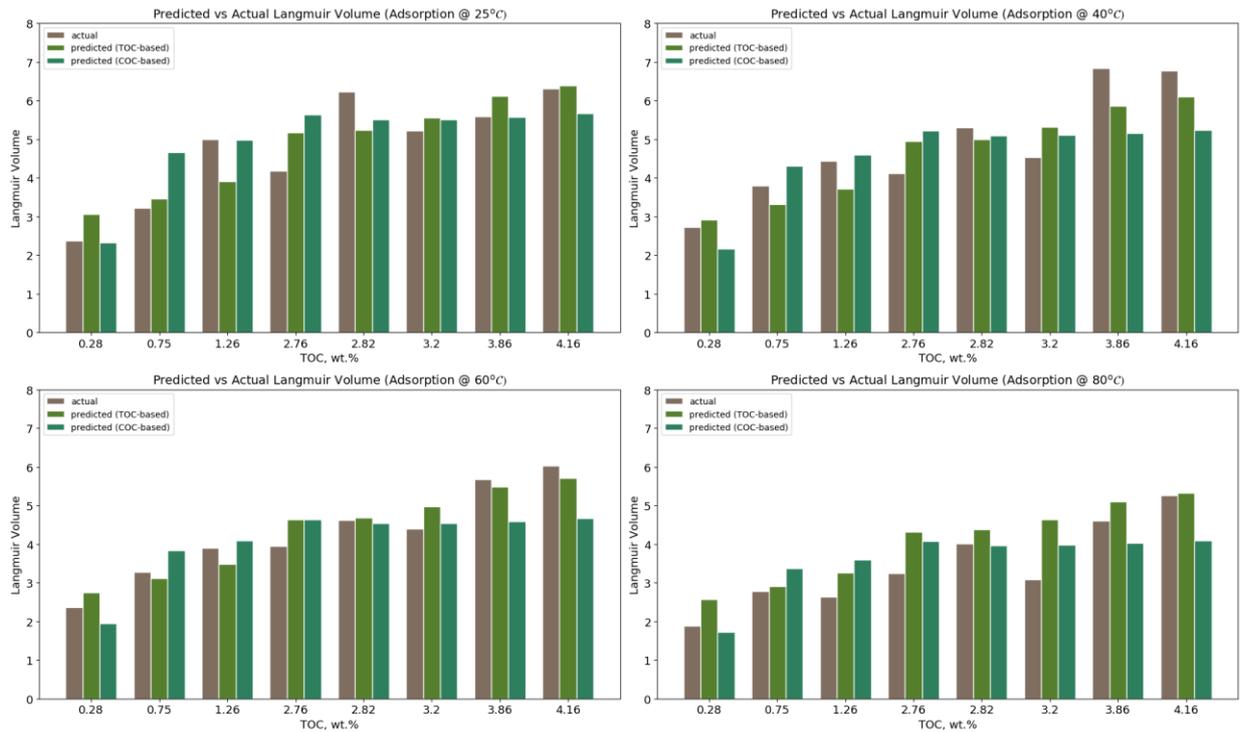
Figure 4.11: Comparing predicted and actual Langmuir volumes for adsorption isotherms
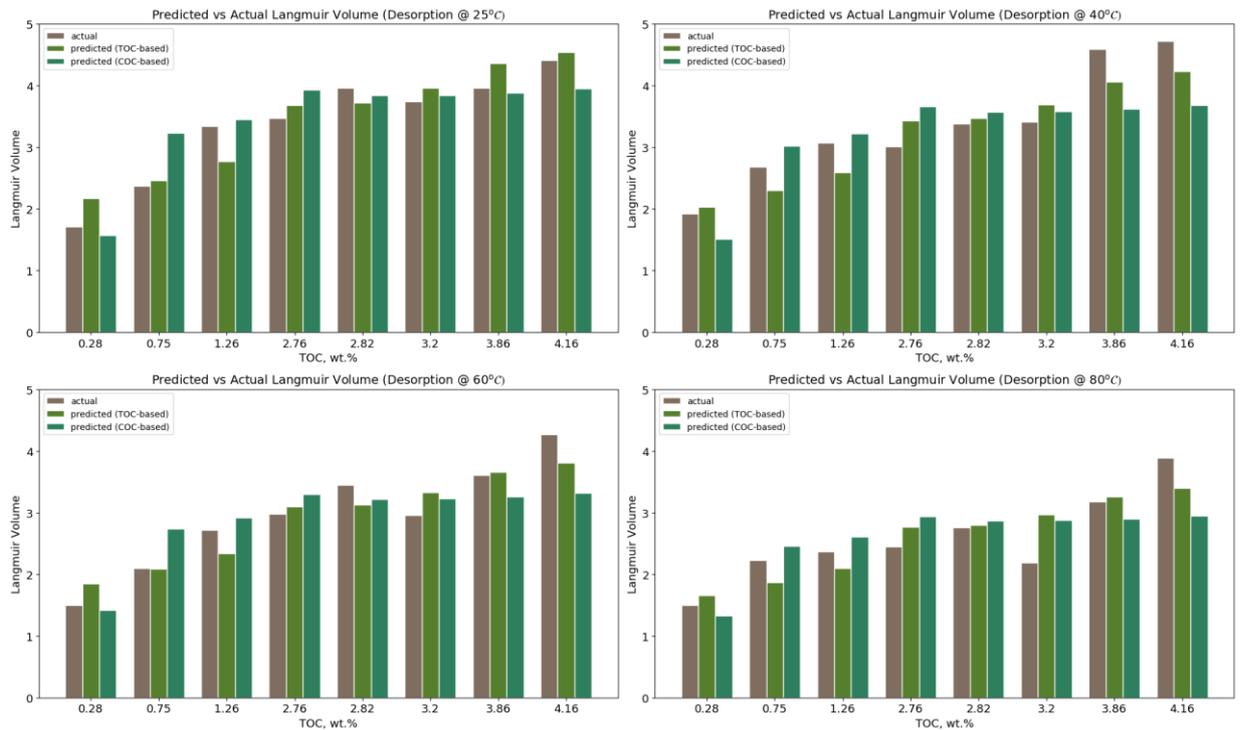
Figure 4.12: Comparing predicted and actual Langmuir volumes for desorption isotherms

Figure 4.13 shows a comparison of the relative errors associated with the TOC-based and the COC-based models for the adsorption isotherms at each test temperature. The errors are of similar magnitudes indicating the reliability of using COC as a single predictor to account for the effect of clay contents in this Formation.
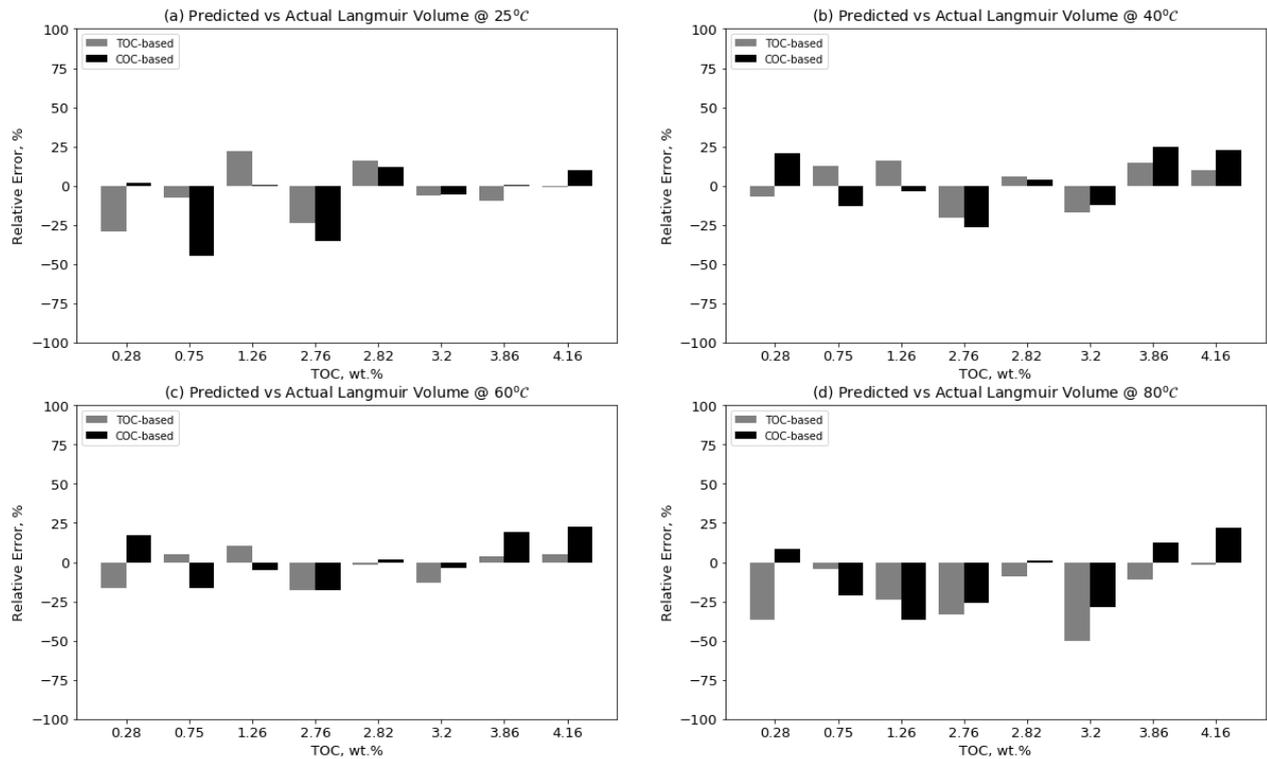
Figure 4.13: Comparing the relative errors in calculated Langmuir volumes for adsorption isotherms

Also, Figure 4.10 shows that a linear relationship exists between Langmuir pressure and Langmuir volume for both sorption processes at each test temperature. If the slope and vertical intercept of the straight-line trend between P_L and V_L are m_1 and c_1 respectively, then:

$$P_L = m_1 \times V_L + c_1 \qquad\qquad 4.14$$

It was also observed that the slopes and intercepts of the lines in Figure 4.10 are quadratic functions of temperature. Therefore, for temperature T in °C, the temperature-dependence of m_1 and c_1 can be represented by the following equations:

$$m_1(T) = a_0 T^2 + a_1 T + a_2 \qquad\qquad 4.15$$

$$c_1(T) = b_0 T^2 + b_1 T + b_2 \qquad\qquad 4.16$$

The values of the coefficients a_i and b_i ($i = 0, 1, 2$) in equations 4.15 and 4.16 are summarized in Table 4.5.

Table 4.5: Coefficients of the quadratic relationship between temperature and each of m_1 and c_1

Process	a_0	a_1	a_2	b_0	b_1	b_2
Adsorption	0.0008	-0.0879	2.5212	-0.0057	0.6213	-9.7478
Desorption	0.0003	-0.0230	0.8049	-0.0019	0.1939	-2.6734

Figures 4.14 and 4.15 show the comparison of the calculated Langmuir pressures for adsorption and desorption isotherms respectively at all test temperatures with the corresponding actual values. Again, the model's predictions adequately match the actual values.
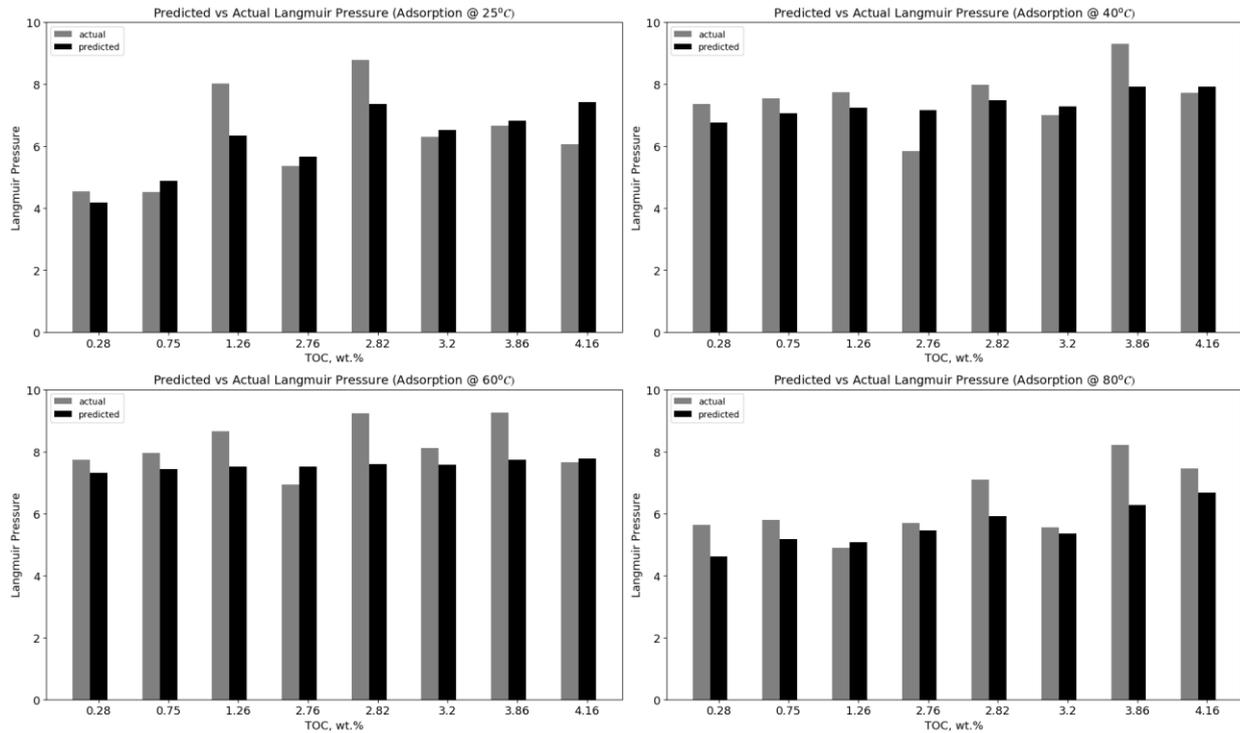
Figure 4.14: Comparing predicted and actual Langmuir pressures for adsorption isotherms

While the analytical models developed here for Langmuir parameters as functions of temperature and rock properties show good performances in predicting experimental values, they should be used with caution considering the assumptions underlying their development. The following assumptions made in their developments may limit their performances to new datasets:

1. The isotherms were characterised by early pore saturation and could only be modelled using a "hybrid" approach.
2. The Langmuir parameters used in developing the models are highly-dependent on the value of adsorbed phase density calculated from D-R model.
3. The samples used in this work are clay-dominated, with TOC ranging from 0.28 – 4.16 wt.%. The models' performances may deteriorate in high TOC samples (with low clay contents).

4. The models' performances may also deteriorate at higher temperatures where the excess adsorption isotherms might peak a little earlier resulting in lower adsorbed phase densities and poorer relationships between Langmuir parameters and TOC contents or COC.
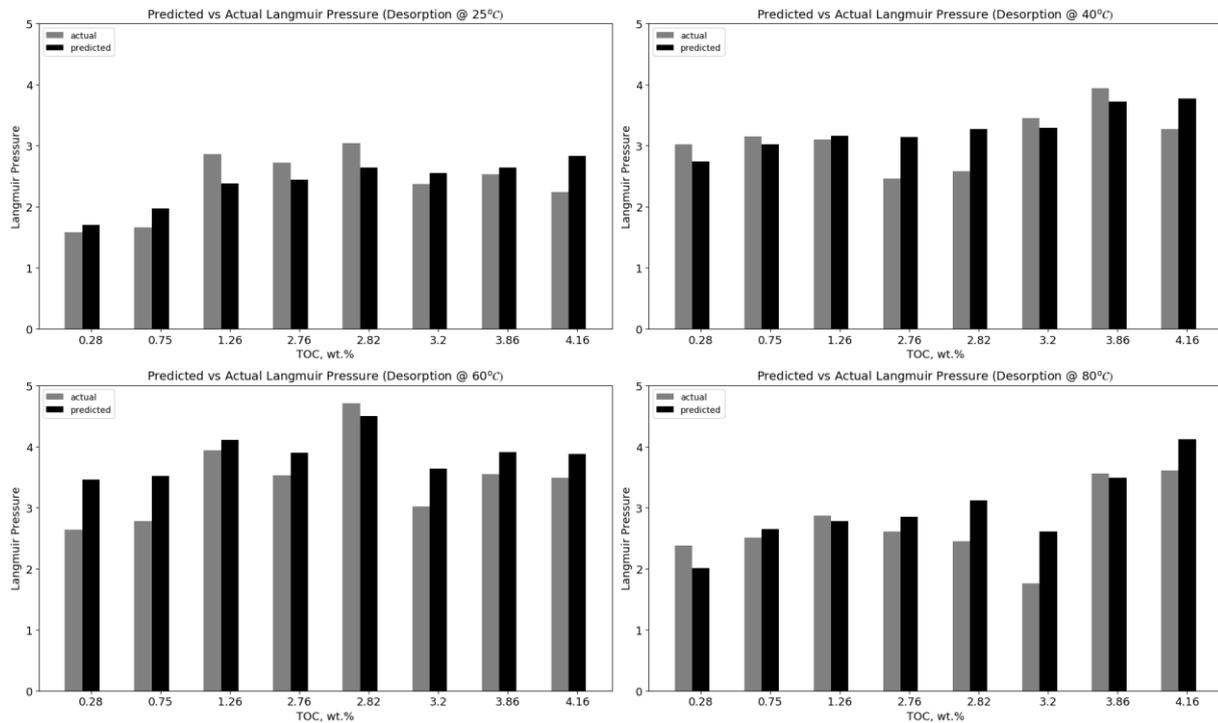
Figure 4.15: Comparing predicted and actual Langmuir pressures for adsorption isotherms

4.4 Conclusions

This study presents the adsorption and desorption isotherms of methane on shale samples from the Ordovician Goldwyer Formation in the Canning Basin of Western Australia. The results showed that methane adsorption in these shales was characterized by early pore saturation resulting in peak excess adsorptions at about 5MPa. Also, for all test temperatures, desorption isotherms were in hysteresis with the adsorption curves resulting in different temperature-dependent model parameters for both processes. Moreover, the size of the hysteresis loop was also affected negatively by temperature. Langmuir volumes for both processes strongly correlated positively with TOC contents but showed a weak to no significant relationship with clay contents. However, the ratio of clay to organic carbon (COC), used to capture the combined effect of both TOC and clay contents showed negative correlations with Langmuir volumes for both adsorption and desorption processes. While the areal hysteresis index (AHI) and improved hysteresis index (IHI) did not show any appreciable correlations with rock properties, the absolute values of the hysteresis area showed strong correlations with TOC content and COC. Lastly, analytical models were developed for the temperature-dependence

of Langmuir volume as functions of TOC contents and COC for each sorption process. The models showed a significant match with experimental results and as such, can be adopted for temperature conditions beyond those investigated in this study.

Chapter 5

Effect of Sorption Hysteresis on Shale Gas Production – A Numerical Simulation Study

5.1 Introduction

Gas production from shale rocks has gained attention worldwide due to advances in hydraulic fracturing and multi-lateral drilling technologies (Yu et al., 2014a, Feast et al., 2015). Shale rocks have an affinity for gas storage in the internal surface area of their pore structures, particularly their organic matter pores, and their natural fractures (Curtis, 2002, Leahy-Dios et al., 2011). Therefore, gas adsorption and desorption mechanisms must be considered during shale gas reserves evaluations and shale gas production predictions respectively (Wang et al., 2016a, Wang et al., 2015, Wei et al., 2013). Research has found that gas production can be significantly under-predicted if "adsorption" is not accounted for in the calculation (Wang et al., 2018, Zhang et al., 2017, Yu et al., 2014a, Feast et al., 2015). The word "adsorption" in this context signals a traditional practice of using adsorption isotherms to obtain desorbed gas volumes during gas production calculations (Wang et al., 2018, Zhang et al., 2017, Yu et al., 2014a, Feast et al., 2015). This practice is based on the assumption that both sorption processes follow the fully reversible monolayer adsorption theory underpinning the Langmuir model (Langmuir, 1918), which is arguably the standard model for shale gas adsorption isotherms (Feast et al., 2015, Yu et al., 2014b). This assumption invariably ignores the hysteresis behaviour of shale gas adsorption-desorption isotherms at in situ conditions.

It has been demonstrated in the preceding chapter that significant hysteresis may exist between the adsorption and desorption isotherms of methane on shale rocks at high pressure and high temperature conditions. These findings support the few existing literatures on this subject (Wei et al., 2017a, Wei et al., 2013, Ekundayo and Rezaee, 2019c, Bhowmik and Dutta, 2019, Zhang et al., 2015b, He et al., 2019). However, while it is well-acknowledged that gas desorption is one of the several complex flow mechanisms characterizing gas production from shale reservoirs (Wang et al., 2018, Wang et al., 2015, Feast et al., 2015, Yu et al., 2014b, Yu et al., 2014a), its true contribution to gas production is often masked by the assumption of reversible sorption isotherms. Despite the published results on the contributions of "adsorption" to shale gas production, we are not aware of any literature that explicitly discussed or the implication for gas production predictions, of using adsorption isotherms in lieu of desorption isotherms.

Hence, the main objective of this chapter is to demonstrate that the existence of gas sorption hysteresis means different gas production performances for adsorption and desorption isotherms. And more so, to show that assuming adsorption equates to desorption can result in wrong estimations of gas production performances.

5.2 Simulation Model

A three-dimensional, single-phase, multiple interacting nested continua (MINC) model (Pruess and Narasimhan, 1985) was developed in CMG-GEM$^®$ to study the influence of sorption hysteresis on gas production from shale rocks. The model was based on GEM's sample dataset (GMFRR005.DAT) for "Fractured Gas Reservoir with MINC" (CMG, 2016). The main reservoir and well parameters used for the "no sorption" (base case) are listed in Table 5.1. The base case was the same for all samples and involves the use of neither adsorption nor desorption isotherm parameters. This was compared with two other cases named adsorption and desorption cases, for which Langmuir parameters at 80°C was used to simulate the contributions or sorption processes to gas production. GEM uses the keywords "ADGMAXC" and "ADGCSTC" to define the Langmuir volume and the reciprocal of Langmuir pressure needed for simulating the desorption process for gas production calculations (CMG, 2016). For simplicity, all natural fractures were assumed to be uniformly spaced and run perpendicular to the I- and J-directions through the entire reservoir thickness.

It is acknowledged that there are several parameters (matrix permeability, fracture permeability, fracture spacing, and so on) that can influence gas production from shale reservoirs. Several sensitivity analyses will be required to quantify the effect of individual parameter on gas production. Examples of such sensitivity studies abound in the literature (Feast et al., 2015, Wang et al., 2018, Yu et al., 2014a, Zhang et al., 2017). The focus of this study was to demonstrate the effect of sorption hysteresis on gas production and as such, keeping other parameters constant was necessary to isolate this effect. A similar approach was adopted by other authors in their work (Feast et al., 2015, Wang et al., 2018, Yu et al., 2014a, Zhang et al., 2017).

Table 5.1: Base case's model parameters

Parameter	Value
Reservoir area, ft^2	1378×1378
Reservoir thickness, ft	66
Number of layers	1
Reservoir pressure, psi	2750
Reservoir temperature, ^{o}F	176
Initial gas saturation, %	100
Matrix porosity, fraction	0.04
Matrix permeability, mD	1×10^{-5}
Fracture porosity, fraction	1×10^{-3}
Fracture permeability, mD	1×10^{-3}
Fracture spacing, ft	26
Compressibility factor, psi^{-1}	1×10^{-6}
Rock density, g/cc	2.65
Number of producing wells	1
Wellbore radius, ft	0.12
Minimum flowing BHP, psi	350
Duration, year	10

5.3 Results and Discussions

The results of the numerical simulation with and without sorption parameters are shown in Figure 5.1 for all eight samples. For each sample, the base case (no-sorption case) ultimately gave the lowest gas production rate and 10-year cumulative gas production compared to the other two cases. This confirms the importance of gas sorption parameters on shale gas production calculations. However, there is no significant difference between the gas production for the base case and each of the two comparison cases during the early stages of gas production. This suggests that the effect of gas adsorption or desorption is minimal during the early time. Given the assumption of 100% initial gas saturation, it is expected that the volume of free gas in the reservoir will be significant. For the base case, this volume is the simulated original gas in-place (OGIP) volume estimated as 862 MMSCF for all the samples. As summarized in Table 5.2, the difference between this volume and the OGIP for the adsorption case for each sample represents the adsorbed gas content at the initial reservoir conditions.

Table 5.2: Contributions of Gas Adsorption to Original Gas in Place

Sample	OGIP*, MMSCF	Adsorbed Gas Vol., MMSCF	% Contr. of Adsorbed Gas
GTh-1	1347	485	36.0
GTh-2	1559	697	44.7
GTh-3	1661	799	48.1
GTh-4	1837	975	53.1
GTh-5	1696	834	49.2
GTh-6	1573	711	45.2
GTh-7	1936	1074	55.5
GTh-8	2122	1260	59.4

* OGIP for adsorption cases

For all the samples, the adsorption case gave the highest production rate and cumulative gas production after 10 years resulting in 8.4 – 22.2% additional gas production (relative to the base case). This agrees with existing literature on the effect of adsorption on shale gas production (Wang et al., 2018, Zhang et al., 2017, Yu et al., 2014a, Feast et al., 2015). While desorption cases also gave higher gas production performances than the base case, the additional gas productions due to desorption are less than the corresponding values for the adsorption cases (Figure 5.1). This confirms that the use of adsorption model parameters, which assumes no hysteresis exists between the sorption processes, can lead to a significant over-prediction of gas production. The difference between the cumulative gas productions from the two sorption cases was used to quantify the effect of sorption hysteresis on gas production.

It follows from the above discussion that while gas sorption generally has a positive effect on gas production from shale reservoirs, the effects are often exaggerated by the assumption of fully reversible sorption isotherms. Where hysteresis exists between adsorption and desorption isotherms, the (Langmuir) model parameters are usually lower for desorption isotherms than for the adsorption counterparts and the differences will directly translate to lower gas production with the desorption parameters.
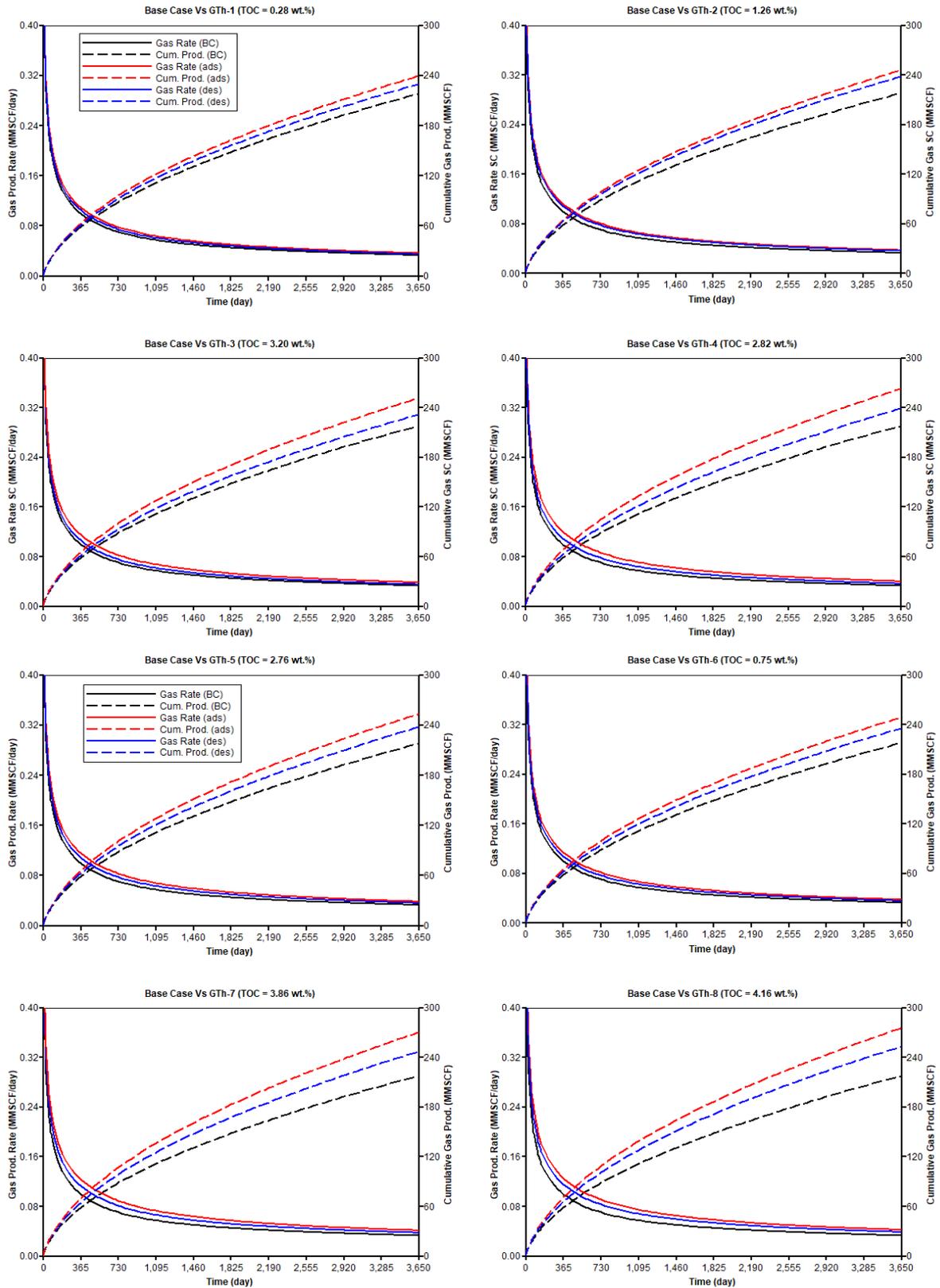
Figure 5.1: Gas production performances showing the effect of gas sorption hysteresis
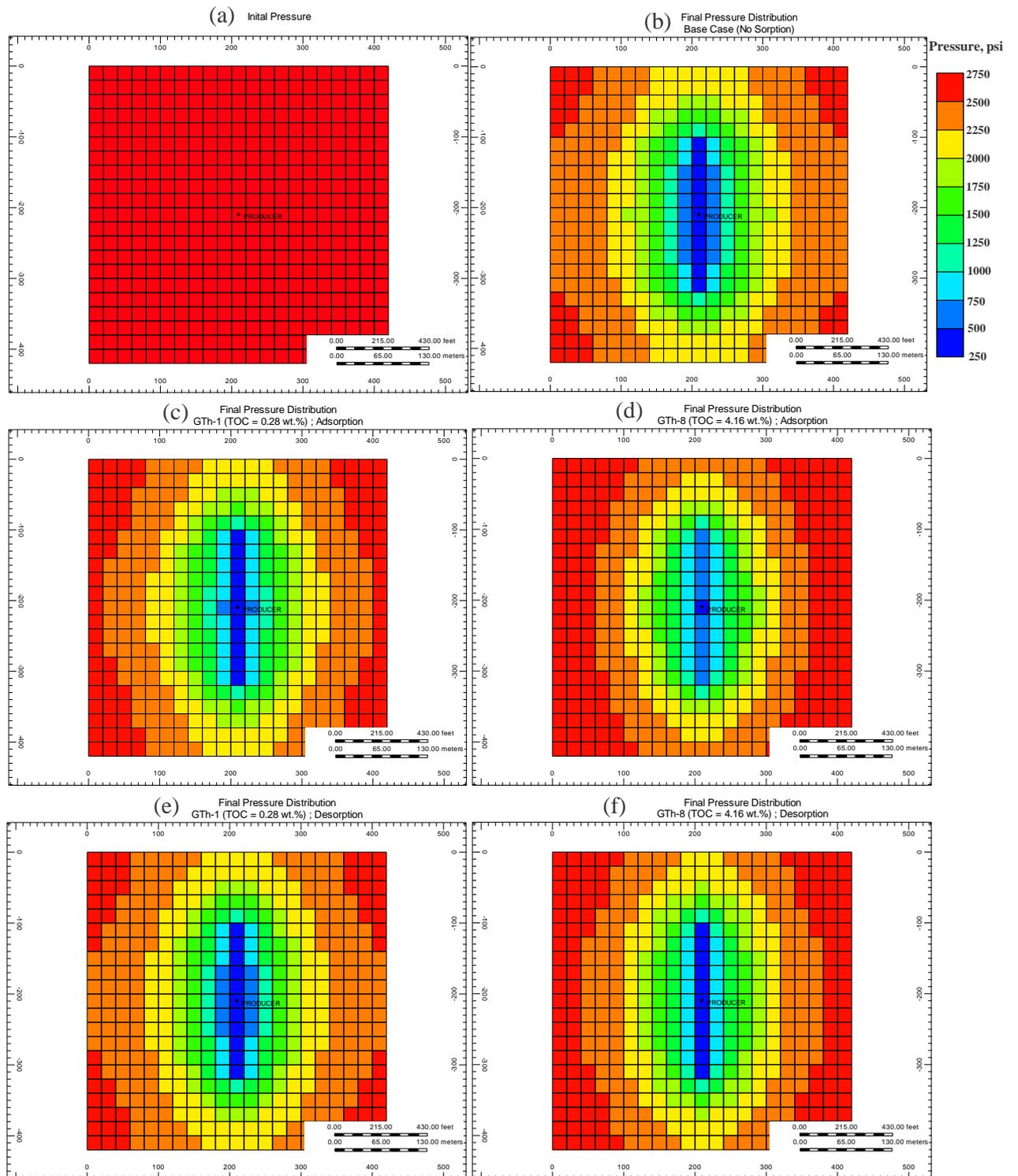
Figure 5.2: Sample pressure distributions for all three simulated scenarios

Figure 5.2(a) shows the initial pressure distribution in the simulation grids. This was the same for all the simulated cases and for all the samples. On the other hand, Figures 5.2(b-f) show the final simulated pressure distributions for the base case, and the adsorption and desorption cases for two selected samples (GTh-1, the lowest TOC sample and GTh-8, the highest TOC sample). For each of these Figures (5.2 b-f), the final pressure is lowest (and approximately equal to the minimum bottom-hole flowing pressure shown in Table 5.1) in the region around the wellbore. Also, while none of the scenarios achieved a complete sweep, it is obvious that the areas drained by the different scenarios are significantly different. To achieve the level of gas production performances shown in Figure 5.1, the base case had drained a lot more area than each of the other cases. Thus, the final pressure at any point (away from the wellbore) is much lower compared to the other cases. Similarly, a comparison of the final pressure distributions for the adsorption and desorption cases shows that for each of the two selected samples, the desorption case drained more area to achieve its gas production performances. Thus, it has a lower final pressure at any given location (away from the wellbore) than the corresponding adsorption case.

5.3.1   Effect of Rock Properties

It was demonstrated in Chapter 4 that TOC content was the primary factor affecting the adsorption and desorption parameters of the Goldwyer Formation. Considering the abundance of clay minerals in this Formation, and given the poor relationship between clay contents and sorption parameters, the parameter Clay to-Organic Carbon ratio (COC) was used to capture the combined effect of both TOC content and clay content.

As shown in Figure 5.3(a), the difference in production gains (relative to the base case) between the adsorption and desorption cases follows a positive linear trend with TOC content. This is expected given a similar relationship between Langmuir volumes and TOC contents presented in Chapter 4 for these samples. The lower value of the coefficient of determination (R^2 = *0.7261*) may be related to the effect of Langmuir pressure which, as stated in Chapter 4, showed no significant correlation with TOC contents. The effect of adsorbed phase density on Langmuir volume is another possible reason for the low R^2 value. As discussed in Chapter 4, the calculated values of the adsorbed phase density at 80°C, were much lower for some samples than others irrespective of their TOC content. This resulted in absolute isotherms that deviated slightly from the expected trend with TOC content. Consequently, the resultant Langmuir volumes for both adsorption and desorption also deviated accordingly, with the deviations (as shown in Figure 4.7, Chapter 4) being more pronounced for desorption at this temperature.
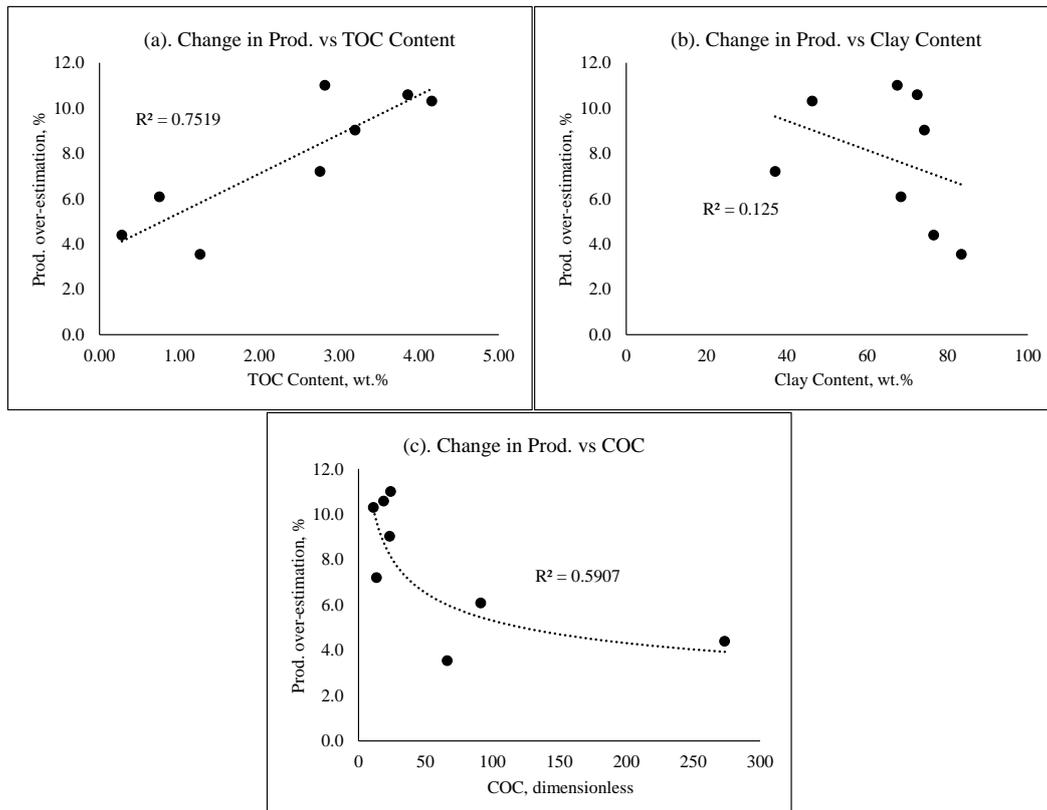
Figure 5.3: Relationship between relative production over-prediction and rock properties

As shown in Figure 5.3(b), a very weak negative relationship exists between the relative amount of gas production over-estimated and clay contents. Again, this follows a similar observation like the one reported in Chapter 4 between Langmuir volumes and clay contents. Lastly, Figure 5.3(c) shows a negative non-linear correlation between production over-prediction and COC. The lower R^2 value (compared to Figure 5.3(a)) is a reflection of the opposing effects of TOC contents and clay contents.

Lastly, a comparison of the final pressure distributions for the two samples (shown in Figure 5.2) shows that for each process, sample GTh-8 (TOC = 4.16 wt.%) drained less area and thus has a higher final pressure at any given grid-cell compared to sample GTh-1 (TOC = 0.28 wt.%) suggesting a relationship may exist between the final pressure at a given location and TOC content. An example of such a relationship is shown in Figure 5.4.
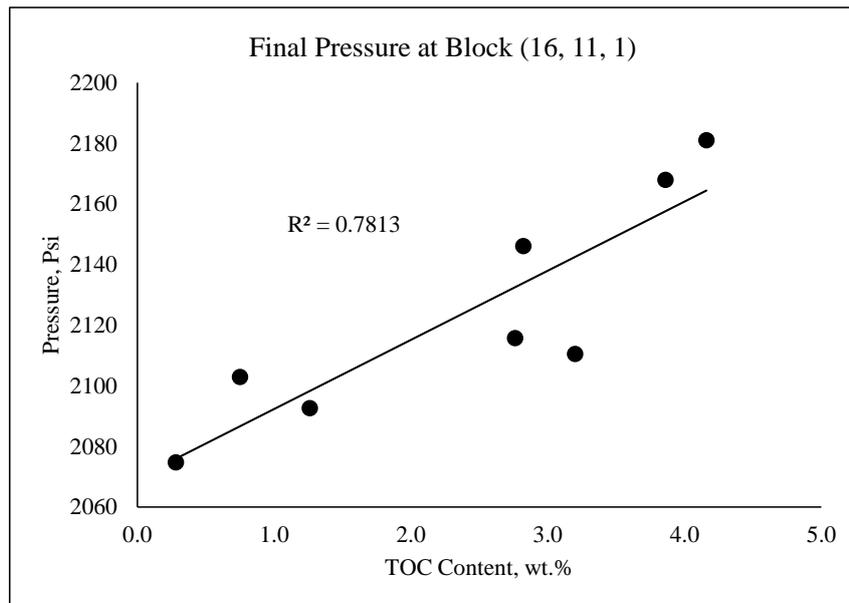
Figure 5.4: An example of the relationship between final block pressure and TOC content (adsorption case)

5.3.2   Effect of Sorption and Sorption Hysteresis

Given the observed differences in gas productions between the two comparison cases relative to the base case, an attempt was made to see the relationships between the relative amounts of these differences and each of the hysteresis quantifiers discussed in Chapter 4. Figure 5.5(a-c) below shows the relationships between the gas production over-predictions and the hysteresis quantifying parameters, namely hysteresis area, areal hysteresis index, and improved hysteresis index. Unsurprisingly, the production over-predictions did not show a significant correlation with any of the parameters.
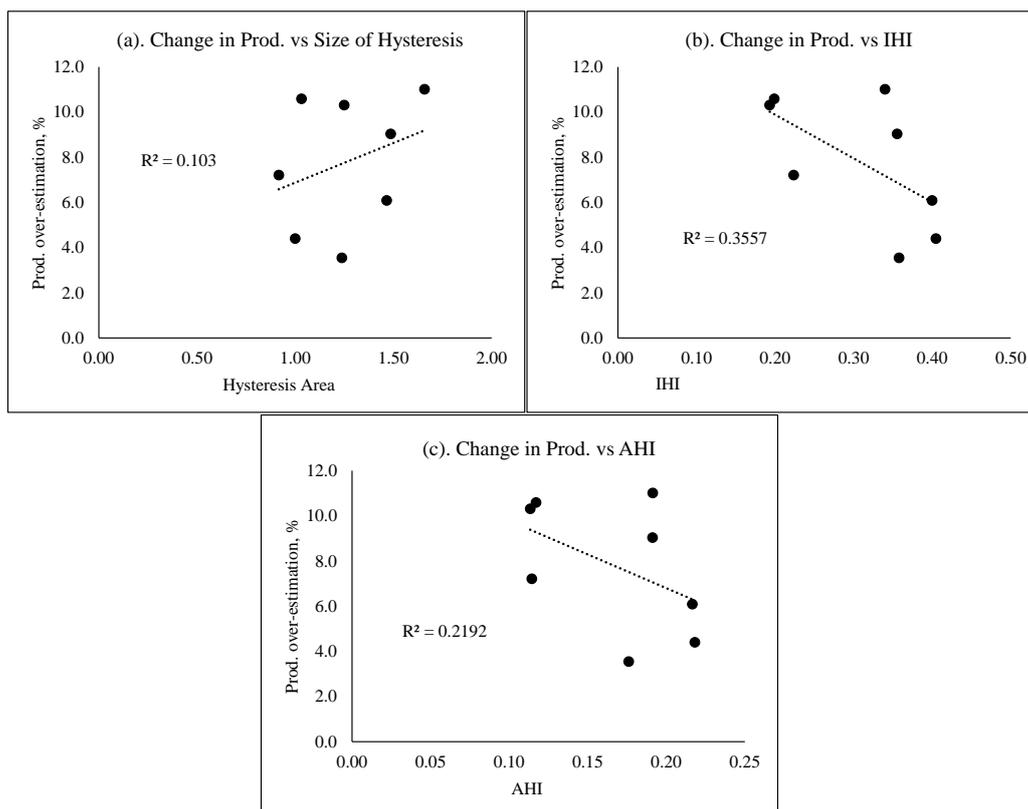
Figure 5.5: Relationship between relative production over-prediction and Hysteresis Quantifiers

As discussed in Chapter 4, all the hysteresis quantifying parameters deviated at 80°C from the expected decreasing trend with temperature possibly due to methane readsorption during the desorption process and/or due to possible gas trapping caused by irreversible adsorption-induced structural changes to the samples' pore systems. However, further studies would be required to validate this hypothesis.

Lastly, one of the conclusions from Chapter 4 of this thesis was that Langmuir parameters would be lower for desorption than the corresponding values for adsorption due to hysteresis between the two processes. Given the strong positive correlations between Langmuir volumes and TOC contents for each of the processes, it is expected that the difference in Langmuir volumes (ΔV_L) between the sorption processes would also correlate positively with TOC content as shown in Figure 5.6(a). In fact, ΔV_L could also be used a measure of the size of hysteresis between adsorption and desorption. Thus, it is obvious from Figures 5.3(a) and 5.6(a), that the relative difference in gas production between adsorption and desorption would also correlate positively with this new measure of hysteresis. This relationship is shown in Figure 5.6(b).
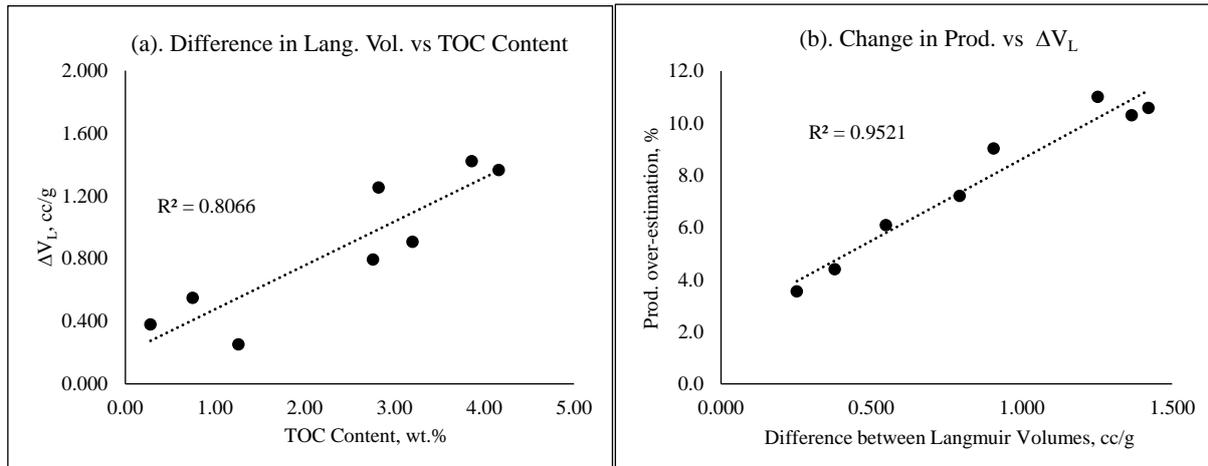
Figure 5.6: Relationship between differential Langmuir volumes and (a) TOC content,
(b) relative amount of gas over-predicted.

5.4 Conclusions

This chapter presented the effect of gas sorption and sorption hysteresis on shale gas production. The results showed that although gas sorption has a positive effect on gas production from shale reservoirs, using adsorption model parameters to calculate desorbed gas volumes during gas production could lead to production over-prediction. In summary, it can be concluded that:

1. Gas sorption contributes significantly to both estimated reservoir gas volumes and gas production. Thus, neglecting the gas sorption during gas production predictions can lead to under-estimation of gas production performances.

2. The relative amounts of gas over-predicted by neglecting hysteresis between adsorption and desorption showed a positive correlation with TOC content. This is expected given the positive correlation between Langmuir volumes and TOC contents.

3. The relative amount of gas over-predicted negatively correlated, albeit, weakly with clay content but moderately with COC, a parameter introduced to better capture the contribution of clay contents.

4. No significant relationship was found between each of the hysteresis quantifying parameters (hysteresis areas, areal hysteresis index, and improved hysteresis index) and the relative amount of gas over-predicted. While the exact reason for this was not established in this thesis, it was postulated that gas readsorption during desorption at high temperature and/or irreversible structural changes caused by adsorption could be

responsible for this observation. However, further studies would be required to ascertain this proposition.

5. A strong positive correlation was found between the relative amount of gas over-predicted and the difference in Langmuir volumes between adsorption and desorption isotherms, which is another indication of the extent of sorption hysteresis.

Lastly, while this study offers insights into the effect of sorption hysteresis on gas production, it is acknowledged that gas transport in shale is a multiphysics process and the inclusion of other flow mechanisms may affect the simulation outputs. However, in keeping with the objectives of this study, it was necessary to keep other parameters constant to isolate the effect of sorption parameters and hysteresis on gas production. Several publications exist that adopted similar approach in their studies (Feast et al., 2015, Wang et al., 2018, Yu et al., 2014a, Zhang et al., 2017).

Chapter 6

Conclusion and Recommendations

6.1 Conclusions

The primary aim of this research was to investigate the hysteresis between methane adsorption and desorption isotherms measured at high temperature and pressure conditions for selected Goldwyer shale samples and their effects on gas production from shale reservoirs. To achieve these objectives, series of high-pressure methane adsorption and desorption experiments were conducted using a medium-ranked, volatile bituminous coal in the first part, and eight shale samples from the Ordovician Goldwyer Formation in the Canning Basin, Western Australia in the latter part of this thesis. The samples were first characterised using conventional techniques low-pressure nitrogen adsorption tests to determine the pore-size distributions and micro-structural properties like specific surface areas and pore volumes, and x-ray diffraction for mineral composition studies. In addition to characterization techniques, geochemical analysis with RockEval® pyrolysis was also conducted on the shale samples to establish the total organic carbon (TOC) contents and its associated parameters.

The part of this thesis involving the coal sample explored the effects of equation of states on methane adsorption and desorption isotherms, as well as their associated model parameters and sorption hysteresis. The findings from this part suggested that equation of states has a significant effect not only on the measured isotherms, but also on the type and size of hysteresis between adsorption and desorption isotherms of methane on coal. This provided new insights into equation of state as a possible cause of the observed hysteresis between methane adsorption and desorption isotherms at high-pressure and temperature conditions.

The latter part of this thesis involved the use of shale samples to investigate the effect of temperature on sorption hysteresis as well as the relationships between sorption hysteresis and rock properties. Following the mathematical modelling of the measured isotherms using a combination of DR and Langmuir models, the relationships between the calculated Langmuir parameters and selected TOC and clay contents of the samples were determined for both adsorption and desorption processes. These relationships gave insights which formed the basis of novel analytical models developed for Langmuir parameters as functions of temperature and rock properties (TOC contents and COC, a parameter which combines the clay and TOC contents) for both adsorption process and, for the first time, desorption process. Lastly, a

numerical block simulation model was set-up using CMG-GEM® to study the effects of observed gas sorption hysteresis on gas production from shale gas reservoirs.

In this chapter, each of the key chapters of this thesis is summarized and its main findings are further discussed. Also, some suggestions are made for future direction in advancing this research subject.

6.1.1   Effects of Equation of States on Gas Sorption Isotherms and Hysteresis

The first broad objective of this thesis, as stated in Chapter 1, was to investigate the effect of equation of state (EOS) on high-pressure methane adsorption and desorption isotherms, the associated model parameters and other parameters derived from these. High-pressure adsorption of supercritical methane is routinely used to study the adsorption capacity of shale reservoirs and coal-seams. However, there is no agreement on the best EOS for computing gas densities required for experimental data analysis making it difficult to compare or reproduce published data. Thus, this aspect of this thesis aimed, in part, to alert fellow researchers of potential errors that might be caused by their choice(s) of EOS for this type of study. Secondly, it is particularly important to choose the most suited EOS for the rest of this research. These objectives were addressed in Chapter 3 of this thesis.

In that chapter, a synthetic coal sample was used to study methane adsorption and desorption at 25°C and 40°C. Six sets of adsorption and desorption isotherms calculated, from the same experimental data, using different equations of states were compared with the reference isotherms calculated using the system's inbuilt software (NIST-Refprop®). The software used the combination of McCarty & Arp EOS (for helium) and Setzmann & Wagner's EOS (for methane) for transforming the measured pressure and temperature data to sorption isotherms. The key findings from this chapter can be highlighted as follows:

1. Measured adsorption and desorption isotherms, resulting model parameters as well as the type and extent of the hysteresis between them varied significantly with the applied EOS

2. The type of sorption hysteresis was found to be related to how the Z-factor of methane deviated from the reference EOS (Setzmann & Wagner's EOS); negatively deviating EOS produced positive sorption hysteresis while positively deviating ones gave negative sorption hysteresis for the same dataset.

3. Due to the significant contribution of adsorption to the gas contents in unconventional gas reservoirs, deviations of estimated initial gas in-place correlated with those of Langmuir volumes relative to the reference adsorption data.

4. Soave-Benedict-Webb-Rubin's (SBWR) EOS (Soave, 1999) gave the lowest deviations from the reference adsorption isotherms (obtained from the system's inbuilt software), SBWR-EOS resulted in sorption hysteresis that conforms to reality (as evident from existing literature). Thus, it was selected for the rest of this research.

6.1.2   Experimental Investigation and Mathematical Modelling of Sorption Hysteresis

The next objective of this research was in two folds. The first was to investigate hysteresis between the methane adsorption and desorption isotherms and how it relates to temperature, selected shale properties. In furtherance to that, this research also sought to develop analytical models for Langmuir parameters as functions of temperature and selected shale properties. These objectives were the key focus of Chapter 4 of this thesis.

In that chapter, methane adsorption and desorption isotherms were measured at four different temperatures on selected shale samples from the Ordovician Goldwyer Formation. The samples were previously characterised in Chapter 2 of this thesis using different techniques. The samples exhibited high clay contents dominated by illite and as such, their methane adsorption isotherms deviated from the expected behaviour with pressure. Methane adsorption capacities of these samples appeared to have been reduced by illite precipitation into the organic micropores resulting in lower amounts been adsorbed than expected. The excess adsorption isotherms reached maximum values in the neighbourhood of 5MPa, much lower than most published values on this subject, as a result of early pore saturation. Such a behaviour could only be satisfactorily modelled using a hybrid approach involving DR-model to estimate the adsorbed phase densities followed by Langmuir model to parameterise the resulting absolute (adsorption and desorption) isotherms.

The isotherms followed the expected negative trend with temperature and positive trend with TOC contents. However, no discernible correlation could be established between the measured isotherms and clay contents. Similar observations were made between Langmuir volumes and these rock properties. The effects of clay contents were therefore inferred from the correlations of the Langmuir parameters with the novel ratio of clay to organic carbon, COC, which gave (mild to strong) negative correlations with Langmuir parameters.

Furthermore, all the samples exhibited significant hysteresis between the adsorption and corresponding desorption isotherms and the absolute area enclosed by the hysteresis loop followed the same relationships with TOC content and COC as Langmuir volume.

The second part of this objective was achieved by developing novel analytical models for temperature-dependent Langmuir parameters, for both adsorption and desorption, as functions of TOC content and COC.

Lastly, the main findings from this aspect of this study are:

1. Due to their high illite compositions, the shale samples used in this thesis exhibited methane adsorption isotherms characterised by early pore saturation leading to excess adsorption peaks at about 5MPa

2. Significant hysteresis was observed between adsorption and desorption isotherms at all test temperatures resulting in lower Langmuir parameters for desorption compared to the corresponding adsorption isotherms

3. Strong positive correlations were observed between Langmuir volume and TOC content for both adsorption and desorption. Reflecting the negative impact of clay contents on the adsorption capacities of the samples used in this study, COC negatively correlated with Langmuir volume for both adsorption and desorption.

4. The commonly used indices (areal hysteresis index (AHI) and improved hysteresis index (IHI)) for quantifying the size of sorption hysteresis could not be correlated with rock properties and their relationships with temperature were also inconsistent. Conversely, the absolute area of the hysteresis loop was found to give strong correlations with TOC content and COC.

5. The analytical models developed for Langmuir parameters as functions of temperature and rock properties gave a significant match with experimental data and may therefore be useful in studying methane adsorption and desorption for similar shale Formations or beyond the experimental conditions investigated in this thesis.

6.1.3 Investigation of the Effects of Sorption Hysteresis on Shale Gas Production

The last primary objective of this thesis was to investigate the effect of the observed hysteresis between methane adsorption and desorption isotherms on shale gas production. This objective was achieved through a numerical simulation study detailed in Chapter 5 of this thesis. It is commonly assumed that adsorption isotherms can be used in simulating shale gas production on the basis that methane adsorption would be fully reversible at high-pressure, high-

temperature conditions (Kierlik et al., 2002, Monson, 1983). In addition to few existing evidences of hysteresis between methane adsorption and desorption isotherms at high pressure and temperature conditions (Bhowmik and Dutta, 2019, Wei et al., 2013, Wei et al., 2017a), this research also found that significant hysteresis between these sorption processes. Thus, a 3D simulation model was developed in CMG-GEM® to quantify the difference in gas production caused by the observed sorption hysteresis. The results showed that although gas sorption has a positive effect on shale gas production, the true contribution of gas sorption may be significantly exaggerated by the assumption of fully reversible sorption isotherms. Where hysteresis exists between adsorption and desorption isotherms, desorption would have lower Langmuir model parameters compared to the corresponding adsorption isotherm and by implication, desorption-based gas production would be lower.

In summary, the key findings from Chapter 5 are highlighted as follows:

1. Gas sorption is very important for gas production from shale reservoirs. Neglecting its contribution can lead to significant under-estimation of gas production performances
2. Significance differences were observed between the adsorption-based gas productions compared to the desorption-based gas productions. These differences represent the volume or undesorbed gas due to sorption hysteresis
3. Gas production difference due to sorption hysteresis was found to show a positive correlation with TOC contents and a negative correlation with clay contents, as inferred from the correlation with COC.
4. Lastly, while the production over-estimation did not give a significant correlation with any of the hysteresis quantifying parameters, it was found to strongly correlate with the difference in Langmuir volumes between adsorption and desorption isotherms.

6.2 Limitations and Recommendations

This thesis provided useful insights into some of the key issues in high-pressure shale gas adsorption and desorption processes. The choice of EOS was identified as a potential reason for the observed hysteresis between adsorption and desorption isotherms of methane on shale rocks at high-pressure, high temperature conditions. It was also demonstrated that high illite content in shale samples could lead to early pore saturation by methane. When that happens, the excess isotherms would exhibit maximum adsorbed amounts at much lower pressures than the commonly cited 10 - 15MPa range (Zhang et al., 2016). In such cases, Langmuir isotherm might result in relatively low values of adsorbed phase density and consequently, exaggerated

absolute adsorptions and Langmuir parameters. A hybrid modelling approach, involving the use of DR model to estimate adsorbed phase density followed by the traditional Langmuir model to fit the resultant absolute isotherms, is recommended.

Given the limited number of samples used in this research, it is recognised that more work would be required to validate the results and conclusions presented in this thesis. The following points could guide future research to address the limitations of this research:

1. The adsorption and desorption isotherms measured in this thesis were based on high purity (99.9%) methane to determine the shale gas adsorption and desorption capacities of the Goldwyer Formation. Naturally, shale gas contains different impurities such as CO_2 and N_2 which also have significant adsorption and desorption tendencies in shale. It is therefore recommended that a more representative adsorbate be used to better quantify the sorption hysteresis in this Formation and develop more representative predictive models for Langmuir parameters.

2. The analytical models developed in this thesis did not take into consideration, the contribution of the individual mineral constituent of the shale rock. To fully understand how each mineral affects the adsorption/desorption in the Goldwyer shales, it may be necessary to expand the models to include the relationships of Langmuir parameters with the key minerals found in the shales.

3. The numerical model used to study the effect of sorption hysteresis on gas production is a single-phase homogeneous block model. In addition to reducing the adsorption capacity of shales, the presence of water has also been reported to cause sorption hysteresis by gas trapping. Therefore, a two-phase (gas-water) simulation model can be developed to further validate the respective contributions of adsorption and desorption processes in the presence of residual moisture (water saturation).

4. The observed deviation at $80^{o}C$, of the hysteresis quantifying parameters from the decreasing trend with temperature, was hypothetically attributed to re-adsorption of methane during the desorption process and/or gas trapping caused by irreversible structural changes to the pore systems induced by adsorption. To verify these assumptions, it is therefore recommended that the experimental set-up used in this study be modified to measure the structural changes associated with sorption processes.

Appendix A

TOC and Total Clay Contents from literature

Table A1: Additional data used in Figure 2.14

Source	Sample ID	TOC content wt.%	Total Clay content wt.%	Source	Sample ID	TOC content wt.%	Total Clay content wt.%
Wang and Guo (2019)	MF3–1	0.97	51.0	Chen et al. (2018)	S-1	2.19	53.7
	MF4–1	1.87	72.0		S-2	0.33	14.2
	Y88–1	0.97	55.0		S-3	1.67	35.6
	Y88–2	1.90	52.0		S-4	1.72	38.8
	Y88–3	4.62	45.0		S-5	0.78	44.0
	Y88–4	3.21	56.0		S-6	0.12	22.6
Wang et al. (2016b)	LQ-1	7.68	35.4		S-7	0.62	31.3
	LQ-6	4.24	34.8		S-8	1.53	42.2
	LQ-9	2.18	37.8		S-9	1.12	38.5
	LQ-13	1.46	48.7	Pan et al. (2016)	Sample 1	1.42	45.1
	GS-6	5.23	34.1		Sample 2	1.01	44.9
	GS-7	4.82	38.5		Sample 3	1.56	44.3
	GS-15	1.76	36.1		Sample 5	2.62	38.5
	CX-18	2.17	27.2		Sample 6	3.47	52.5
	HW-5	4.40	20.1		Sample 7	3.41	49.2
	HW-9	3.90	28.7		Sample 8	3.98	52.5
Guo et al. (2017)	T3t-1	0.87	33.0	Chen et al. (2019a)	Y-1	0.73	38.5
	T3t-2	2.24	48.0		Y-2	0.39	39.7
	T3t-3	2.57	49.0		Y-3	0.74	54.4
	T3t-4	1.22	36.0		Y-4	0.54	44.0
	T3t-5	2.42	43.0		Y-5	0.99	32.3
	T3h-1	1.05	46.0		Y-6	0.97	47.1
	T3h-2	0.70	42.0		Y-7	1.72	43.0
	T3h-3	0.98	45.0		Y-8	1.63	41.3
	T3h-5	1.30	47.0		Y-9	0.74	47.6
	T3h-6	5.76	55.0	Cao et al. (2015)	CJG-7	7.28	21.8
	T3h-7	1.55	60.0		CJG-10	7.74	19.3
	T2-3k-1	0.50	26.0		QT-1	2.75	35.1
	T2-3k-2	0.95	40.0		QT-2	3.59	35.4
	T2-3k-3	0.81	42.0		QT-4	2.69	47.9
	T2-3k-4	0.76	41.0		QT-5	2.76	45.7
	J2q-1	1.02	58.0		NSH-1	4.4	34.8
	J2q-2	1.17	35.0		NSH-6	4.59	35.1
	J2q-3	1.38	57.0		MB-1	2.22	50.8
	J2q-4	1.62	52.0		MB-4	2.09	62.5
	J2kz-1	1.48	36.0				
	J2kz-3	2.39	36.0				
	J1y-1	2.47	43.0				
	J1y-2	5.35	70.0				
	J1y-3	5.33	70.0				
	J1y-5	4.59	60.0				
	J1y-6	1.55	55.0				

Appendix B

Equations of State

This section of has been published as a supporting material in the article titled "**Effect of Equation of States on High Pressure Volumetric Measurements of Methane-Coal Sorption Isotherms - Part 1: Volumes of Free Space and Methane Adsorption Isotherms**" and is available online at .

B1. **Cubic Equations of State**

In terms of molar volume, Van der Waal type cubic equations of state assume the following general mathematical form:

$$P = \frac{RT}{(v_m + \beta)} - \frac{a(T)}{(v_m + \delta)(v_m + \gamma)} \qquad B1$$

Where the parameters P, R and T are the pressure, gas constant and temperature respectively; δ and γ are EOS-specific parameters while parameters $a(T)$ and β are similarly defined for all Van der Waal type equations of state as:

$$a(T) = a = \frac{\Omega_a \alpha(T) R^2 T_c^2}{P_c} \qquad B2$$

$$\beta = -b \qquad B3$$

The parameter b is given as:

$$b = \frac{\Omega_b R T_c}{P_c} \qquad B4$$

Where Ω_a, Ω_b EOS-specific constants and Tc, Pc are the critical temperature and critical pressure of the gas respectively. The temperature dependent parameter $\alpha(T)$ is also EOS-specific and is given as:

$$\alpha(T) = \left(1 + m\left(1 - T_r^{\frac{1}{2}}\right)\right)^2 \qquad B5$$

Where:

$T_r = \frac{T}{T_c}$ is the reduce temperature and m is EOS-specific.

In terms of the molar volume, the *Equation B1* can be expanded to yield

$$v_m{}^3 + v_m{}^2 \left(\beta + \delta + \gamma - \frac{RT}{P} \right) + v_m \left(\beta\delta + \beta\gamma + \delta\gamma - \frac{RT}{P}\delta - \frac{RT}{P}\gamma + \frac{a}{P} \right)$$
$$+ \left(\frac{a}{P}\beta - \frac{RT}{P}\delta\gamma + \beta\delta\gamma \right) = 0 \qquad\qquad B6$$

The molar volume of the gas can be obtained as the lowest root of *Equation B6* for a given EOS. Alternatively, *Equation B6* can be expressed in terms of the gas compressibility factor, Z as:

$$Z^3 + Z^2 \left(\frac{P}{RT}(\beta + \delta + \gamma) - 1 \right) + Z \left(\frac{P^2}{R^2T^2}(\beta\delta + \beta\gamma + \delta\gamma) - \frac{P}{RT}\delta - \frac{P}{RT}\gamma + \frac{P}{R^2T^2}a \right)$$
$$+ \left(\frac{P^2}{R^3T^3}a\beta - \frac{P^2}{R^2T^2}\delta\gamma + \frac{P^3}{R^3T^3}\beta\delta\gamma \right) = 0 \qquad\qquad B7$$

The largest root of *Equation B7,* solved iteratively, is the z-factor of the gas for the given EOS parameters a, β, δ *and* γ.

Also, for use in subsequent subsections, two additional parameters *A & B* are generally defined as

$$A = \frac{aP}{R^2T^2} \qquad\qquad B8$$

$$B = \frac{bP}{RT} \qquad\qquad B9$$

B1.1   Soave-Redlich-Kwong (SRK) Equation of State
The SRK-EOS is given as:

$$P = \frac{RT}{(v_m - b)} - \frac{a(T)}{v_m(v_m + b)} \qquad\qquad B10$$

Compared to *Equation B1*, it can be seen that $\beta = -b$; $\delta = 0$ and $\gamma = b$. The SRK-EOS is also characterized by $\Omega_a = 0.42747$; $\Omega_b = 0.08664$ *and the* parameter m is given as:

$$m = 0.480 + 1.574\omega - 0.176\omega^2 \qquad\qquad B11$$

ω is the acentric factor of the fluid/gas being studied.

Substituting for the parameters β, δ *and* γ in *Equation B7* and simplifying with *Equations B8 & B9*, the SRK-EOS can be written in terms of gas compressibility as:

$$Z^3 - Z^2 + Z(A - B - B^2) - AB = 0 \qquad\qquad B12$$

B1.2 Peng-Robinson (PR) Equation of State

The PR-EOS is given as:

$$P = \frac{RT}{(v_m - b)} - \frac{a(T)}{(v_m^2 + 2bv_m - b^2)}$$

$$= \frac{RT}{(v_m - b)} - \frac{a(T)}{[(v_m + (1 - \sqrt{2})b)][(v_m + (1 + \sqrt{2})b)]} \qquad B13$$

Compared to *Equation B1*, it can be seen that $\beta = -b$; $\delta = (1 - \sqrt{2})b$ and $\gamma = (1 + \sqrt{2})b$. The PR-EOS is also characterized by $\Omega_a = 0.457535$; $\Omega_b = 0.077796$ *and* m is given as:

$$m = 0.37464 + 1.54226\omega - 0.26992\omega^2 \qquad B14$$

Substituting for the parameters β, δ *and* γ in *Equation B7* and simplifying with *Equations B8 & B9*, the PR-EOS can be written in terms of gas compressibility as:

$$Z^3 + (B - 1)Z^2 + Z(A - 2B - 3B^2) + (B^3 + B^2 - AB) = 0 \qquad B15$$

B1.3 SRK-Peneloux Equation of State

The SRK-Peneloux EOS is given as:

$$P = \frac{RT}{(v_m - b)} - \frac{a(T)}{(v_m + c)(v_m + b + 2c)} \qquad B16$$

Compared to *Equation B1*, it can be seen that $\beta = -b$; $\delta = c$ and $\gamma = b + 2c$. Parameter c is the volume shift factor introduced by Peneloux et al, to modify the SRK-EOS and given as:

$$c = 0.40768 \frac{RT_c}{P_c}(0.29441 - Z_{RA}) \qquad A17$$

Where Z_{RA} is known as the Rackett compressibility factor (Pedersen and Christensen, 2007) given as:

$$Z_{RA} = 0.29056 - 0.08775\omega \qquad A18$$

Introducing a parameter C defined as:

$$C = \frac{cP}{RT} \qquad A19$$

Substituting for the parameters β, δ and γ in *Equation B7* and simplifying with the definitions of A, B & C, the SRK-Peneloux EOS can be written in terms of gas compressibility as:

$$Z^3 + (3C - 1)Z^2 + [A - B - B^2 - 2BC - 3C + 2C^2]Z$$
$$- (AB + BC + B^2C + 2BC^2 + 2C^2) = 0 \qquad B20$$

B1.4 PR-Peneloux Equation of State
The PR-Peneloux EOS is given as:

$$P$$
$$= \frac{RT}{(v_m - b)} - \frac{a(T)}{\{v_m + [b(1 - \sqrt{2}) + c(2 - \sqrt{2})]\}\{v_m + [b(1 + \sqrt{2}) + c(2 + \sqrt{2})]\}} \qquad B21$$

Comparing *Equation B21* to *Equation B1*, it can be seen that $\beta = -b$; $\delta = b(1 - \sqrt{2}) + c(2 - \sqrt{2})$ and $\gamma = b(1 + \sqrt{2}) + c(2 + \sqrt{2})$. The volume shift factor, c is defined in *Equation B17* above. With these and the definition of C given in *Equation B19*, the PR-Peneloux EOS can be written in terms of Z-factor as:

$$Z^3 + (B + 4C - 1)Z^2 + [A - 2B - 3B^2 - 4BC - 2C + 2C^2]Z$$
$$- (AB - B^2 - B^3 + 2BC^2 + 2C^2) = 0 \qquad B22$$

B2. Non-Cubic Equations of State
Two virial-type equations of state have been selected for comparison with the cubic equations presented in *section B1*.

B2.1 LK-EOS
Lee and Kesler (1975) presented a modification of Benedict-Webb-Rubin (BWR) EOS following the principle of corresponding states (Jia et al., 2016, Lee and Kesler, 1975). In terms of the reduced parameters (P_r, T_r & v_r), the LK-EOS is given as:

$$1 + \frac{B}{v_r} + \frac{C}{v_r^2} + \frac{D}{v_r^5} + \frac{c_4}{T_r v_r^2}\left(\beta + \frac{\gamma}{v_r^2}\right)\exp\left(-\frac{\gamma}{v_r^2}\right) - \frac{P_r v_r}{T_r} = 0 \qquad B23$$

The values of the variables B, C & D are given by the following auxiliary equations:

$$B = b_1 - \frac{b_2}{T_r} - \frac{b_3}{T_r^2} - \frac{b_4}{T_r^3}; \quad C = c_1 - \frac{c_2}{T_r} + \frac{c_3}{T_r^3}; \quad D = d_1 + \frac{d_2}{T_r}$$

The compressibility, Z of any fluid of known acentric factor (ω) is given in terms of the compressibility Z^0 of a simple fluid ($\omega = 0$) and the compressibility Z^{ref} of a reference fluid ($\omega = \omega^{ref}$) as follows:

$$Z = Z^0 + \frac{\omega}{\omega^r} (Z^{ref} - Z^0)$$ B24

Where:

$$Z^0 = \frac{P_r v_r^0}{T_r}$$ B25a

$$Z^{ref} = \frac{P_r v_r^{ref}}{T_r}$$ B25b

v_r^0 & v_r^{ref} are respective the reduced specific molar volumes of the simple fluid (rare gas) and reference fluid (n-octane) determined by solving the *Equation B23* for v_r using the corresponding values of the coefficients b₁, b₂, b₃, b₄, c₁, c₂, c₃, c₄, d₁, d₂, β and γ from *Table B1* below.

Table B1: Numerical Values of the coefficients of the LK-EOS (Lee and Kesler, 1975)

Coefficient	Simple fluid	Reference fluid
b_1	0.1181193	0.2026579
b_2	0.265728	0.331511
b_3	0.15479	0.027655
b_4	0.030323	0.203488
c_1	0.0236744	0.0313385
c_2	0.0186984	0.0503618
c_3	0	0.016901
c_4	0.042724	0.041577
d_1	1.55488×10^{-5}	4.87360×10^{-5}
d_2	6.23689×10^{-5}	74.0336×10^{-5}
β	0.65392	1.226
γ	0.060167	0.03754

B2.2 *SBWR-EOS*

Soave (1999)'s modification represented an attempt to reduce the number of terms while improving the accuracy of the BWR-EOS. The SBWR-EOS is given in terms of the three parameters $(P_r, T_r$ & $v_r)$ as:

$$1 + \frac{B}{v_r} + \frac{D}{v_r^4} + \frac{E}{v_r^2}\left(1 + \frac{F}{v_r^2}\right)\exp\left(-\frac{F}{v_r^2}\right) - \frac{P_r v_r}{T_r} = 0$$ B26

The variables B, D, E and F are defined as given in the following auxiliary equations:

$$B = \frac{RT_c}{P_c}\left[bZ_c + 0.422\left(1 - \frac{1}{T_r^{1.6}}\right) + 0.234\omega\left(1 - \frac{1}{T_r^3}\right)\right]$$ B27a

$$D = d\left(\frac{RT_cZ_c}{P_c}\right)^4\left[1 + d_1\left(\frac{1}{T_r} - 1\right) + d_2\left(\frac{1}{T_r} - 1\right)^2\right] \qquad B27b$$

$$E = \left(\frac{RT_c}{P_c}\right)^2\left[eZ_c^2 + e_1\left(\frac{1}{T_r} - 1\right) + e_2\left(\frac{1}{T_r} - 1\right)^2 + e_3\left(\frac{1}{T_r} - 1\right)^3\right] \qquad B27c$$

$$F = f\left(\frac{RT_cZ_c}{P_c}\right)^2 \qquad B27d$$

P_c, T_c and Z_c are respectively the critical pressure, critical temperature and critical Z-factor of a given fluid whose acentric factor is ω. The critical z-factor can be calculated from the Rackett equation (Soave, 1999) given as:

$$Z_c = 0.2908 - 0.099\omega + 0.04\omega^2 \qquad B28a$$

The coefficients in *equations 2.27a-d* can be obtained as follows:

$$b = Z_c - 1 - d - e(1 + f)\exp(-f) \qquad B28b$$

$$d = \frac{1 - 2Z_c - e(1 + f - 2f^2)\exp(-f)}{3} \qquad B28c$$

$$e = \frac{2 - 5Z_c}{(1 + f + 3f^2 - 2f^3)\exp(-f)} \qquad B28d$$

$$f = 0.77 \qquad B28e$$

$$d_1 = 0.4912 + 0.6478\omega \qquad B28f$$

$$d_2 = 0.3000 + 0.3619\omega \qquad B28g$$

$$e_1 = 0.0841 + 0.1318\omega + 0.0018\omega^2 \qquad B28h$$

$$e_2 = 0.0750 + 0.2408\omega - 0.0140\omega^2 \qquad B28i$$

$$e_3 = -0.0065 + 0.1798\omega - 0.0078\omega^2 \qquad B28j$$

The compressibility of any fluid of known acentric factor can then be calculated from *Equation B29* below once the reduced specific molar volume is obtained from *Equation B26* above.

$$Z = \frac{P_r v_r}{T_r} \qquad B29$$

Appendix C

Description of the Adsorption Steps

C1.   Adsorption Steps

Consider two consecutive adsorption steps $i-1$ & i as illustrated in *Figure C1* below. Each adsorption step involves 3 processes discussed as follows:
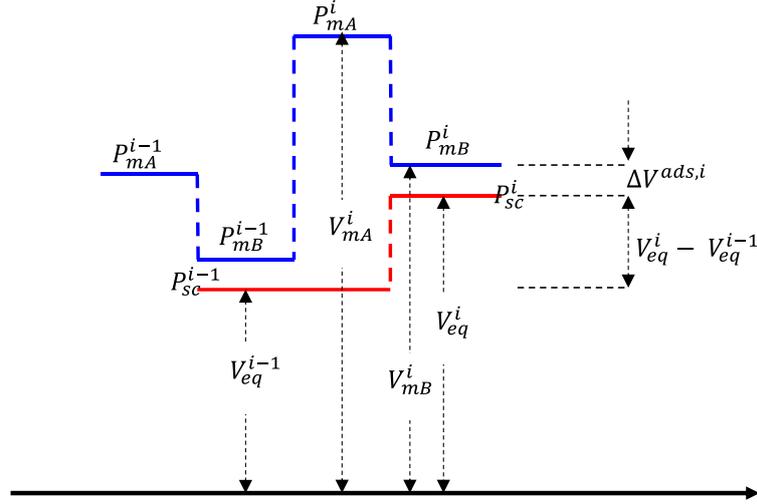
Figure C1: Schematic of two consecutive adsorption pressure steps

a. *Filling the manifold with the adsorbate*: The amount of gas that enters into the manifold at pressure, P_{mA}^i and temperature, T_{mA}^i (where i = 1, 2, 3,..., n) is given as:

$$N_{mA}^i = \frac{P_{mA}^i}{T_{mA}^i Z_{mA}^i} \times \frac{V_{man}}{R} \qquad\qquad C1$$

The equivalent volume at STP is given as:

$$V_{mA}^i \approx \frac{P_{mA}^i V_{man}}{T_{mA}^i Z_{mA}^i} \times \frac{V_{STP}}{R} \qquad\qquad C2$$

Where V_{man} is the volume of the manifold, R = gas constant, Z is the gas compressibility factor and V_{STP} is the molar gas volume at STP ($\approx 22400\ cc$).

b. *Expanding gas from the manifold to the sample cell*: The final pressure and temperature in the manifold are P_{mB}^i and T_{mB}^i respectively. Hence, the amount of gas

expanded/dosed into the sample cell and the equivalent volume at STP can be calculated as:

$$N_{dosed}^{ads,i} = \Delta \left(\frac{P}{ZT}\right)_{man}^{i} \times \frac{V_{man}}{R} \qquad C3$$

$$V_{dosed}^{i} \approx \left(\frac{P_{mA}^{i} V_{man}}{T_{mA}^{i} Z_{mA}^{i}} - \frac{P_{mB}^{i} V_{man}}{T_{mB}^{i} Z_{mB}^{i}}\right) \times \frac{V_{STP}}{R} \qquad C4$$

c. *Equilibrating the gas in the system*: The volume, at STP, of gas in equilibrium is given as:

$$V_{free}^{i} = \left(V_{eq}^{i} - V_{eq}^{i-1}\right) \qquad C5$$

The free space available to gas is composed of three parts, the lower stem of volume, V_{ls}, the upper stem of volume, $V_{us} = 7\text{cc}$ (Zou et al., 2017) and the sample cell of volume, V_{sc}. Therefore:

$$V_{free}^{i} = \frac{V_{STP}}{R}\left[\left(\frac{P_{sc}^{i} V_{sc}}{T_{sc}^{i} Z_{sc}^{i}} + \frac{P_{sc}^{i} V_{us}}{T_{us}^{i} Z_{us}^{i}} + \frac{P_{sc}^{i} V_{ls}}{T_{ls}^{i} Z_{ls}^{i}}\right) - \left(\frac{P_{sc}^{i-1} V_{sc}}{T_{sc}^{i-1} Z_{sc}^{i-1}} + \frac{P_{sc}^{i-1} V_{us}}{T_{us}^{i-1} Z_{us}^{i-1}} + \frac{P_{sc}^{i-1} V_{ls}}{T_{ls}^{i-1} Z_{ls}^{i-1}}\right)\right] \qquad C6$$

Writing a volume balance for the system,

$$V_{dosed}^{i} = V_{free}^{i} + \Delta V^{i} \qquad C7$$

Putting *Equations C4 and C6 in C7*, the differential adsorbed volume per unit mass of the adsorbent can be obtained as follows:

$$\Delta\tilde{V}^{i} = \frac{V_{STP}}{RM_s}\left[\left(\frac{P_{mA}^{i} V_{man}}{T_{mA}^{i} Z_{mA}^{i}} - \frac{P_{mB}^{i} V_{man}}{T_{mB}^{i} Z_{mB}^{i}}\right) - \left(\frac{P_{sc}^{i} V_{sc}}{T_{sc}^{i} Z_{sc}^{i}} + \frac{P_{sc}^{i} V_{us}}{T_{us}^{i} Z_{us}^{i}} + \frac{P_{sc}^{i} V_{ls}}{T_{ls}^{i} Z_{ls}^{i}}\right) + \left(\frac{P_{sc}^{i-1} V_{sc}}{T_{sc}^{i-1} Z_{sc}^{i-1}} + \frac{P_{sc}^{i-1} V_{us}}{T_{us}^{i-1} Z_{us}^{i-1}} + \frac{P_{sc}^{i-1} V_{ls}}{T_{ls}^{i-1} Z_{ls}^{i-1}}\right)\right] \qquad C8$$

The cumulative volume adsorbed per unit mass at any pressure step is given as:

$$\tilde{V}_{r}^{ads} = \sum_{i=1}^{r}\left(\Delta\tilde{V}^{i}\right) \qquad C9$$

For the first adsorption step, it can be safely assumed that $P_{sc}^0 = 0$ since the system is expected to be in fully evacuated prior to this step.

### C2. Ambient Free space Volume Calculation
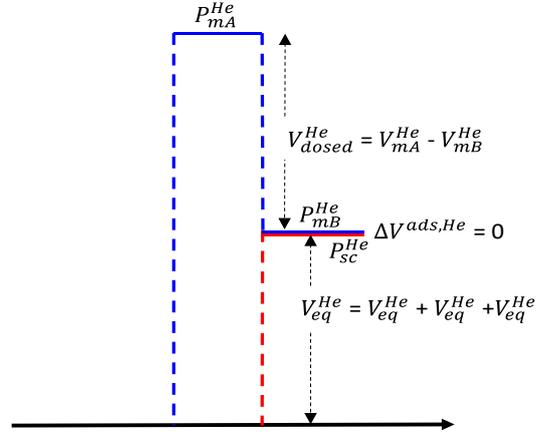
Figure C2: Schematic of helium expansion step measurement of free-space volume

As shown in *Figure C2*, free space measurement follows the adsorption processes described in *section C1* above except that helium gas is used in this case. It is arguably assumed that helium adsorption is negligible ($\Delta V^{ads, He} \approx 0$) (Zhang et al., 2015b, Zou et al., 2017). Therefore:

$$V_{dosed}^{He} = V_{eq}^{He} \qquad\qquad C10$$

$$\frac{P_{mA}^{He} V_{man}}{T_{mA}^{He} Z_{mA}^{He}} - \frac{P_{mB}^{He} V_{man}}{T_{mB}^{He} Z_{mB}^{He}} = \frac{P_{sc}^{He} V_{sc}}{T_{sc}^{He} Z_{sc}^{He}} + \frac{P_{sc}^{He} V_{us}}{T_{us}^{He} Z_{us}^{He}} + \frac{P_{sc}^{He} V_{ls}}{T_{ls}^{He} Z_{ls}^{He}} \qquad\qquad C11$$

The HPVA-II 200® uses two temperature-point steps to determine the volume of free-space and the corresponding values V_{ls}, the volume of the lower stem of the sample holder and V_{sc}, the volume of the sample cell. Note that the volume of the upper stem $V_{ls} \approx 7cc$ (Zou et al., 2017). For the first step, it is assumed that $T_{sc}^{He} = T_{ls}^{He} = Ambient\ temperature$. In this case *Equation 3.4* can be written as (Zhang et al., 2015b):

$$V_{Amfs} = V_{sc} + V_{ls} + V_{us} = V_{lsc} + V_{us} \qquad\qquad C12a$$

Which means:

$$V_{lsc} = V_{sc} + V_{ls} = V_{Amfs} - V_{us} \qquad\qquad C12b$$

Equation C11 can now be written as:

$$V_{Amfs} = \frac{T_{sc}^{He} Z_{sc}^{He}}{P_{sc}^{He}} \left(\frac{P_{mA}^{He} V_{man}}{T_{mA}^{He} Z_{mA}^{He}} - \frac{P_{mB}^{He} V_{man}}{T_{mB}^{He} Z_{mB}^{He}} - \frac{P_{sc}^{He} V_{us}}{T_{us}^{He} Z_{us}^{He}} + \frac{P_{sc}^{He} V_{us}}{T_{sc}^{He} Z_{sc}^{He}} \right) \qquad C13$$

The second step proceeds at the experimental temperature such that $T_{sc}^{He} \neq T_{ls}^{He}$. In this case, *Equations C11 & C12a* are solved for the values of V_{sc} and V_{ls} using the value of V_{Amfs} determined from the previous step (Zhang et al., 2015b).

Appendix D

Attributions

Ekundayo, J. M[1]. and Rezaee, R[1]. (2019) **"Effect of Equation of States on High-Pressure Volumetric Measurements of Methane-Coal Sorption Isotherms-Part 1: Volumes of Free Space and Methane Adsorption Isotherms."** *Energy and Fuels 33 (2): 1029-1036*

[1] WASM: Minerals, Energy and Chemical Engineering, Curtin University, 6151 Kensington, Western Australia

Name	Conceptualization	Methodology and Investigation	Data Curation & Analysis	Interpretation and Discussion	Original Draft Writing	Review, Editing and Approval
Ekundayo, J. M.	X	X	X	X	X	X
I acknowledge that these represent my contributions to the above research output. _____ Ekundayo, J.M.						
Rezaee, R.	X					X
I acknowledge that these represent my contributions to the above research output. _____ Reza Rezaee						

Ekundayo, J. M[1]. and Rezaee, R[1]. (2019) **"Volumetric measurements of methane-coal adsorption and desorption isotherms—Effects of equations of state and implication for initial gas reserves."** *Energies 12 (10)*

[1] WASM: Minerals, Energy and Chemical Engineering, Curtin University, 6151 Kensington, Western Australia

Name	Conceptualization	Methodology and Investigation	Data Curation & Analysis	Interpretation and Discussion	Original Draft Writing	Review, Editing and Approval
Ekundayo, J. M.	X	X	X	X	X	X
I acknowledge that these represent my contributions to the above research output. _____ Ekundayo, J.M.						
Rezaee, R.	X					X
I acknowledge that these represent my contributions to the above research output. _____ Reza Rezaee						

Ekundayo, J. M[1]. and Rezaee, R[1]. (2019) **"Numerical Simulation of Gas Production from Gas Shale Reservoirs – Influence of Gas Sorption Hysteresis."** *Energies 12 (18)*

[1] WASM: Minerals, Energy and Chemical Engineering, Curtin University, 6151 Kensington, Western Australia

Name	Conceptualization	Methodology and Investigation	Data Curation & Analysis	Interpretation and Discussion	Original Draft Writing	Review, Editing and Approval
Ekundayo, J. M.	X	X	X	X	X	X
I acknowledge that these represent my contributions to the above research output. _____ Ekundayo, J.M.						
Rezaee, R.	X					X
I acknowledge that these represent my contributions to the above research output. _____ Reza Rezaee						

Ekundayo, J. M[1]. and Rezaee, R[1]. (2019) **"Numerical Simulation of Gas Production from Gas Shale Reservoirs – Influence of Gas Sorption Hysteresis."** *Energies 12 (18)*

Ekundayo, J. M.[1,2], Rezaee, R.[1] and Fan, C.[1] 2020. "**Experimental investigation and mathematical modelling of shale gas adsorption and desorption hysteresis**". Journal of Natural Gas Science and Engineering, 103761.

[1] WASM: Minerals, Energy and Chemical Engineering, Curtin University, 6151 Kensington, Western Australia

[2] State Key Laboratory of Oil and Gas Reservoir Geology and Exploitation, Southwest Petroleum University, Chengdu, Sichuan, 610500, China

Name	Conceptualization	Methodology and Investigation	Data Curation & Analysis	Interpretation and Discussion	Original Draft Writing	Review, Editing and Approval
Ekundayo, J. M.	X	X	X	X	X	X
I acknowledge that these represent my contributions to the above research output. _____ Ekundayo, J.M.						
Rezaee, R.	X					X
I acknowledge that these represent my contributions to the above research output. _____ Reza Rezaee						
Fan, C.						X
I acknowledge that these represent my contributions to the above research output. _____ Chunyan Fan						

Appendix E

Permission to re-use

Ekundayo, J. M[1]. and Rezaee, R[1]. (2019) **"Effect of Equation of States on High-Pressure Volumetric Measurements of Methane-Coal Sorption Isotherms-Part 1: Volumes of Free Space and Methane Adsorption Isotherms."** *Energy and Fuels 33 (2): 1029-1036*

[1] WASM: Minerals, Energy and Chemical Engineering, Curtin University, 6151 Kensington, Western Australia

Ekundayo, J. M.[1,2], Rezaee, R.[1] and Fan, C.[1] 2020. "**Experimental investigation and mathematical modelling of shale gas adsorption and desorption hysteresis**". Journal of Natural Gas Science and Engineering, 103761.

[1] WASM: Minerals, Energy and Chemical Engineering, Curtin University, 6151 Kensington, Western Australia

[2] State Key Laboratory of Oil and Gas Reservoir Geology and Exploitation, Southwest Petroleum University, Chengdu, Sichuan, 610500, China

References

Al-Fatlawi, O., Hossain, M. M. & Osborne, J. 2017. Determination of best possible correlation for gas compressibility factor to accurately predict the initial gas reserves ingas-hydrocarbon reservoirs. *International Journal of Hydrogen Energy,* 42**,** 25492 - 25508. https://doi.org/https://doi.org/10.1016/j.ijhydene.2017.08.030

Alshakhs, M. 2017. *Shale Play Assessment of the Goldwyer Formation in the Canning Basin Using Property Modelling.* MPhil, Curtin University.

Amrhar, O., Nassali, H. & Elyoubi, M. S. 2015. Two and three-parameter isothermal modeling for adsorption of Crystal Violet dye onto Natural Illitic Clay: Nonlinear regression analysis. *Journal of Chemical and Pharmaceutical Research,* 7**,** 892-903.

Anovitz, L. M. & Cole, D. R. 2015. Characterization and Analysis of Porosity and Pore Structures. *Reviews in Mineralogy & Geochemistry,* 80**,** 61 - 164.

Bae, J.-S., Bhatia, S. K., Rudolph, V. & Massarotto, P. 2009. Pore Accessibility of Methane and Carbon Dioxide in Coals. *Energy & Fuels,* 23**,** 3319-3327. https://doi.org/https://doi.org/10.1021/ef900084b

Bahadur, J., Melnichenko, Y. B., Mastalerz, M., Furmann, A. & Clarkson, C. R. 2014. Hierarchical Pore Morphology of Cretaceous Shale: A Small-Angle Neutron Scattering and Ultrasmall-Angle Neutron Scattering Study. *Energy & Fuels,* 28**,** 6336-6344. https://doi.org/https://doi.org/10.1021/ef501832k

Bahar, M. & Triche, N. E. 2013. Shale Gas Volumetrics of Unconventional Resource Plays in the Canning Basin, Western Australia. *SPE Unconventional Resources Conference and Exhibition-Asia Pacific.* Brisbane, Australia: Society of Petroleum Engineers. https://doi.org/ https://doi.org/10.2118/167078-MS

Battistutta, E., van Hemert, P., Lutynski, M., Bruining, H. & Wolf, K.-H. 2010. Swelling and sorption experiments on methane, nitrogen and carbon dioxide on dry Selar Cornish coal. *International Journal of Coal Geology,* 84**,** 39-48. https://doi.org/https://doi.org/10.1016/j.coal.2010.08.002

Bell, G. J. & Rakop, K. C. 1986. Hysteresis of Methane/Coal Sorption Isotherms. *61st SPE-ATCE.* New Orleans, LA: SPE. https://doi.org/https://doi.org/10.2118/15454-MS

Bernard, S., Wirth, R., Schreiber, A., Schulz, H.-M. & Horsfield, B. 2012. Formation of nanoporous pyrobitumen residues during maturation of the Barnett Shale (Fort Worth Basin). *International Journal of Coal Geology,* 103**,** 3-11. https://doi.org/https://doi.org/10.1016/j.coal.2012.04.010

Bhowmik, S. & Dutta, P. 2019. A study on the effect of gas shale composition and pore structure on methane sorption. *Journal of Natural Gas Science and Engineering,* 62**,** 144-156. https://doi.org/https://doi.org/10.1016/j.jngse.2018.12.009

BP 2020. Statistical Review of World Energy. 69 ed. online.

Brandani, S., Mangano, E. & Sarkisov, L. 2016. Net, excess and absolute adsorption and adsorption of helium. *Adsorption,* 2016**,** 261-276. https://doi.org/https://doi.org/10.1007/s10450-016-9766-0

Brunauer, S., Emmett, P. H. & Teller, E. 1938. Adsorption of Gases in Multimolecular Layers. *J. of Am. Chem. Soc.,* 60**,** 309 - 319. https://doi.org/https://doi.org/10.1021/ja01269a023

Buckingham, A. D., Disch, R. L. & Dunmur, D. A. 1968. Quadrupole moments of some simple molecules. *Journal of the American Chemical Society,* 90**,** 3104-3107. https://doi.org/https://doi.org/10.1021/ja01014a023

Busch, A., Gensterblum, Y. & Krooss, B. M. 2003. Methane and CO2 sorption and desorption measurements on dry Argonne premium coals: pure components and mixtures. *International Journal of Coal Geology,* 55**,** 205-224. https://doi.org/https://doi.org/10.1016/S0166-5162(03)00113-7

Busch, A., Gensterblum, Y., Krooss, B. M. & Siemons, N. 2005. Investigation of high-pressure selective adsorption/desorption behaviour of CO2 and CH4 on coals: An experimental study. *International Journal of Coal Geology,* 66**,** 53– 68. https://doi.org/https://doi.org/10.1016/j.coal.2005.07.003

Bustin, R. M. 2005. Gas shale tapped for big play: AAPG Explorer. February.

Cadman, S. J., Pain, L., Vuckovic, V. & le Poidevin, S. R. 1993. Canning Basin. *In:* SCIENCES, W. A. B. O. R. (ed.) *Australian Petroleum Accumulations.* Western Australia: W.A. Bureau of Resource Sciences.

Cao, T., Song, Z., Wang, S., Cao, X., Li, Y. & Xia, J. 2015. Characterizing the pore structure in the Silurian and Permian shales of the Sichuan Basin, China. *Marine and Petroleum Geology,* 61**,** 140-150. https://doi.org/https://doi.org/10.1016/j.marpetgeo.2014.12.007

Cao, Z., Liu, G., Zhan, H., Li, C., You, Y., Yang, C. & Jiang, H. 2016. Pore structure characterization of Chang-7 tight sandstone using MICP combined with N(2)GA techniques and its geological control factors. *Scientific reports,* 6**,** 36919-36919. https://doi.org/https://doi.org/10.1038/srep36919

Chalmers, G. R. & Bustin, R. M. 2007. On the effects of petrographic composition on coalbed methane sorption. *International Journal of Coal Geology,* 69**,** 288-304.

Chen, L., Jiang, Z., Jiang, S., Liu, K., Yang, W., Tan, J. & Gao, F. 2019a. Nanopore Structure and Fractal Characteristics of Lacustrine Shale: Implications for Shale Gas Storage and Production Potential. *Nanomaterials,* 9**,** 390. https://doi.org/https://doi.org/10.3390/nano9030390

Chen, L., Jiang, Z., Liu, K., Tan, J., Gao, F. & Wang, P. 2017. Pore structure characterization for organic-rich Lower Silurian shale in the Upper Yangtze Platform, South China: A possible mechanism for pore development. *Journal of Natural Gas Science and Engineering,* 46**,** 1-15. https://doi.org/https://doi.org/10.1016/j.jngse.2017.07.009

Chen, L., Jiang, Z., Liu, Q., Jiang, S., Liu, K., Tan, J. & Gao, F. 2019b. Mechanism of shale gas occurrence: Insights from comparative study on pore structures of marine and

lacustrine shales. *Marine and Petroleum Geology,* 104**,** 200-216. https://doi.org/https://doi.org/10.1016/j.marpetgeo.2019.03.027

Chen, L. E. I., Jiang, Z., Liu, K., Yang, W. E. I., Jiang, S. H. U. & Tan, J. 2018. Investigation of fractal characteristics and methane adsorption capacity of the upper triassic lacustrine shale in the Sichuan Basin, Southwest China. *Fractals,* 27**,** 1940011. https://doi.org/https://doi.org/10.1142/S0218348X19400115

Clarkson, C. R., Solano, N., Bustin, R. M., Bustin, A. M. M., Chalmers, G. R. L., He, L., Melnichenko, Y. B., Radliński, A. P. & Blach, T. P. 2013. Pore structure characterization of North American shale gas reservoirs using USANS/SANS, gas adsorption, and mercury intrusion. *Fuel,* 103**,** 606-616. https://doi.org/https://doi.org/10.1016/j.fuel.2012.06.119

Clarkson, C. R., Wood, J., Burgis, S. & Freeman, M. 2012. Nanopore-structure analysis and permeability predictions for a tight gas siltstone reservoir by use of low-pressure adsorption and mercury-intrusion techniques. *SPE Reservoir Evaluation & Engineering,* 16**,** 648-661.

CMG 2016. GEM (Compositional & Unconventional Reservoir Simulator) USER GUIDE *In:* LTD., C. M. G. (ed.).

Coasne, B., Galarneau, A., Di Renzo, F. & Pellenq, R. J. M. 2010. Molecular Simulation of Nitrogen Adsorption in Nanoporous Silica. *Langmuir,* 26**,** 10872-10881. https://doi.org/https://doi.org/10.1021/la100757b

Cook, P., Beck, V., Brereton, D., Clark, R., Fisher, B., Kentish, S., Toomey, J. & Williams, J. 2013. Engineering Energy: Unconventional Gas Production. *A study of shale gas in Australia.* Melbourne, Victoria: Australian Council of Learned Academies (ACOLA).

Cui, X., Bustin, R. M. & Chikatamarla, L. 2007. Adsorption-induced coal swelling and stress: Implications for methane production and acid gas sequestration into coal seams. *Journal of Geophysical Research: Solid Earth,* 112. https://doi.org/https://doi.org/10.1029/2004JB003482

Curtis, J. B. 2002. Fractured shale-gas systems. *AAPG Bulletin,* 86**,** 1921 - 1938. https://doi.org/https://doi.org/10.1306/61EEDDBE-173E-11D7-8645000102C1865D

Dantas, S., Struckhoff, K. C., Thommes, M. & Neimark, A. V. 2019. Phase Behavior and Capillary Condensation Hysteresis of Carbon Dioxide in Mesopores. *Langmuir,* 35**,** 11291-11298. https://doi.org/https://doi.org/10.1021/acs.langmuir.9b01748

Delle Piane, C., Almqvist, B. S. G., MacRae, C. M., Torpy, A., Mory, A. J. & Dewhurst, D. N. 2015. Texture and diagenesis of Ordovician shale from the Canning Basin, Western Australia: Implications for elastic anisotropy and geomechanical properties. *Marine and Petroleum Geology,* 59**,** 56-71. https://doi.org/https://doi.org/10.1016/j.marpetgeo.2014.07.017

Didier, Y. D., Yu-Shu, W., Nicholas, F., Cong, W. & Bernard, B. 2014. Numerical Simulation of Low Permeability Unconventional Gas Reservoirs. *SPE/EAGE European Unconventional Conference and Exhibition.* Vienna, Austria.

Do, D. D. & Do, H. D. 2003. Pore characterization of carbonaceous materials by DFT and GCMC simulations: a review. *Adsorpt Sci Technol* 21**,** 389–423.

Do, D. D. & Do, H. D. 2005. Adsorption of argon from sub- to supercritical conditions on graphitized thermal carbon black and in graphitic slit pores: A grand canonical Monte Carlo simulation study. *The Journal of Chemical Physics,* 123**,** 084701. https://doi.org/https://doi.org/10.1063/1.1996573

Do, D. D. & Do, H. D. 2007. Appropriate volumes for adsorption isotherm studies: The absolute void volume, accessible pore volume and enclosing particle volume. *Journal of Colloid and Interface Science,* 316**,** 317-330. https://doi.org/https://doi.org/10.1016/j.jcis.2007.08.020

Dutta, P., Bhowmik, S. & Das, S. 2011. Methane and carbon dioxide sorption on a set of coals from India. *International Journal of Coal Geology,* 85**,** 289-299. https://doi.org/https://doi.org/10.1016/j.coal.2010.12.004

EIA 2016. International Energy Outlook 2016. Online: U.S. Energy Information Administration.

Ekundayo, M. J. & Rezaee, R. 2019a. Effect of Equation of States on High Pressure Volumetric Measurements of Methane-Coal Sorption Isotherms - Part 1: Volumes of Free Space and Methane Adsorption Isotherms. *Energy & Fuels.* https://doi.org/https://doi.org/10.1021/acs.energyfuels.8b04016

Ekundayo, M. J. & Rezaee, R. 2019b. Numerical Simulation of Gas Production from Gas Shale Reservoirs-Influence of Gas Sorption Hysteresis. *Energies,* 12**,** 1-12. https://doi.org/https://doi.org/10.3390/en12183405

Ekundayo, M. J. & Rezaee, R. 2019c. Volumetric Measurements of Methane-Coal Adsorption and Desorption Isotherms—Effects of Equations of State and Implication for Initial Gas Reserves. *Energies,* 12. https://doi.org/https://doi.org/10.3390/en12102022

Ekundayo, M. J., Rezaee, R. & Fan, C. 2020. Effects of Gas Sorption Hysteresis on Gas Production from Organic-Rich Gas Shale Reservoirs. *SPE Asia Pacific Oil & Gas Conference and Exhibition (SPE APOGCE) 2020.* Virtual (accepted manuscript): Society of Petroleum Engineers. https://doi.org/https://doi.org/10.2118/202462-MS

Espitalie, J., Madec, M., Tissot, B., Mennig, J. J. & Leplat, P. 1977. Source Rock Characterization Method for Petroleum Exploration. *Offshore Technology Conference.* Houston, Texas. https://doi.org/10.4043/2935-MS

Feast, G., Wu, K., Walton, J., Cheng, Z. F. & Chen, B. 2015. Modeling and Simulation of Natural Gas Production from Unconventional Shale Reservoirs. *International Journal of Clean Coal and Energy,* 4**,** 23-32. https://doi.org/http://dx.doi.org/10.4236/ijcce.2015.42003

Feng, Y.-Y., Yang, W. & Chu, W. 2016. Coalbed methane adsorption and desorption characteristics related to coal particle size. *Chinese Physics B,* 25**,** 068102. https://doi.org/https://doi.org/10.1088/1674-1056/25/6/068102

Ferguson, D. P. 2016. *The depositional history of the Ordovician lower Goldwyer Formation, Canning Basin, Western Australia.* M.Sc. Geology.

Fertl, W. H. & Chilingar, G. V. 1988. Total Organic Carbon Content Determined From Well Logs. *SPE Formation Evaluation,* 3**,** 407-419. https://doi.org/https://doi.org/10.2118/15612-PA

Garrido, J., Linares-Solano, A., Mardn-Mardnez, J. M., M. Molina-Sabio, Rodriguez-Reinoso, F. & Torregrosa, R. 1987. Use of N2 vs. C02 in the Characterization of Activated Carbons. *Langmuir,* 3**,** 76 - 81.

Gasparik, M., Bertier, P., Gensterblum, Y., Ghanizadeh, A., Krooss, B. M. & Littke, R. 2014a. Geological controls on the methane storage capacity in organic-rich shales. *International Journal of Coal Geology,* 123**,** 34-51. https://doi.org/https://doi.org/10.1016/j.coal.2013.06.010

Gasparik, M., Ghanizadeh, A., Bertier, P., Gensterblum, Y., Bouw, S. & Krooss, B. M. 2012. High-Pressure Methane Sorption Isotherms of Black Shales from the Netherlands. *Energy & Fuels,* 26**,** 4995-5004. https://doi.org/https://doi.org/10.1021/ef300405g

Gasparik, M., Rexer, T. F. T., Aplin, A. C., Billemont, P., Weireld, G. D., Gensterblum, Y., Henry, M., Krooss, B. M., Liu, S., Ma, X., Sakurovs, R., Song, Z., Staib, G., Thomas, K. M. & Zhang, T. 2014b. First international inter-laboratory comparison of high-pressure CH4, CO2 and C2H6 sorption isotherms on carbonaceous shales. *International Journal of Coal Geology,* 132**,** 131-146. https://doi.org/https://doi.org/10.1016/j.coal.2014.07.010

Gensterblum, Y., van Hemert, P., Billemont, P., Battistutta, E., Busch, A., Krooss, B. M., De Weireld, G. & Wolf, K. H. A. A. 2010. European inter-laboratory comparison of high pressure CO2 sorption isotherms II: Natural coals. *International Journal of Coal Geology,* 84**,** 115-124. https://doi.org/https://doi.org/10.1016/j.coal.2010.08.013

Ghori, K. A. R. 2018. Petroleum source rocks of Western Australia. *The APPEA Journal,* 58**,** 282-310. https://doi.org/https://doi.org/10.1071/AJ17051

Ghori, R. A. K. 2013. Emerging unconventional shale plays in Western Australia. *The APPEA Journal,* 53**,** 313-336.

Goodman, A. L., Busch, A., Duffy, G. J., Fitzgerald, J. E., Gasem, K. A. M., Gensterblum, Y., Krooss, B. M., Levy, J., Ozdemir, E., Pan, Z., Robinson, R. L., Schroeder, K., Sudibandriyo, M. & White, C. M. 2004. An Inter-laboratory Comparison of CO2 Isotherms Measured on Argonne Premium Coal Samples. *Energy & Fuels,* 18**,** 1175-1182. https://doi.org/https://doi.org/10.1021/ef034104h

Gregg, S. J., Sing, K. S. W. & Salzberg, H. 1967. Adsorption surface area and porosity. *Journal of The electrochemical society,* 114**,** 279C.

Guo, S., Lü, X., Song, X. & Liu, Y. 2017. Methane adsorption characteristics and influence factors of Mesozoic shales in the Kuqa Depression, Tarim Basin, China. *Journal of Petroleum Science and Engineering,* 157**,** 187-195. https://doi.org/https://doi.org/10.1016/j.petrol.2017.07.020

Guo, X., Qin, Z., Yang, R., Dong, T., He, S., Hao, F., Yi, J., Shu, Z., Bao, H. & Liu, K. 2019. Comparison of pore systems of clay-rich and silica-rich gas shales in the lower Silurian Longmaxi formation from the Jiaoshiba area in the eastern Sichuan Basin, China. *Marine and Petroleum Geology,* 101**,** 265-280. https://doi.org/https://doi.org/10.1016/j.marpetgeo.2018.11.038

Hadian, P. & Rezaee, R. 2020. The Effect of Supercritical CO2 on Shaly Caprocks. 2020. *Energies.,* 13**,** 149. https://doi.org/https://doi.org/10.3390/en13010149

Hansen, P. C. & O'Leary, D. P. 1993. The use of the L-curve in the regularization of discrete ill-posed problems. *SIAM Journal of Scientific Computing,* 14**,** 1487-1503.

Harpalani, S., Prusty, B. K. & Dutta, P. 2006. Methane/CO2 Sorption Modeling for Coalbed Methane Production and CO2 Sequestration. *Energy & Fuels,* 20**,** 1591-1599. https://doi.org/10.1021/ef050434l

Hashimoto, T., Bailey, A. H. E., Chirinos, A. & Carr, L. K. 2018. Onshore Basin Inventory Volume 2: The Canning, Perth and Officer basins. *In:* AUSTRALIA, G. (ed.). Canberra: Geoscience Australia. https://doi.org/https://doi.org/10.11636/Record.2018.018

He, J., Shi, Y., Ahn, S., Kang, J. W. & Lee, C.-H. 2010. Adsorption and Desorption of CO2 on Korean Coal under Subcritical to Supercritical Conditions. *The Journal of Physical Chemistry B,* 114**,** 4854-4861. https://doi.org/https://doi.org/10.1021/jp911712m

He, L., Mei, H., Hu, X., Dejam, M., Kou, Z. & Zhang, M. 2019. Advanced Flowing Material Balance To Determine Original Gas in Place of Shale Gas Considering Adsorption Hysteresis. *SPE Reservoir Evaluation & Engineering,* 22**,** 1282-1292. https://doi.org/10.2118/195581-PA

Hunt , J. M. 1996. *Petroleum geochemistry and geology,* New York, W. H. Freeman & Company.

Hutson, N. D. & Yang, R. T. 1997. Theoretical basis for the Dubinin-Radushkevitch (D-R) adsorption isotherm equation. *Adsorption,* 3**,** 189-195. https://doi.org/https://doi.org/10.1007/BF01650130

Jessen, K., Tang, G.-Q. & Kovscek, A. R. 2008. Laboratory and Simulation Investigation of Enhanced Coalbed Methane Recovery by Gas Injection. *Transport in Porous Media,* 73**,** 141-159. https://doi.org/https://doi.org/10.1007/s11242-007-9165-9

Jia, W., Li, Z., Liao, K. & Li, C. 2016. Using Lee-Kesler equation of state to compute the compressibility factor of CO2-content natural gas. *Journal of Natural Gas Science and Engineering,* 34**,** 650-656. https://doi.org/http://dx.doi.org/10.1016/j.jngse.2016.07.032

Johnson, L., Rezaee, R., Kadkhodaie, A., Smith, G. & Yu, H. 2017. Integrated Reservoir Characterization of the Goldwyer Formation, Canning Basin. *One Curtin International Postgraduate Conference.* Miri, Sarawak, Malaysia.

Johnson, L., Smith, G., Rezaee, R. & Kadkhodaie, A. 2019. A 3D Model of the Unconventional Play in the Goldwyer Formation: An Integrated Shale Rock Characterisation over the Broome Platform, Canning Basin. *Asia Pacific*

Unconventional Resources Technology Conference. Brisbane, Australia. https://doi.org/https://doi.org/10.15530/AP-URTEC-2019-198312

Johnson, L. M. 2019. *Integrated Reservoir Characterization of the Goldwyer Formation, Canning Basin.* PhD, Curtin University.

Johnson, L. M., Rezaee, R., Smith, G. C., Mahlstedt, N., Edwards, D. S., Kadkhodaie, A. & Yu, H. 2020. Kinetics of hydrocarbon generation from the marine Ordovician Goldwyer Formation, Canning Basin, Western Australia. *International Journal of Coal Geology,* 232**,** 103623. https://doi.org/https://doi.org/10.1016/j.coal.2020.103623

Ju, Y., Jiang, B., Hou, Q., Tan, Y., Wang, G. & Xiao, W. 2009. Behavior and mechanism of the adsorption/desorption of tectonically deformed coals. *Chinese Science Bulletin,* 54**,** 88-94. https://doi.org/https://doi.org/10.1007/s11434-008-0412-4

Jun-yi, L., Zheng-song, Q., Wei-an, H., Yang, L. & Ding-ding, S. 2014. Nano-pore structure characterization of shales using gas adsorption and mercury intrusion techniques. *Journal of Chemical and Pharmaceutical Research,* 6**,** 850-857.

Keller, J. U. & Staudt, R. 2005. *Gas Adsorption Equilibria: Experimental Methods and Adsorptive Isotherms*, Springer.

Kennard, J. M., Jackson, M. J., Romine, K. K., Shaw, R. D. & Southgate, P. N. 1994. Depositional sequences and associated petroleum systems of the Canning Basin, WA. *In:* PURCELL, P. G. & PURCELL, R. R. (eds.) *The Sedimentary Basins of Western Australia.* Perth: Petroleum Exploration Society of Australia Symposium.

Kierlik, E., Monson, P. A., Rosinberg, M. L. & Tarjus, G. 2002. Adsorption hysteresis and capillary condensation in disordered porous solids: a density functional study. *JOURNAL OF PHYSICS: CONDENSED MATTER,* 14**,** 9295–9315. https://doi.org/https://doi.org/10.1088/0953-8984/14/40/319

Kikic, I. 2005. Equations of State (in Chapter 2: Physical and chemical equilibria). *In:* AMADEI, C. (ed.) *Encyclopedia of Hydrocarbons.* Roma: MARCHESI GRAFICHE EDITORIALI S.p.A.

Kim, H. J., Shi, Y., He, J., Lee, H.-H. & Lee, C.-H. 2011. Adsorption characteristics of CO2 and CH4 on dry and wet coal from subcritical to supercritical conditions. *Chemical Engineering Journal,* 171**,** 45-53. https://doi.org/https://doi.org/10.1016/j.cej.2011.03.035

King, G. R. 1993. Material-Balance Techniques for Coal-Seam and Devonian Shale Gas Reservoirs With Limited Water Influx. *SPE Reservoir Engineering,* 8**,** 67-72. https://doi.org/https://doi.org/10.2118/20730-PA

Klaver, J., Desbois, G., Littke, R. & Urai, J. L. 2015. BIB-SEM characterization of pore space morphology and distribution in postmature to overmature samples from the Haynesville and Bossier Shales. *Marine and Petroleum Geology,* 59**,** 451-466. https://doi.org/https://doi.org/10.1016/j.marpetgeo.2014.09.020

Klobes, P., Meyer, K. & Munro, R. G. 2006. NIST Recommended Practice Guide: Porosity and Specific Surface Area Measurements for Solid Materials. *In:* TECHNOLOGY, N. I. O. S. A. (ed.).

Klock, G. O. 1968. *Pore Size Distributions as Measured by the Mercury Intrusion Method and Their Use in Predicting Permeability.* Doctor of Philosophy, Oregon State University.

Kuila, U., McCarty, D. K., Derkowski, A., Fischer, T. B., Topór, T. & Prasad, M. 2014. Nano-scale texture and porosity of organic matter and clay minerals in organic-rich mudrocks. *Fuel,* 135**,** 359-373. https://doi.org/https://doi.org/10.1016/j.fuel.2014.06.036

Labani, M. M. 2014. *An Investigation into the Interrelationship between Petrophysical Properties of Potential Gas Shale Reservoirs from Western Australia.* PhD, Curtin University.

Lafarge, E., Marquis, F. & Pillot, D. 1998. Rock-Eval 6 Applications in Hydrocarbon Exploration, Production, and Soil Contamination Studies. *Revue de l'Institut français du pétrole,* 53**,** 421-437. https://doi.org/https://doi.org/10.2516/ogst:1998036

Langmuir, I. 1918. The adsorption of gases on plane surfaces of glass, mica and platinum. *Journal of the American Chemical Society,* 40**,** 1361-1403. https://doi.org/https://doi.org/10.1021/ja02242a004

Lastoskie, C., Gubbins, K. E. & Quirke, N. 1993. Pore size distribution analysis of microporous carbons: a density functional theory approach. *Journal of Physical Chemistry,* 97**,** 4786–4796. https://doi.org/https://doi.org/10.1021/j100120a035

Lastoskie, C. M., Quirke, N. & Gubbins, K. E. 1997. Chapter 15. Structure of Porous Adsorbents: Analysis Using Density Functional Theory and Molecular Simulation. *Studies in Surface Science and Catalysis,* 104**,** 745-775. https://doi.org/https://doi.org/10.1016/S0167-2991(97)80078-X

Leahy-Dios, A., Das, M., Agarwal, A. & Kaminsky, R. D. 2011. Modeling of Transport Phenomena and Multicomponent Sorption for Shale Gas and Coalbed Methane in an Unstructured Grid Simulator. *SPE ATCE.* Denver, Colorado, USA.

Lee, B. I. & Kesler, M. G. 1975. A Generalized Thermodynamic Correlation Based on Three-Parameter Corresponding States. *AIChE Journal,* 21**,** 510 - 527.

Li, F., Wang, M., Liu, S. & Hao, Y. 2019. Pore characteristics and influencing factors of different types of shales. *Marine and Petroleum Geology,* 102**,** 391-401. https://doi.org/https://doi.org/10.1016/j.marpetgeo.2018.11.034

Li, M., Chen, Z., Cao, T., Ma, X., Liu, X., Li, Z., Jiang, Q. & Wu, S. 2018. Expelled oils and their impacts on Rock-Eval data interpretation, Eocene Qianjiang Formation in Jianghan Basin, China. *International Journal of Coal Geology,* 191**,** 37-48. https://doi.org/https://doi.org/10.1016/j.coal.2018.03.001

Liu, Y. C., Chen, D. X., Qiu, N. S., Wang, Y., Fu, J., Huyan, Y., Jia, J. K. & Wu, H. 2017a. Reservoir characteristics and methane adsorption capacity of the Upper Triassic continental shale in Western Sichuan Depression, China. *Australian Journal of Earth*

Sciences, 64**,** 807-823.
https://doi.org/https://doi.org/10.1080/08120099.2017.1342174

Liu, Z., He, Y., Xu, J., Huang, P. & Jilani, G. 2008. The ratio of clay content to total organic carbon content is a useful parameter to predict adsorption of the herbicide butachlor in soils. *Environmental Pollution (1987),* 152**,** 163-171.
https://doi.org/https://doi.org/10.1016/j.envpol.2007.05.006

Liu, Z., Zhang, Z., Lu, Y., Ki Choi, S. & Liu, X. 2017b. Sorption Hysteresis Characterization of CH4 and CO2 on Anthracite, Bituminous Coal, and Lignite at Low Pressure. *Journal of Energy Resources Technology,* 140**,** 012203-012203-9.
https://doi.org/https://doi.org/10.1115/1.4037483

Loucks, R. G., Reed, R. M., Ruppel, S. C. & Jarvie, D. M. 2009. Morphology, Genesis, and Distribution of Nanometer-Scale Pores in Siliceous Mudstones of the Mississippian Barnett Shale. *Journal of Sedimentary Research,* 79**,** 848-861.
https://doi.org/https://doi.org/10.2110/jsr.2009.092

Lowell, S. & Shields, J. E. 1981. Equivalency of mercury porosimetry and gas adsorption. *Powder Technology,* 29**,** 225-231. https://doi.org/https://doi.org/10.1016/0032-5910(81)87024-6

Lutynski, M. A., Battistutta, E., Bruining, H. & Wolf, K.-H. A. A. 2011. Discrepancies inthe assessment of CO$_2$ storage capacity and methane recovery from coal with selected equation of states Part I. Experimental isotherm calculation. *Physicochemical Problems of Mineral Processing,* 47**,** 159 - 168.

Ma, C., Dong, C., Lin, C., Elsworth, D., Luan, G., Sun, X. & Liu, X. 2019. Influencing factors and fracability of lacustrine shale oil reservoirs. *Marine and Petroleum Geology,* 110**,** 463-471.
https://doi.org/https://doi.org/10.1016/j.marpetgeo.2019.07.002

Ma, X. & Guo, S. 2019. Comparative Study on Shale Characteristics of Different Sedimentary Microfacies of Late Permian Longtan Formation in Southwestern Guizhou, China. *Minerals,* 9. https://doi.org/https://doi.org/10.3390/min9010020

Mastalerz, M., He, L., Melnichenko, Y. B. & Rupp, J. A. 2012. Porosity of Coal and Shale: Insights from Gas Adsorption and SANS/USANS Techniques. *Energy & Fuels,* 26**,** 5109-5120. https://doi.org/https://doi.org/10.1021/ef300735t

McCarty, R. D. & Arp, V. D. 1990. *New wide range equation of state for helium.*

Menon, P. G. 1968. Adsorption at high pressures. *Chemical Reviews,* 68**,** 277-294.
https://doi.org/https://doi.org/10.1021/cr60253a002

Micromeritics 2013. HPVA II - High-Pressure Volumetric Analyzer. *In:* SYSTEMS, P. (ed.) *HPVA-II Brochure.* Norcross GA

Milliken, K. L. & Curtis, M. E. 2016. Imaging pores in sedimentary rocks: Foundation of porosity prediction. *Marine and Petroleum Geology,* 73**,** 590-608.
https://doi.org/https://doi.org/10.1016/j.marpetgeo.2016.03.020

Monson, G. 1983. A model of adsorption-desorption hysteresis in which hysteresis is primarily developed by the interconnections ina network of pores. *Proceedings of the Royal Society of London. Series A, Mathematical and Physical Sciences,* 390**,** 47 - 72. https://doi.org/https://doi.org/10.1098/rspa.1983.0122

Myers, A. L. & Monson, P. A. 2002. Adsorption in Porous Materials at High Pressure: Theory and Experiment. *Langmuir,* 18**,** 10261-10273. https://doi.org/https://doi.org/10.1021/la026399h

Myers, A. L. & Monson, P. A. 2014. Physical adsorption of gases: the case for absolute adsorption as the basis for thermodynamic analysis. *Adsorption,* 20**,** 591-622. https://doi.org/https://doi.org/10.1007/s10450-014-9604-1

Nunez-Betelu, L. & Baceta, J. I. Basics and application of Rock-Eval/TOC pyrolysis: an example from the uppermost Paleocene/lowermost Eocene in the Basque Basin, Western Pyrenees. Munibe Ciencias naturales, 1994. 43-62.

Ozdemir, E. 2004. *Chemistry of the Adsorption of Carbon dioxide by Argonne Premium Coals and a Model to Simulate CO$_2$ Sequestration in Coal Seams.* Doctor of Philosophy, University of Pittsburgh.

Ozdemir, E. 2017. Dynamic nature of supercritical CO2 adsorption on coals. *Adsorption,* 23**,** 25-36. https://doi.org/https://doi.org/10.1007/s10450-016-9814-9

Pan, L., Xiao, X., Tian, H., Zhou, Q. & Cheng, P. 2016. Geological models of gas in place of the Longmaxi shale in Southeast Chongqing, South China. *Marine and Petroleum Geology,* 73**,** 433-444. https://doi.org/https://doi.org/10.1016/j.marpetgeo.2016.03.018

Pan, Z., Connell, L. D., Camilleri, M. & Connelly, L. 2010. Effects of matrix moisture on gas diffusion and flow in coal. *Fuel,* 89**,** 3207-3217. https://doi.org/https://doi.org/10.1016/j.fuel.2010.05.038

Pariti, U. M. 1992. *Coal sorption behavior using gas mixture.* M.Sc., The University of Arizona.

Parra-Garcia, M., Sanchez, G., Dentith, M. & George, A. 2014. Regional structural and stratigraphic study of the Canning Basin, Western Australia. *In:* AUSTRALIA, G. S. O. W. (ed.). Perth: Department of Mines and Petroleum Government of Western Australia.

Pedersen, K. S. & Christensen, P. L. 2007. *Chapter 4: Cubic Equations of State in Phase Behavior of Petroleum Reservoir Fluids,* Boca Raton, CRC Press, Taylor & Francis Group.

Péneloux, A., Rauzy, E. & Fréze, R. 1982. A consistent correction for Redlich-Kwong-Soave volumes. *Fluid Phase Equilibria,* 8**,** 7-23. https://doi.org/https://doi.org/10.1016/0378-3812(82)80002-2

Peters, K. & Cassa, M. 1994. Applied Source Rock Geochemistry. *In:* MAGOON, L. B. & DOW, W. G. (eds.) *AAPG Memoir.* AAPG. https://doi.org/https://doi.org/10.1306/M60585C5

Peters, K. E. Guidelines for Evaulating Petroleum Source Rock Using Programmed Pyrolysis. *In:* GEOLOGISTS, A. A. O. P., ed. American Chemical Society, Symposium on Organic Geochemistry of Humic Substances, Kerogen and Coal, 1986 Philadelphia, Pennsylvania. American Association of Petroleum Geologists, 318-329. https://doi.org/https://doi.org/10.1306/94885688-1704-11D7-8645000102C1865D

Pevear, D. R. Illite and hydrocarbon exploration. National Academy of Sciences colloquium ''*Geology, Mineralogy, and Human Welfare*'', 1999 Irvine, CA.: National Academy of Sciences, 3440–3446. https://doi.org/https://doi.org/10.1073/pnas.96.7.3440

Pillalamarry, M., Harpalani, S. & Liu, S. 2011. Gas diffusion behavior of coal and its impact on production from coalbed methane reservoirs. *International Journal of Coal Geology,* 86**,** 342-348. https://doi.org/https://doi.org/10.1016/j.coal.2011.03.007

Pruess, K. & Narasimhan, T. 1985. A practical method for modeling fluid and heat flow in fractured porous media. *Society of Petroleum Engineers Journal,* 25**,** 14-26.

Rabbani, A. R. & Kamali, M. R. 2005. Source rock evaluation and petroleum geochemistry, offshore SW Iran. *Journal of Petroleum Geology,* 28**,** 413-428. https://doi.org/https://doi.org/10.1111/j.1747-5457.2005.tb00091.x

Rajniak, P. & Yang, R. T. 1993. A Simple Model and Experiments for Adsorption-Desorption Hysteresis: Water Vapor on Silica Gel. *AIChE Journal,* 39**,** 774 – 786.

Rani, S. & Sud, D. 2015. Effect of temperature on adsorption-desorption behaviour of triazophos in Indian soils. *Plant Soil Environ.,* 61**,** 36 - 42. https://doi.org/https://doi.org/10.17221/704/2014-PSE

Ravikovitch, P. I., Vishnyakov, A. & Neimark, A. V. 2001. Density functional theories and molecular simulations of adsorption and phase transitions in nanopores. *PHYSICAL REVIEW E,* 64**,** 1-20. https://doi.org/https://doi.org/10.1103/PhysRevE.64.011602

Rexer, T. F. T., Benham, M. J., Aplin, A. C. & Thomas, K. M. 2013. Methane Adsorption on Shale under Simulated Geological Temperature and Pressure Conditions. *Energy & Fuels,* 27**,** 3099-3109. https://doi.org/https://doi.org/10.1021/ef400381v

Rodrigues, C. F. A., Machado Da Silva, J. M., Dinis, M. A. P. & Lemos De Sousa, M. J. 2018. Effect of gas compressibility factor estimation in coal sorption isotherms accuracy. *International Journal of Oil, Gas and Coal Technology,* 19**,** 230-247. https://doi.org/https://doi.org/10.1504/IJOGCT.2018.094544

Ross, D. J. & Bustin, R. M. 2007. Shale gas potential of the lower Jurassic Gordondale member, northeastern British Columbia, Canada. *Bulletin of Canadian Petroleum Geology,* 55**,** 51-75.

Ross, D. J. & Bustin, R. M. 2008. Characterizing the shale gas resource potential of Devonian–Mississippian strata in the Western Canada sedimentary basin: Application of an integrated formation evaluation. *AAPG bulletin,* 92**,** 87-125.

Ross, D. J. K. & Bustin, R. M. 2009. The importance of shale composition and pore structure upon gas storage potential of shale gas reservoirs. *Marine and Petroleum Geology,* 26**,** 916-927. https://doi.org/https://doi.org/10.1016/j.marpetgeo.2008.06.004

Rouquerol, J., Rouquerol, F., Llewellyn, P. & Denoyel, R. 2016. Surface excess amounts in high-pressure gas adsorption: Issues and benefits. *Colloids and Surfaces A: Physicochemical and Engineering Aspects,* 496**,** 3-12. https://doi.org/https://doi.org/10.1016/j.colsurfa.2015.10.045

Sakurovs, R., Day, S., Weir, S. & Duffy, G. 2007. Application of a Modified Dubinin−Radushkevich Equation to Adsorption of Gases by Coals under Supercritical Conditions. *Energy & Fuels,* 21**,** 992-997. https://doi.org/https://doi.org/10.1021/ef0600614

Seidle, J. 2011a. Gas and Water Mass Balances in Coals. *Fundamentals of Coalbed Methane Reservoir Engineering.* Tulsa, Oklahoma: PennWell.

Seidle, J. 2011b. Sorption of Gas on Coals. *Fundamentals of Coalbed Methane Reservoir Engineering.* Tulsa, Oklahoma: PennWell.

Setzmann, U. & Wagner, W. 1991. A New Equation of State and Tables of Thermodynamic Properties for Methane Covering the Range from the Melting Line to 625 K at Pressures up to 100 MPa. *Journal of Physical and Chemical Reference Data,* 20**,** 1061-1155. https://doi.org/https://doi.org/10.1063/1.555898

Sing, K. S. W. 2001. The use of nitrogen adsorption for the characterisation of porous materials. *Colloids and Surfaces A: physicochemical Engineering Aspects,* 187 - 188**,** 3 - 9. https://doi.org/http://dx.doi.org/10.1351/pac198557040603

Sing, K. S. W., Everett, D. H., Haul, R. A. W., Moscou, L., Pierotti, R. A., Rouquerol, J. & Siemieniewska, T. 1985. REPORTING PHYSISORPTION DATA FOR GAS/SOLID SYSTEMS with Special Reference to the Determination of Surface Area and Porosity (Recommendations 1984). *Pure & Applied Chemistry,* 57**,** 603 - 619. https://doi.org/http://dx.doi.org/10.1351/pac198557040603

Sing, K. S. W. & Williams, R. T. 2004. The Use of Molecular Probes for teh Characterization of nanoporous Adsorbents. *Part. Syst. Charact.,* 21**,** 71-79. https://doi.org/https://doi.org/10.1002/ppsc.200400923

Soave, G. S. 1999. An effective modification of the Benedict-Webb-Rubin equation of state. *Fluid Phase Equilibria,* 164**,** 157-172. https://doi.org/https://doi.org/10.1016/S0378-3812(99)00252-6

Spaak, G., Edwards, D. S., Foster, C. B., Pagès, A., Summons, R. E., Sherwood, N. & Grice, K. 2017. Environmental conditions and microbial community structure during the Great Ordovician Biodiversification Event; a multi-disciplinary study from the Canning Basin, Western Australia. *Global and Planetary Change,* 159**,** 93-112. https://doi.org/https://doi.org/10.1016/j.gloplacha.2017.10.010

Sun, M., Yu, B., Hu, Q., Zhang, Y., Li, B., Yang, R., Melnichenko, Y. B. & Cheng, G. 2017. Pore characteristics of Longmaxi shale gas reservoir in the Northwest of Guizhou, China: Investigations using small-angle neutron scattering (SANS), helium pycnometry, and gas sorption isotherm. *International Journal of Coal Geology,* 171**,** 61-68. https://doi.org/https://doi.org/10.1016/j.coal.2016.12.004

Taghavinejad, A., Sharifi, M., Heidaryan, E., Liu, K. & Ostadhassan, M. 2020. Flow modeling in shale gas reservoirs: A comprehensive review. *Journal of Natural Gas*

Science and Engineering, 83**,** 103535.
https://doi.org/https://doi.org/10.1016/j.jngse.2020.103535

Tang, X., Ripepi, N., Luxbacher, K. & Pitcher, E. 2017. Adsorption Models for Methane in Shales: Review, Comparison, and Application. *Energy & Fuels,* 31**,** 10787-10801. https://doi.org/https://doi.org/10.1021/acs.energyfuels.7b01948

Tang, X., Wang, Z., Ripepi, N., Kang, B. & Yue, G. 2015. Adsorption Affinity of Different Types of Coal: Mean Isosteric Heat of Adsorption. *Energy & Fuels,* 29**,** 3609-3615. https://doi.org/https://doi.org/10.1021/acs.energyfuels.5b00432

Testamanti, M. N. 2018. *Assessment of Fluid Transport Mechanisms in Shale Gas Reservoirs.* PhD, Curtin University.

Thommes, M., Cychosz, K. A. & Neimark, A. V. 2012. Chapter 4 - Advanced Physical Adsorption Characterization of Nanoporous Carbons. *In:* TASCÓN, J. M. D. (ed.) *Novel Carbon Adsorbents.* Oxford: Elsevier. https://doi.org/https://doi.org/10.1016/B978-0-08-097744-7.00004-1

Thommes, M., Kanero, K., Neimark, A. V., Olivier, J. P., Rodriguez-Reinoso, F., Rouquerol, J. & Sing, K. S. W. 2015. Physisorption of gases, with special reference to the evaluation of surface area and pore size distribution (IUPAC technical Report). *Pure & Applied Chemistry,* 87**,** 1051-1069. https://doi.org/https://doi.org/10.1515/pac-2014-1117

Thompson, A. & Goyne, K. W. 2012. Introduction to the Sorption of Chemical Constituents in Soils. *Nature Education Knowledge* 4**,** 7-11.

Ustinov, E. A. & Do, D. D. 2004. Application of density functional theory to capillary phenomena in cylindrical mesopores with radial and longitudinal density distributions. *Journal of Chemical Physics,* 120**,** 9769 - 9781. https://doi.org/https://doi.org/10.1063/1.1710860

Ustinov, E. A. & Do, D. D. 2005. Modeling of Adsorption in Finite Cylindrical Pores by Means of Density Functional Theory. *Adsorption,* 11**,** 455 - 477. https://doi.org/

https://doi.org/10.1007/s10450-005-5606-3

van Hattum, J., Bond, A., Jablonski, D. & Taylor-Walshe, R. 2019. Exploration of an unconventional petroleum resource through extensive core analysis and basin geology interpretation utilising play element methodology: the Lower Goldwyer Formation, onshore Canning Basin, Western Australia. *The APPEA Journal,* 59. https://doi.org/https://doi.org/10.1071/aj18225

Wang, F. & Guo, S. 2019. Shale gas content evolution in the Ordos Basin. *International Journal of Coal Geology,* 211**,** 103231. https://doi.org/https://doi.org/10.1016/j.coal.2019.103231

Wang, G., Ren, T., Wang, K. & Wu, Y. 2014a. Influence of Maximum Pressure on the Path of CO_2 Desorption Isotherm on Coal. *Energy & Fuels,* 28**,** 7093-7096. https://doi.org/https://doi.org/10.1021/ef501974a

Wang, G., Ren, T., Zhang, L. & Shu, L. 2017a. Undesorbable residual gas in coal seams and its influence on gas drainage. *International Journal of Mining Science and Technology,* 27**,** 763-769. https://doi.org/https://doi.org/10.1016/j.ijmst.2017.07.019

Wang, J., Dong, M., Yang, Z., Gong, H. & Li, Y. 2016a. Investigation of Methane Desorption and Its Effect on the Gas Production Process from Shale: Experimental and Mathematical Study. *Energy & Fuels,* 31 205−216. https://doi.org/https://doi.org/10.1021/acs.energyfuels.6b02033

Wang, J., Dong, M., Yang, Z., Gong, H. & Li, Y. 2017b. Investigation of Methane Desorption and Its Effect on the Gas Production Process from Shale: Experimental and Mathematical Study. *Energy & Fuels,* 31**,** 205-216. https://doi.org/https://doi.org/10.1021/acs.energyfuels.6b02033

Wang, J., Luo, H., Liu, H., Cao, F., Li, Z. & Sepehrnoori, K. 2015. An Integrative Model To Simulate Gas Transport and Production Coupled With Gas Adsorption, Non-Darcy Flow, Surface Diffusion, and Stress Dependence in Organic-Shale Reservoirs. *SPE Journal***,** 244-264.

Wang, K., Wang, G., Ren, T. & Cheng, Y. 2014b. Methane and CO2 sorption hysteresis on coal: A critical review. *International Journal of Coal Geology,* 132**,** 60-80. https://doi.org/https://doi.org/10.1016/j.coal.2014.08.004

Wang, R., Sang, S., Zhu, D., Liu, S. & Yu, K. 2017c. Pore characteristics and controlling factors of the Lower Cambrian Hetang Formation shale in Northeast Jiangxi, China. *Energy Exploration & Exploitation,* 36**,** 43-65. https://doi.org/https://doi.org/10.1177/0144598717723814

Wang, W., Yu, W., Hu, X., Liu, H., Chen, Y., Wu, K. & Wu, B. 2018. A semianalytical model for simulating real gas transport in nanopores and complex fractures of shale gas reservoirs. *AIChE Journal,* 64**,** 326-337. https://doi.org/https://doi.org/10.1002/aic.15881

Wang, Y., Zhu, Y., Liu, S. & Zhang, R. 2016b. Methane adsorption measurements and modeling for organic-rich marine shale samples. *Fuel,* 172**,** 301-309. https://doi.org/https://doi.org/10.1016/j.fuel.2015.12.074

Washburn, E. W. 1921. Note on a method of determining the distribution of pore sizes in a porous material. *The Proceedings of the National Academy of Sciences,* 7**,** 115–116.

Wei, G., Hu, Z., Zhang, X., Yu, R. & Wang, L. 2017a. Shale Gas Adsorption and Desorption Characteristics and its Effects on Shale Permeability. *Energy Exploration & Exploitation,* 35(4)**,** 463-481. https://doi.org/https://doi.org/10.1177/0144598716684306

Wei, G., Hu, Z., Zhang, X., Yu, R. & Wang, L. 2017b. Shale Gas Adsorption and Desorption Characteristics and its Effects on Shale Permeability. *Energy Exploration & Exploitation,* 0(0)**,** 1-19. https://doi.org/10.1177/0144598716684306

Wei, G., Xiong, W., Gao, S., Hu, Z., Liu, H. & yu, R. 2013. Impact of temperature on the isothermal adsorption/desorption characteristics of shale gas. *Petroleum Exploration and Development,* 40**,** 514-519 https://doi.org/https://doi.org/10.1177/0144598716684306

Weishauptová, Z., Medek, J. & Kovář, L. 2004. Bond forms of methane in porous system of coal II. *Fuel,* 83**,** 1759-1764. https://doi.org/https://doi.org/10.1016/j.fuel.2004.03.001

Weishauptová, Z., Přibyl, O., Sýkorová, I. & Machovič, V. 2015. Effect of bituminous coal properties on carbon dioxide and methane high pressure sorption. *Fuel,* 139**,** 115-124. https://doi.org/https://doi.org/10.1016/j.fuel.2014.08.030

Wellman, C. H., Steemans, P. & Vecoli, M. 2013. Palaeophytogeography of Ordovician–Silurian land plants. *In:* HARPER, D. A. T. & SERVAIS, T. (eds.) *Early Palaeozoic Biogeography and Palaeogeography.* London: The Geological Society of London. https://doi.org/http://dx.doi.org/10.1144/M38.29

Xiong, J., Liu, X. & Liang, L. 2015. Experimental study on the pore structure characteristics of the Upper Ordovician Wufeng Formation shale in the southwest portion of the Sichuan Basin, China. *Journal of Natural Gas Science and Engineering,* 22**,** 530-539. https://doi.org/https://doi.org/10.1016/j.jngse.2015.01.004

Xiong, Q., Li, K., Yang, D., Yu, H., Pan, Z. & Song, Y. 2020. Characterizing coal pore space by gas adsorption, mercury intrusion, FIB–SEM and μ-CT. *Environmental Earth Sciences,* 79**,** 209. https://doi.org/https://doi.org/10.1007/s12665-020-08950-3

Yan-Yan, F., Wen, Y. & Wei, C. 2016. Coalbed methane adsorption and desorption characteristics related to coal particle size. *Chinese Physics B,* 25.

Yang, F., Hu, B., Xu, S., Meng, Q. & Kroos, B. M. 2018a. Thermodynamic Characteristic of Methane Sorption on Shales from Oil, Gas, and Condensate Windows. *Energy & Fuels.* https://doi.org/https://doi.org/10.1021/acs.energyfuels.8b02140

Yang, R., He, S., Hu, Q., Sun, M., Hu, D. & Yi, J. 2017. Applying SANS technique to characterize nano-scale pore structure of Longmaxi shale, Sichuan Basin (China). *Fuel,* 197**,** 91-99. https://doi.org/https://doi.org/10.1016/j.fuel.2017.02.005

Yang, S., Wu, W., Xu, J., Ji, D., Chen, Z. & Wei, Y. 2018b. Modeling of Methane/Shale Excess Adsorption Under Reservoir Conditions. *SPE Reservoir Evaluation & Engineering,* 21**,** 1027-1034. https://doi.org/10.2118/180076-PA

Yang, Y. & Liu, S. 2020. Review of Shale Gas Sorption and Its Models. *Energy & Fuels.* https://doi.org/https://doi.org/10.1021/acs.energyfuels.0c02906

Yu, W., Huang, S., Wu, K. & Sepehrnoori, K. 2014a. Development of A Semi-Analytical Model for Simulation of Gas Production in Shale Gas Reservoirs. *Unconventional Resources Technology Conference, .* Denver, Colorado: Society of Exploration Geophysicists, American Association of Petroleum Geologists, Society of Petroleum Engineers. https://doi.org/https://doi.org/10.15530/urtec-2014-1922945

Yu, W., Sepehrnoori, K. & Patzek, T. W. 2014b. Evaluation of Gas Adsorption in Marcellus Shale. *SPE ATCE.* Amsterdam, The Netherlands.

Yuan, Y., Rezaee, R., Al-Khdheeawi, E. A., Hu, S.-Y., Verrall, M., Zou, J. & Liu, K. 2019. Impact of Composition on Pore Structure Properties in Shale: Implications for Micro-/Mesopore Volume and Surface Area Prediction. *Energy & Fuels,* 33**,** 9619-9628. https://doi.org/https://doi.org/10.1021/acs.energyfuels.9b02232

Zhang, J., Clennell, M. B., Liu, K., Pervukhina, M., Chen, G. & Dewhurst, D. N. 2016. Methane and Carbon Dioxide Adsorption on Illite. *Energy & Fuels,* 30**,** 10643-10652. https://doi.org/https://doi.org/10.1021/acs.energyfuels.6b01776

Zhang, L., Aziz, N., Ren, T., Nemcik, J. & Tu, S. 2014. Influence of coal particle size on coal adsorption and desorption characteristics. *Archives of Mining Sciences,* 59**,** 807-820. https://doi.org/https://doi.org/10.2478/amsc-2014-0056

Zhang, R. & Liu, S. 2016. Experimental and theoretical characterization of methane and CO2 sorption hysteresis in coals based on Langmiur desorption. *International Journal of Coal Geology,* 171**,** 49-60. https://doi.org/http://dx.doi.org/10.1016/j.coal.2016.12.007

Zhang, R., Liu, S., Bahadur, J., Elsworth, D., Melnichenko, Y., He, L. & Wang, Y. 2015a. Estimation and modeling of coal pore accessibility using small angle neutron scattering. *Fuel,* 161**,** 323-332. https://doi.org/https://doi.org/10.1016/j.fuel.2015.08.067

Zhang, W., Xu, J. & Jiang, R. 2017. Production forecast of fractured shale gas reservoir considering multi-scale gas flow. *Journal of Petroleum Exploration and Production Technology,* 7**,** 1071-1083. https://doi.org/https://doi.org/10.1007/s13202-016-0281-3

Zhang, Y., Xing, W., Liu, S., Liu, Y., Yang, M., Zhao, J. & Song, Y. 2015b. Pure methane, carbon dioxide, and nitrogen adsorption on anthracite from China over a wide range of pressures and temperatures: experiments and modeling. *RSC Advances,* 5**,** 52612-52623. https://doi.org/https://doi.org/10.1039/C5RA05745K

Zhou, F., Hussain, F., Guo, Z., Yanici, S. & Cinar, Y. 2013. Adsorption/Desorption Characteristics for Methane, Nitrogen and Carbon Dioxide of Coal Samples from Southeast Qinshui Basin, China. *Energy Exploration & Exploitation,* 31**,** 645-665. https://doi.org/https://doi.org/10.1260/0144-5987.31.4.645

Zhou, S., Xue, H., Ning, Y., Guo, W. & Zhang, Q. 2018. Experimental study of supercritical methane adsorption in Longmaxi shale: Insights into the density of adsorbed methane. *Fuel,* 211**,** 140-148. https://doi.org/https://doi.org/10.1016/j.fuel.2017.09.065

Zhu, H. & Selim, H. M. 2000. Hysteretic behavior of metolachlor adsorption-desorption in soils. *Soil Science,* 165**,** 632-645. https://doi.org/https://doi.org/10.1097/00010694-200008000-00005

Zou, J. & Rezaee, R. 2016a. Effect of particle size on high-pressure methane adsorption of coal. *Petroleum Research,* 1**,** 53-58. https://doi.org/https://doi.org/10.1016/s2096-2495(17)30030-3

Zou, J. & Rezaee, R. 2016b. Effect of particle size on high-pressure methane adsorption of coal. *Petroleum Research,* 1**,** 53-58.

Zou, J. & Rezaee, R. 2019. A Prediction Model for Methane Adsorption Capacity in Shale Gas Reservoirs. *Energies,* 12**,** 280. https://doi.org/https://doi.org/10.3390/en12020280

Zou, J. & Rezaee, R. 2020. Methane adsorption capacity of shale samples from Western Australia. *Australian Journal of Earth Sciences,* 67**,** 107-113. https://doi.org/https://doi.org/10.1080/08120099.2019.1656104

Zou, J., Rezaee, R. & Liu, K. 2017. Effect of Temperature on Methane Adsorption in Shale Gas Reservoirs. *Energy & Fuels,* 31**,** 12081 - 12092. https://doi.org/https://doi.org/10.1021/acs.energyfuels.7b02639